SEARCH FOR STERILE NEUTRINO OSCILLATIONS WITH THE PROSPECT EXPERIMENT

BY

PRANAVA TEJA SURUKUCHI

Submitted in partial fulfillment of the
requirements for the degree of
Doctor of Philosophy in Department of Physics
in the Graduate College of the
Illinois Institute of Technology

Approved 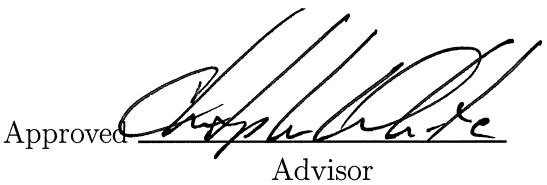
Advisor

Chicago, Illinois
May 2019

ACKNOWLEDGMENT

This thesis has been made possible by the effort of various people. This is my attempt at acknowledging everyone without whom this work wouldn't have been possible. This is perhaps a more formidable task than preparing the dissertation document itself. I apologize in advance if I forgot to mention someone.

I would like to thank Prof. Christopher White for taking me into the group and giving me the opportunity to be a part of the vibrant community of experimental neutrino physics and the support he provided along my PhD journey. I am greatly indebted to Prof. Bryce Littlejohn for being the advisor I could never have even hoped to have. In addition to having the foresight to propel me in the right direction, Bryce always gave me the chance to pursue my ideas while making sure that I do not meander out into an unproductive wilderness. I am also very appreciative of his upbeat and fresh outlook on research. There has not been a single encounter with Bryce where I didn't come out inspired and optimistic about my future in research. I am fortunate to have had him as my advisor. I would also like to thank the rest of my committee for giving me suggestions to improve my thesis. Prof. Zack Sullivan for taking genuine interest and thoroughly going through my dissertation and providing valuable comments; Prof. Kevin Cassel for giving advise on the general outline of my dissertation.

I am very fortunate to have Karin as my mentor. She has not only been extremely patient with me in answering my innumerable questions in a painstaking detail, but also guided me in taking my first steps in research. It is not an overstatement to say that large parts of this research wouldn't have been possible without Karin's patience and encouragement. I am thankful to Xianyi for being the ever-cheerful and accommodative compatriot. It has been a true pleasure to work in close quarters with Xianyi at all stages of graduate school. Ever since I joined the

PROSPECT experiment, Danielle has been a close companion who was always there to lend an ear whenever needed to share the ups and downs of research life. Not only has she been a confidant, but has also been a source of support for me.

I am very thankful for the important work done by Yonas, Keith, Ian, Lexi who worked for countless hours tirelessly and meticulously to fabricate and perform QC/QA of the PROSPECT optical grid components. I also thank Yonas and Lexi for taking significant amount of time off in traveling with me long distances and playing an invaluable role in making PROSPECT possible; Keith and Ian for helping design the cleanroom setup that made the fabrication of separators possible.

I am also thankful to various members of the PROSPECT experiment who have created a valuable research environment and provided support when needed. Tom for his detector expertise and the time and effort he puts in to make complicated things easily discernible; Michael for the immense amount of work he put to create low-level frameworks that made all the rest of the analysis possible; Xiangpan, Chao, Xin for their expertise, hard work, and the valuable advice they provided in performing the sterile neutrino search; Olga for performing several cross-checks that made the oscillation search robust; the hardware team for providing valuable inputs that made the detector design possible; the analysis team which put in an incredible amount of work towards getting to the physics data; the assembly team which have tirelessly worked in putting the detector together into one piece; the spokespersons and the IB for making important decisions in progressing the experiment; in particular, Karsten and Nathaniel who also provided valuable advise to me when needed; and many more people who put in huge amount of time and effort in providing personal guidance and making the experiment possible overall.

I am thankful to Dave, David, and Sharon at Ingeniven who went out of their way to not only produce high quality separators for PROSPECT but also to make

my stay in Hampton enjoyable. I acknowledge Dylan, Evan, and Chris at Autotiv for being very receptive of all the support rod requirements and for willing to change the design at a moment's notice.

I would like to acknowledge the role played by several people at IIT and in Chicago. Prof. Yurii Shylnov for always being a huge support and giving me confidence to continue to PhD program; Prof. Carlo Segre for advising me during my Master's program and giving me hope at a time when I was contemplating to leave physics forever; Sal for providing valuable support and time in early R&D of the PROSPECT optical grid; Todd and Joy for making my journey so much easier; David for providing insights into the professional world of neutrino physics; countless teachers, classmates, and other members of IIT who made my 7 years at IIT worthwhile. Although I was away from my family I barely ever felt homesick, thanks to all the friends I made at IIT. Sashank, Rohit, and Abhiroop have not only been fun roommates but also great friends who made living in Chicago a fun experience.

I cannot thank Katya enough for being there for me whenever I needed and for keeping me sane at times when my world seemed to fall in disarray. She has not only been a moral support for me but has inspired me time and time again to strive to be better everyday.

Finally, but most importantly I am forever indebted to my parents for encouraging me to choose my own path. They selflessly provided sustained support for me even at times when I didn't deserve it. They have been my biggest strength and I dedicate this thesis to them.

యన్మాతాపితరౌ వృత్తం తనయే కురుతః సదా
న సుప్రతీకారం తత్తు మాత్రా పిత్రా చ యత్కృతం

TABLE OF CONTENTS

Page

ACKNOWLEDGEMENT iii

LIST OF TABLES viii

LIST OF FIGURES xii

ABSTRACT xiii

CHAPTER

1. SUMMARY AND OUTLINE 1

1.1. Neutrinos, Reactors, and Sterile Neutrino Oscillations . . . 1
1.2. PROSPECT Experiment 2
1.3. Sterile Neutrino Search with the PROSPECT Experiment . 3
1.4. Future Prospects and Implications of the PROSPECT Experiment 3
1.5. Thesis Outline 4
1.6. Primary Contributions 6

2. INTRODUCTION TO NEUTRINOS, NEUTRINO MIXING AND STERILE NEUTRINOS 8

2.1. Postulation and Discovery of the Neutrino 8
2.2. Experimental Discoveries of the Neutrino Properties 10
2.3. Neutrinos in and Beyond the Standard Model 13

3. REACTOR NEUTRINOS AND NEUTRINO ANOMALIES . . 19

3.1. Reactor Antineutrino Experiments 19
3.2. Reactor Antineutrino Spectrum 23
3.3. Anomalies in the Reactor Neutrino Sector 29
3.4. Anomalies Hinting at Sterile Neutrinos in Other Sectors . . 33

4. PROSPECT EXPERIMENT 35

4.1. HFIR as the Source of $\overline{\nu}_e$ 35
4.2. PROSPECT Detector 39
4.3. Detector Assembly 54
4.4. Detector Installation 55
4.5. PROSPECT Prototype Detectors 55

5. PROSPECT OPTICAL GRID 57

5.1. Design of the Optical Segmentation System 57

5.2. Fabrication and QC/QA of the Optical Separators 68
5.3. Fabrication and QC/QA of the Support Rods 75
5.4. Preparation and Assembly of the PROSPECT Optical Grid 76

6. CALIBRATION, RECONSTRUCTION, EVENT CLASSIFICATION AND PERFORMANCE OF THE PROSPECT DETECTOR 80

6.1. PROSPECT Data Analysis Framework 80
6.2. Detector Calibration 84
6.3. Event Classification 90
6.4. Performance of the Detector 96
6.5. Validation of PROSPECT Monte Carlo Simulations 97
6.6. Neutrinos in the PROSPECT Detector 100

7. OSCILLATION SEARCH WITH THE PROSPECT EXPERIMENT 105

7.1. Sterile Neutrino Search Strategy 105
7.2. Modeling the Experiment 108
7.3. Data and Inputs 118
7.4. Uncertainty Handling 121
7.5. Confidence Interval Assignment 132
7.6. Fitter Validation and Performance 135
7.7. Results 140
7.8. Cross-checks 142
7.9. Impact of Systematical Uncertainties 144

8. CONCLUSION 146

APPENDIX 149

A. STATISTICAL TECHNIQUES 149
A.1. Equivalence of the Pulls based χ^2 and the Covariance Matrix Based χ^2 150
A.2. Mapping Covariance Matrix from Segments to Baselines . . 152
A.3. Statistical Covariance Matrices 153
A.4. Covariance Matrices and Toy Datasets 155

B. RATIONALE BEHIND USING FELDMAN COUSINS APPROACH 157

BIBLIOGRAPHY 161

LIST OF TABLES

Table		Page
2.1	Neutrino Oscillation Parameters	14
3.1	Fission Energies of the Dominant Fission Isotopes	26
3.2	An Example Analytical Approximation for the $\overline{\nu}_e$ Energy Spectrum	28
4.1	PROSPECT parameters	36
4.2	PROSPECT Prototypes	56
5.1	Nominal Separator Dimensions	64
5.2	Support Rod Types	68
6.1	Radioactive Calibration Sources	87
6.2	Event Classification	92
6.3	Event Rates	102
7.1	Systematic Uncertainties	124
7.2	Systematic Contribution to Uncertainty	145

LIST OF FIGURES

Figure		Page
2.1	Savannah River Experiment	9
3.1	KamLAND Results	22
3.2	$\overline{\nu}_e$ Production in Nuclear Reactors	24
3.3	$\overline{\nu}_e$ Spectra from the Major Isotopes	27
3.4	Reactor Antineutrino Spectrum at a Detector	29
3.5	Reactor Antineutrino Anomaly	31
3.6	Sterile Neutrino Oscillation Parameter Space	32
4.1	HFIR Reactor Core	37
4.2	Evolution of the Fission Fractions of Major Fission Isotopes.	37
4.3	Detector Schematic	39
4.4	IBD Schematic	41
4.5	Optical Grid Schematic	43
4.6	PMT Positioning in the PROSPECT Detector	44
4.7	PMT Module Schematic	45
4.8	PROSPECT Shielding Schematic	47
4.9	PROSPECT Calibration Schematics	48
4.10	PROSPECT Calibration Locations	49
4.11	DAQ Schematic	52
5.1	Optical Grid Schematic	59
5.2	Optical Separator Schematic	61
5.3	DF2000MA Reflectivity in Air	62
5.4	DF2000MA Reflectivity in LiLS	63
5.5	Optical Separator	64
5.6	Support Rod Types and Locations	67

5.7 Optical Separator Fabrication Schematic 69
5.8 Lamination Process 70
5.9 Optical Separator Trimmer 71
5.10 Separator Dimensions 72
5.11 Sealing Scheme 73
5.12 Heat Sealing QA 74
5.13 Printed Support Rods 75
5.14 Assembly of the Optical Grid 77
5.15 Separator Support Rod Pre-assembly 77
6.1 Analysis Data Structures and Relations 83
6.2 Corner-clipping Muon Events 84
6.3 Muon Based Position Calibration 86
6.4 Longitudinal Dependence of the Waveform Integrals 87
6.5 Light Curves 88
6.6 Pulse Shape Discrimination 89
6.7 Post-calibration PSD 89
6.8 Actinium Decay Scheme 95
6.9 Detector Segment-to-segment Uniformity 96
6.10 Detector Stability 97
6.11 Data-MC Comparison 99
6.12 Pressure Dependence on Cosmogenic Event Rates 101
6.13 IBD Candidates 103
6.14 Baseline Dependent IBD Rates 103
7.1 Sterile Neutrino Oscillation Search Procedure 106
7.2 HFIR Power Map 108
7.3 Baseline Mapping 110
7.4 Modeled $\overline{\nu}_e$ Rates 111

7.5 Non-Equilibrium Isotopes Contribution 112
7.6 ^{28}Al Contribution 112
7.7 Detector Response Matrices 115
7.8 Map of Ignored Segments 116
7.9 Reconstructed MC $\overline{\nu}_e$ Spectrum 116
7.10 Reconstructed MC L vs E Spectra 117
7.11 Reconstructed MC Oscillated L vs E Spectrum 118
7.12 Prompt Segment and Baseline Spectra 119
7.13 Comparison of the Measured to the Predicted Spectra 120
7.14 Signal Systematic Covariance Matrix 128
7.15 Total Signal Covariance Matrix 129
7.16 Background Systematic Covariance Matrix 130
7.17 Total Background Covariance Matrix 131
7.18 χ^2 Distributions 133
7.19 Full Parameter Space $\Delta\chi^2_C$ Distributions 134
7.20 PROSPECT Sensitivity 134
7.21 Fitter Validation Employing Oscillated Simulated Spectra 135
7.22 Fitter Validation Employing Oscillated Simulated Toys with Fluctuations 136
7.23 Toy MC Best-fit $\sin^2 2\theta$ and Δm^2_{14} Distributions 137
7.24 Toy MC Best-fit $\sin^2 2\theta$ Distributions 138
7.25 Toy MC Best-fit Δm^2_{14} Distributions 139
7.26 Toy χ^2 Distribution 141
7.27 Exclusion Curve 141
7.28 Exclusion Curve Using Two Separate Statistical Methods 143
7.29 Impact of Models on the Exclusion Curves 143
8.1 Global Reactor Sterile Neutrino Searches 147

B.1 Standard χ^2 Improper Coverage 159
B.2 Confidence Interval Assignment Comparison 160

ABSTRACT

Neutrinos have been one of the most interesting particles to study for the best part of the last century. Ever since the first discovery of neutrinos, various experiments using both natural and artificial neutrino sources have helped in determining the nature of neutrinos. In particular, experiments in the last two decades helped determine the neutrino oscillation parameters. Although three neutrino picture is well established, discrepancies have been observed in some recent reactor, accelerator, and source neutrino experiments hinting at the existence of a fourth weakly non-interacting neutrino called a *sterile* neutrino. Additional experimental investigation is needed to test the sterile neutrino hypothesis and identify the source of discrepancies.

PROSPECT is a short-baseline reactor antineutrino experiment designed to search for sterile neutrinos and make a precise measurement of ^{235}U reactor antineutrino spectrum from the High Flux Isotope Reactor at Oak Ridge National Laboratory located in Tennessee. The PROSPECT detector is segmented with ^{6}Li-loaded liquid scintillator as the target. The design and development of the PROSPECT detector started in 2014 and the assembly and installation have finished by early 2018. PROSPECT detector has been collecting data since March 2018. The design, development, and installation of the detector is discussed with a particular emphasis on the components designed and developed at Illinois Institute of Technology. The detector calibration, event reconstruction, and data quality are also discussed. Finally, the sterile neutrino search using 33 days of reactor on data and 29 days of reactor off data is presented.

CHAPTER 1

SUMMARY AND OUTLINE

1.1 Neutrinos, Reactors, and Sterile Neutrino Oscillations

Neutrinos are the most abundant fundamental particles in the universe after photons. They play a key role in the formation and evolution of the Universe. Although there has been a lot of progress in understanding these elusive particles since their discovery, questions about the nature of neutrinos still persist and are being actively investigated.

Neutrinos are weakly interacting very low mass spin-1/2 particles. Three distinct species (flavors) of neutrinos are experimentally verified to exist. Each flavor of neutrino is composed of an assorted admixture of three distinct masses. Neutrinos are produced (and detected) as one of the three well-defined flavors (flavor-eigenstates) but they travel as one of the masses (mass-eigenstates). A consequence of this *mixing* is that there is a non-zero probability of a neutrino generated in one flavor being detected in one of the other two flavors. If the neutrinos had identical masses, this probability would have been zero. Experimental discovery of neutrino oscillations have led to a conclusion that at least two of the three neutrinos have non-zero mass.

The neutrino was discovered at Savannah River Plant (SRP) nuclear reactor in 1956 with inverse beta decay reaction as the detection mechanism. Ever since, reactors have played a major role in the study of neutrinos including the measurement of multiple mixing angles and early cross-section investigations. In the three neutrino paradigm, the last identified and the most precisely measured mixing angle was simultaneously by three reactors experiments–Daya Bay, Double Chooz, and RENO.

Recently, new evidence manifested for the potential existence of a fourth neutrino flavor in reactor, accelerator, and radioactive source neutrino experiments. This neutrino, if exists does not undergo standard nuclear interactions and hence is referred to as a sterile neutrino. Existence of sterile neutrinos would have major implications in the current understanding of the standard model of particle physics.

1.2 PROSPECT Experiment

The PROSPECT experiment was primarily conceived to search for eV-scale sterile neutrinos and measure the antineutrino ($\overline{\nu}_e$) spectrum from the fissions of ^{235}U. The source of $\overline{\nu}_e$ for the PROSPECT experiment is an 85 MW highly enriched uranium reactor called the High Flux Isotope Reactor (HFIR) at the Oak Ridge National Laboratory in Tennessee. The $\overline{\nu}_e$ emanating from the HFIR are primarily from ^{235}U , one of the isotopes of Uranium. This enables a precise measurement of the ^{235}U spectrum. The small size of the HFIR core, and accessibility to space in close proximity to the reactor enables a search for sterile neutrinos via high frequency oscillation of $\overline{\nu}_e$.

The PROSPECT detector is a $\sim$4 ton single volume Lithium (^{6}Li) loaded liquid scintillator detector optically divided into 154 identical segments. $\overline{\nu}_e$ generated via beta decay in the reactor are detected via delayed coincidence of inverse beta decay ($\overline{\nu}_e + p \rightarrow e^+ + n$) products; positrons followed by neutrons. High resolution measurement is made possible by the use of a novel segmentation approach that uses very thin highly reflective surfaces. Scintillation light generated by electromagnetic recoils from the positron (prompt signal) and nuclear recoils from neutron capture on ^{6}Li (delayed signal) is transported by the reflective surfaces and is collected by two photomultiplier tubes—one at each end of a segment. Using a combination of time profile information and temporal and spatial coincidences of the prompt and the delayed signals, PROSPECT was able to achieve good signal efficiency while

eliminating more than five orders of magnitude of backgrounds.

1.3 Sterile Neutrino Search with the PROSPECT Experiment

The design of the PROSPECT experiment enables a search for sterile neutrinos with minimal reliance on the reactor $\overline{\nu}_e$ spectrum models. High frequency neutrino oscillations produce a coherent variation in energy dependent antineutrino flux within the detector. With segmentation providing a baseline-dependent inverse beta decay spectrum, the oscillation signature was investigated by comparing the spectrum at multiple baselines within the detector.

This sterile neutrino search dataset includes two discrete periods that amount to 33 days of reactor on data. 28 contiguous days of reactor off data was also used for cosmogenic background subtraction. With a time-averaged rate of $\sim$750 signal events/day and a signal-to-background ratio of $\sim$ 1, $\sim$ 25k signal events were accumulated during this period. PROSPECT observed no evidence of eV-scale sterile neutrino oscillations and disfavored the oscillation parameters suggested by the reactor anomalies at 2.2 σ.

1.4 Future Prospects and Implications of the PROSPECT Experiment

PROSPECT is in a unique location to cover high amplitude oscillations not accessible to other reactor neutrino experiments. The initial oscillation search was performed with only $\sim$3 calendar months of PROSPECT data. In addition to collection of more data, significant improvements in the systematic uncertainties are possible with more calibration campaigns underway. Combined improvements in the statistical and systematic uncertainties will enable the PROSPECT detector to provide improved coverage. A combination of PROSPECT with other reactor neutrino oscillation experiments covering low oscillation frequencies will effectively cover most of the suggested sterile neutrino parameter space.

PROSPECT measures the $\overline{\nu}_e$ spectrum solely from the ^{235}U fission isotope. This measurement, in addition to providing a ^{235}U benchmark spectrum, will also help identify issues with the existing ^{235}U models. PROSPECT's pure ^{235}U spectrum measurement combined with the spectrum measurement from a power reactor[1] will also help identify issues in reactor models of the other primary fission isotopes. Finally, PROSPECT's demonstration of the ability to perform on-surface reactor $\overline{\nu}_e$ measurement has paved the way for neutrinos as a potential probe for reactor monitoring.

1.5 Thesis Outline

This thesis presents the first search for high frequency oscillations mediated by sterile neutrinos using PROSPECT experiment. The outline of the thesis is as follows:

Chapter 1 contains the summary of the thesis with a brief introduction to neutrinos, sterile neutrinos, reactors, and the PROSPECT experiment.

Chapter 2 provides an overview of experimental and theoretical neutrino physics. The postulation of neutrinos and the experiments that led to their discovery is discussed. A historical perspective of the experiments that aided in discovery of neutrino properties is given. Finally, the theory pertaining to neutrino oscillations is described.

Chapter 3 discusses the neutrino experiments that utilize reactors as their source and delineates some of the methods used in these experiments. Various approaches used in the prediction of neutrino spectrum from the reactors are described and contrasted. Anomalies in the reactor neutrino sector are discussed with a focus on the those that could arise from the presence of sterile neutrinos. Anomalies in the other sectors that similarly could be solved by the existence of the sterile neutrinos are

[1] ^{235}U, ^{239}Pu, ^{238}U, and ^{241}Pu are the primary fission isotopes in a typical power reactor.

commented on briefly.

Chapter 4 gives a description of the PROSPECT experiment. The source of neutrinos for the PROSPECT experiment is discussed with the accompanying details about its merits and drawbacks. A comprehensive description of the design of the PROSPECT detector and its components is provided. A brief discussion on the assembly and the installation of the detector is given. Finally, the chapter ends with a quick introduction of the prototypes that led to the final design of the PROSPECT detector.

Chapter 5 gives a complete description of the design of the PROSPECT optical grid system. The design of optical separators and support rods is provided. The production and QC/QA of the optical grid components and their incorporation into the PROSPECT detector is given.

Chapter 6 describes the low level analyses and the validation of the data collected with the PROSPECT detector. The framework developed by the collaboration to perform data analysis is described. Calibration and reconstruction of the physics quantities are discussed. The classification of events based on the reconstructed physics quantities is described. The validation and performance of the data collected with the PROSPECT detector is discussed. Finally, the neutrino dataset collected with 33 days of data is illustrated.

Chapter 7 provides the search for oscillations using 33 days of PROSPECT data. The fitter developed to search for oscillations with minimal dependence on the reactor antineutrino models is described. A detailed description of the detector and reactor simulations along with the inputs that went into the oscillation search is provided. Following the description of the statistical technique used in assigning confidence intervals, the robustness of the fitter is demonstrated. Results of a high frequency oscillation search performed with the data collected with the PROSPECT detector is reported. The robustness of the fitter is demonstrated for different statistical tech-

niques and different input models. Finally, the impact of systematic uncertainties on the results are discussed.

Chapter 8 provides concluding statements of the thesis.

Appendix A describes some of the statistical techniques that are employed in the oscillation fitter.

Appendix B shows the pitfall of using the standard approach in defining confidence intervals with PROSPECT as a use case.

1.6 Primary Contributions

In addition to several minor contributions, these are my primary contributions to the PROSPECT experiment.

- **Hardware:** I have co-led the design, development, fabrication, and QA/QC of the PROSPECT optical separators and support rods. I have led the selection of the separator material and the selection and development of the process for the lamination. In conjunction with Ingeniven, I have developed a custom heat sealing technique and associated QA protocols to encapsulate the separators in 2 mil FEP film. I have worked with Autotiv in fine tuning the design of the separator rods. In conjunction with the rest of the assembly team, I have developed the cleaning and QC/QA processes for pre-assembly and assembly of the separators and the support rods. I have also been part of the inner detector assembly team and helped in performing segment QA of the assembled detector. The details of the hardware work I did for the PROSPECT detector are included in Chapter. 5. The work done in the development of the optical separators and support rods have led to a technical paper [1] currently under review with the Journal of Instrumentation.

- **Analysis:** I have led the development of the framework to search for reactor

model-independent search for sterile neutrinos with the PROSPECT experiment. I have performed PROSPECT sterile neutrino sensitivity studies in helping optimize the detector design. Finally, I have performed the first search for sterile neutrino search with the PROSPECT data. This included developing detector response matrix, leading the uncertainty analysis and covariance matrix development the details of which are included in the Chapter. 7. The analysis I did for the PROSPECT experiment led to a refereed article [2] in Physical Review Letters.

CHAPTER 2

INTRODUCTION TO NEUTRINOS, NEUTRINO MIXING AND STERILE NEUTRINOS

2.1 Postulation and Discovery of the Neutrino

The history of neutrinos can be traced back to the early experiments on radioactivity. Several measurements involving beta decay radiation including those conducted by James Chadwick [3] showed that the measured beta spectrum was continuous. This was opposed to the gamma and alpha emission spectra both of which were demonstrated to have well-defined discrete values. The continuous beta spectrum was later confirmed by Ellis and Wooster [4] using a calorimetric technique. Experiments conducted by Meitner [5] later also showed that no gamma radiation was emitted from beta decays disproving the hypothesis that beta decay electrons might be radiating energy while traveling. Further, the nuclear spins of the ^{14}N and ^{6}Li atoms—in contradiction to Rutherford's prediction [6] of 1/2— turned out to be 1 which seemingly violates spin-statistics theorem.

In order to explain the observed discrepancies in the radioactive experiments, Pauli in 1931 postulated [7] the existence of a spin-half neutral particle contained in the nucleus, which he called a *neutron*. He suggested that a fraction of energy produced in the beta decay was carried away undetected in the form of the kinetic energy of this very light particle. Since this particle was hypothesized to have a spin of one-half, the spin-statistics problem could also be explained by the presence of this particle.

The theory of beta decay [8] proposed by Fermi in 1934 laid out the theoretical foundation of this neutral particle. Since an uncharged particle with the name neutron

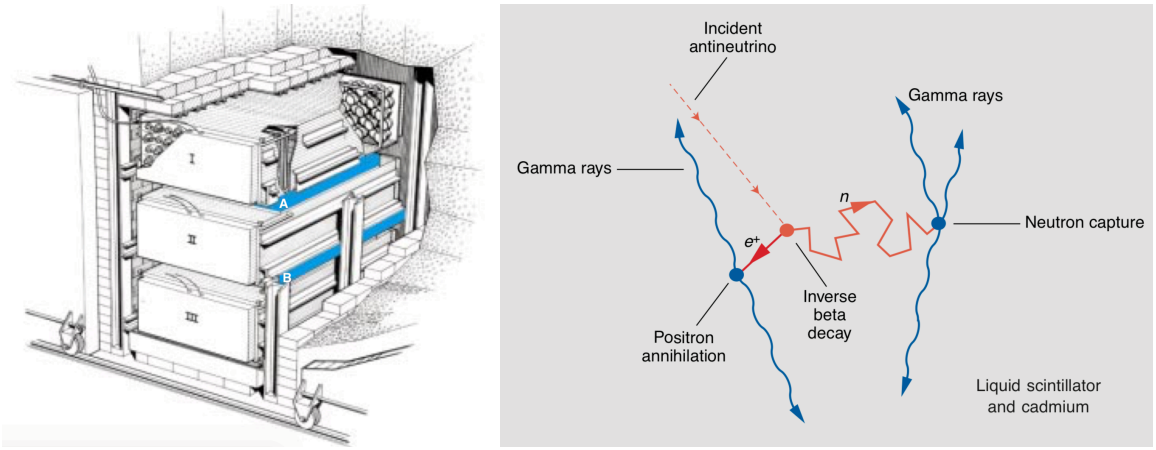

Figure 2.1. The detector schematic (left) and the detection mechanism (right) used in the Savannah River experiment [9]. The detector consisted of two Cadmium Chloride filled water tanks (A and B shown in blue) which acted as the proton targets for the inverse beta decay reactions and three tanks of liquid scintillators (I,II, and III) where the IBD signals deposit their energies to be detected by the photomultiplier tubes.

already existed, Fermi renamed this light uncharged particle a *neutrino*. Fermi's theory allows for the neutrino mass to be zero and additionally predicts a process opposite to the beta decay called inverse beta decay (IBD).

It was not until 1956 that the neutrino was experimentally discovered by Reines, Cowan *et al.* at the Savannah River reactor [10]. The reactor provided intense antineutrino flux of $5 \times 10^{13}\text{cm}^{-2}\text{s}^{-1}$ at the detector. The detector consisted of two tanks of water dissolved with Cadmium Chloride sandwiched between three tanks of liquid scintillator. Both liquid scintillator tanks were viewed on either ends by 110 photomultiplier tubes (PMT). Antineutrinos from the Savannah River reactor were captured on protons in water by the IBD interaction

$$\overline{\nu}_e + p \rightarrow e^+ + n. \tag{2.1}$$

The positron from the IBD reaction in addition to depositing its kinetic energy also annihilates with electrons promptly and generates two gammas via

$$e^+ + e^- \rightarrow \gamma + \gamma. \tag{2.2}$$

These gammas travel into a separate tank and through scintillation process release photons to be collected by the photomultiplier tubes. The IBD neutron thermalizes after scattering on protons and captures on Cadmium:

$$n + {}^{108}\mathrm{Cd} \rightarrow \gamma + {}^{109}\mathrm{Cd}. \tag{2.3}$$

A delayed time-coincidence was used between the positron and the neutron as a signature to tag an IBD event. The reactor was shut down and reactor on versus reactor off rates were compared to demonstrate that the rates were higher when the reactor was on. This conclusively proved the existence of neutrinos. Most of the reactor antineutrino experiments to date detect neutrinos via a delayed coincidence of the IBD interaction. The schematic of the Savannah Reactor reactor experiment and the detection mechanism used for the experiment are shown in the Fig. 2.1.

2.2 Experimental Discoveries of the Neutrino Properties

Incidentally, the answer to the question of whether neutrino is its own antiparticle was deduced by an experiment done by Ray Davis [11] in 1955, even prior to the discovery of the neutrino. Pontecorvo suggested a practical method to look for a neutrino using the capture of a neutrino on ^{37}Cl. With Brookhaven National Lab (BNL) Graphite Research Reactor as the source and Carbon Tetrachloride as the target, a search for neutrinos was attempted using the reaction

$$\overline{\nu}_e + \mathrm{Cl}^{37} \rightarrow e^- + \mathrm{Ar}^{37}. \tag{2.4}$$

Conservation of lepton number states that this reaction is not possible. If the conversion of ^{37}Cl to ^{37}Ar was noticed, it would have meant that the lepton number is not conserved and neutrino was its own antiparticle. Since no evidence was found of this conversion, neutrino was thought to be distinct from its antiparticle (the

antineutrino)[2].

As more experiments were being conducted on understanding the nature of weak interactions, indications of parity violation in Kaon decays emerged. Several possible tests to confirm parity violation in weak interactions were proposed by Lee and Yang [12] in 1956. In a pioneering experiment conducted by Wu *et al.* [13] asymmetry in the distribution of electrons emitted from polarized ^{60}Co nuclei was observed proving that parity was maximally violated weak interactions. Following this discovery, new theories in maximal parity violating Vector-Axial (V-A) structure of weak interactions were developed by Sudarshan, Marshak [14] and Feynman, Gell-Mann [15] separately. This theory predicts that neutrinos are left-handed and antineutrinos are right-handed. In 1958, V-A theory was directly confirmed for neutrinos by Golhaber, Grodzins, and Sunyar [16].

There were two experimentally observed charged lepton counterparts to the neutrino at the time of its discovery—namely the electron and the muon. This raised a question of whether an antineutrino generated in the reaction associated with an electron is the same as the one that is associated with a muon. In 1962, Lederman along with Schwartz and Steinberger discovered the existence of the muon neutrino (ν_μ) at the BNL Alternating Gradient Synchrotron (AGS) [17]. Proton beams produced from AGS hit a Beryllium target at 15 GeV generating pions which decayed into muons and antineutrinos. When these antineutrinos were introduced into a spark chamber, only muons were observed and no electrons were observed. In addition to concluding that there are two types of neutrinos, it further led to the idea of the individual lepton number conservation[3].

[2]It must be noted that this is only true in case of neutrinos being Dirac particles. Neutrinos could still be their own antiparticles if they are Majorana particles.

[3]It is to be noted that the individual lepton number is shown to not be conserved in case of neutrino oscillations.

Standard Solar Model (SSM) was proposed by Bahcall [18] in 1964 which predicted neutrino flux from the sun. Around the same time, Davis *et al.* conducted a radiochemical experiment at the Homestake mine [19] to measure solar neutrino flux by measuring the number of Argon atoms produced by the interaction described in Eq. 2.4 when the solar neutrinos are captured on Chlorine atoms. The neutrino flux predicted in SSM was about three times higher than that observed in the Homestake experiment. This mismatch came to be known as the Solar Neutrino Problem (SNP).

Pontecorvo and Gribov proposed [20] neutrino oscillations as a solution to the SNP. They suggested that a neutrino produced in an electron flavor could be transformed into a muon flavor. By that time Maki, Nakagawa, and Sakata already developed a 2x2 mixing matrix to describe the mixing between two flavors of neutrinos [21]. Although the mixing matrix has changed since its inception, this was the first theoretical step in the direction of neutrino oscillations. The Homestake experiment ran for over 30 years with many improvements in the detector technology, but the discrepancy persisted. Other experiments like the reactor experiment conducted in 1970s by Reines et al. [22] started to favor the neutrino oscillation paradigm. Search for neutrino oscillations intensified in the 1990s with experiments like SAGE [23], GALLEX [24], and GNO [25] observed ν_e capture on Gallium by

$$\nu_e + {}^{71}\mathrm{Ga} \rightarrow e^- + {}^{71}\mathrm{Ge}. \tag{2.5}$$

These experiments also showed a deficit in the solar neutrino flux in the low energy region.

In 1983 Kamiokande [26], a large water Cherenkov detector was built to search for proton decay. Although no evidence of the proton decays was found, the collaboration realized that the detector was sensitive to neutrinos. After upgrades, the detector was repurposed and named Kamiokande-II and started collecting neutrino data in 1985. The Kamiokande-II experiment found a deficit of solar neutrinos in 4–15

MeV range [27] supporting the neutrino oscillation hypothesis. To verify the neutrino oscillation hypothesis, Super-Kamiokande (Super-K) experiment, a successor to the Kamiokande experiment was built to search for neutrino oscillations by observing solar and atmospheric neutrinos. The first evidence of the atmospheric neutrino oscillations was found in 1998 by the Super-K [28] experiment. To extend the results from the Kamiokande-II experiment, Sudbury Neutrino Observatory (SNO) was designed to detect solar neutrinos using heavy water as the target. Heavy water has an advantage of being sensitive to all the three neutrino flavors. In 2002, the SNO experiment provided definitive proof for the neutrino oscillations as the right interpretation of the SNP [29].

Meanwhile, the Direct Observation of Nu Tau (DONUT) collaboration at Fermi National Laboratory had announced [30] the discovery of tau neutrino (ν_τ) in 2001 giving the Standard Model (SM) its current leptonic picture. The mixing matrix was then extended to include ν_τ.

In the past two decades there has been a significant amount of progress in understanding of the neutrino oscillations. The current status of the experimentally determined neutrino oscillation parameters are provided in the Tab. 2.1. In addition to refining the known oscillation parameters, the nature of neutrinos (Dirac or Majorana) [31–36], their mass ordering ($m_3 > m_{1,2}$ or $m_3 < m_{1,2}$) [37–43], their absolute mass scale [44, 45], and CP-violation(δ_{CP}) [37, 38] are being investigated experimentally.

2.3 Neutrinos in and Beyond the Standard Model

The Standard Model of particle physics is a gauge theory based on the gauge symmetries $SU(3)_c \bigotimes SU(2)_L \bigotimes U(1)_Y$. Weak interactions are based on $SU(2)_L$ gauge group where the subscript L indicates that the field is chiral and the field acts differ-

Table 2.1. Experimentally determined neutrino oscillation parameters [46]. The values shown in the braces are for the inverted hierarchy.

Parameter	Best-fit	3σ range
$\Delta m^2_{21}(10^{-5}\text{eV}^2)$	7.37	$6.93 - 7.96$
$\Delta m^2_{31(23)}(10^{-3}\text{eV}^2)$	2.56(2.54)	$2.45(2.42) - 2.69(2.66)$
$\sin^2\theta_{12}$	0.297	$0.250 - 0.354$
$\sin^2\theta_{23}$	0.425(0.589)	$0.381(0.384) - 0.615(0.636)$
$\sin^2\theta_{13}$	0.0215(0.0216)	$0.0190(0.0190) - 0.0240(0.0242)$
δ/π	2σ : 1.38(1.31)	$1.0(0.92) - 1.9(1.88)$

ently on left- and right-handed particles. Whereas left-handed fermions transform as doublets, right-handed fermions transform as singlets under this transformation. Neutrinos are spin 1/2 leptons in the SM and they do not interact via electromagnetic or strong forces. Three generations of neutrinos each a counterpart of the corresponding charged lepton exist.

The SM fermions are represented by 4-component Dirac spinor fields (ψ) which can be decomposed into left- and right-chiral components, ψ_L and ψ_R respectively. The mass term in the Lagrangian for a Dirac fermion couples left and right chiral fields and can be written as

$$\mathcal{L} = -m_D\ (\overline{\psi}_R\psi_L + \overline{\psi}_L\psi_R). \tag{2.6}$$

This term can be generated through Higgs mechanism and explicitly breaks chiral symmetry. In the SM, the neutrinos were initially formulated to be massless because right-handed neutrinos are not found as suggested by the Dirac mass term. But neutrino oscillations have established that at least two of the three generations of neutrinos are massive. Neutrinos could obtain mass through Dirac mechanism similar

to the other fermions through a Yukawa coupling to the Higgs field

$$\mathcal{L} = -m_D \ (\overline{\nu}_R \nu_L + \overline{\nu}_L \nu_R). \tag{2.7}$$

But since neutrino masses are known to be uncommonly small (10^{-3} eV), the Yukawa coupling of the neutrino has to be ∼8 orders of magnitude smaller than that of the electron—the lightest known particle after the neutrino.

Because neutrinos have no charge, they could also have Majorana mass term [47] described by

$$\mathcal{L} = -m_M \ (\nu_L^{c^T} C \nu_L^c + \overline{\nu}_L^c C \overline{\nu}_L^{c^T}) \tag{2.8}$$

where C is the charge conjugation operator $\psi_L^c = C(\overline{\psi}_R^T)$. If both Dirac and Majorana terms exist, the Lagrangian can be written as

$$\mathcal{L} = \begin{pmatrix} \nu_L & \nu_L^c \end{pmatrix} \begin{pmatrix} m_L & m_D \\ m_D & m_R \end{pmatrix} \begin{pmatrix} \nu_L \\ \nu_L^c \end{pmatrix}. \tag{2.9}$$

For $m_L = 0$, the eigenvalues of the mass matrix end up being m_D^2/m_R and m_R. If $m_R \sim 10^{16}$ GeV, the value of $m_D^2/m_R \sim 10^{-3}$ eV which gives an elegant explanation for the neutrino masses being uncommonly low. This way of generating low neutrino mass is called the See-Saw mechanism [48].

The misalignment between the neutrino mass and the flavor eigenstates implies that the neutrinos undergo oscillations. The Lagrangian involving charged current neutrino interactions with leptons can be written as

$$\mathcal{L} = \frac{-g}{2\sqrt{2}} \sum_{\alpha,i} [\bar{l}_\alpha \gamma^\mu (1-\gamma_5) \nu_\alpha W_\mu^- + \overline{\nu}_\alpha \gamma^\mu (1-\gamma_5) l_\alpha W_\mu^+], \tag{2.10}$$

where g is the weak coupling constant, $\alpha = e, \mu, \tau$ are the flavor eigenstates, $i = 1, 2, 3$ are the mass eigenstates, l stands for a charged lepton, ν for a neutrino, and $W^\pm$ stand

for W Bosons. This Lagrangian can also be written in the neutrino mass eigenbases as,

$$\mathcal{L} = \frac{-g}{2\sqrt{2}} \sum_{\alpha,i} [\bar{l}_\alpha \gamma^\mu (1-\gamma_5) U_{\alpha i} \nu_i W_\mu^- + \overline{\nu}_i \gamma^\mu (1-\gamma_5) U_{\alpha i}^* l_\alpha W_\mu^+]. \tag{2.11}$$

Where, $U_{\alpha i}$ is a unitary matrix that transforms mass eigenbases to flavor eigenbases. This matrix is called Pontecorvo-Maki-Nakagawa-Sakata (PMNS) matrix and can be written as

$$U_{\text{PMNS}} = \begin{pmatrix} U_{e1} & U_{e2} & U_{e3} \\ U_{\mu 1} & U_{\mu 2} & U_{\mu 3} \\ U_{\tau 1} & U_{\tau 2} & U_{\tau 3} \end{pmatrix}. \tag{2.12}$$

For the sake of convenience, this matrix was historically divided into several pieces in terms of their mixing angles and has been used as

$$U_{\text{PMNS}} = \begin{pmatrix} 1 & & \\ & c\theta_{23} & s\theta_{23} \\ & -s\theta_{23} & c\theta_{23} \end{pmatrix} \begin{pmatrix} c\theta_{13} & & s\theta_{13}e^{-i\delta} \\ & 1 & \\ -s\theta_{13}e^{-i\delta} & & c\theta_{13} \end{pmatrix} \begin{pmatrix} c\theta_{12} & s\theta_{12} & \\ -s\theta_{12} & c\theta_{12} & \\ & & 1 \end{pmatrix} \begin{pmatrix} e^{i\xi_1/2} & & \\ & e^{i\xi_2/2} & \\ & & 1 \end{pmatrix}, \tag{2.13}$$

where $c\theta_{ij} = \cos\theta_{ij}$ and $s\theta_{ij} = \sin\theta_{ij}$, θs stand for the mixing angles, δ is the CP-violating phase, $\xi 1$,and $\xi 2$ are the Majorana phase terms. According to this matrix, a neutrino produced in one flavor eigenstate after traveling some distance in vacuum has a non-zero probability of being observed in a different flavor eigenstate. The probability of this transformation is given by

$$\begin{aligned} P(\nu_\alpha \to \nu_\beta) =& \delta_{\alpha\beta} - 4 \sum_{i>j} \text{Re}(U_{\alpha i}^* U_{\beta i} U_{\alpha j} U_{\beta j}^*) \sin^2(\frac{\Delta m_{ij}^2 L}{4E}) + \\ & 2 \sum_{i>j} \text{Im}(U_{\alpha i}^* U_{\beta i} U_{\alpha j} U_{\beta j}^*) \sin(\frac{\Delta m_{ij}^2 L}{2E}). \end{aligned} \tag{2.14}$$

Where $\Delta m^2_{ij} = m^2_i - m^2_j$, L is the neutrino path length and E is the energy of the neutrino. It is important to note that $P(\nu_\alpha \rightarrow \nu_\beta)$ is non-zero only when Δm^2_{ij} is non-zero. This implies that the observation of oscillations between two flavors is proof that at least one of the neutrinos must have non-zero mass. By tuning the values of L and E, a two neutrino oscillation approximation can be achieved:

$$P(\nu_\alpha \rightarrow \nu_\beta) \simeq \delta_{\alpha\beta} - \sin^2 2\theta_{\alpha\beta} \sin^2(\frac{\Delta m^2 L}{4E}). \tag{2.15}$$

In fact, many neutrino detectors exploit this approximation to search for neutrino oscillations and measure specific terms in the PMNS matrix. The experimentally determined values of various terms in the PMNS matrix are shown in the Tab. 2.1.

2.3.1 Sterile Neutrino Oscillations and Implications. Sterile neutrinos are fermions that transform as singlets under the $SU(2)_L$ transformation which means that they don't take part in the weak interactions. But sterile neutrino states can mix with active neutrino states. Sterile neutrinos could manifest as part of natural extensions to the SM to explain the neutrino masses as described in the Sec. 2.3. In theory, there are no restrictions on the number of sterile neutrinos that could be included in the extensions of the SM. One or more of these neutrinos could be at the Grand Unified Theory scale and could explain the relatively small masses of the active neutrinos. It could mean that more sterile neutrinos—if they exist—could be at ∼eV scales leading to noticeable distortions in short baseline oscillation experiments.

Adding sterile neutrinos would mean extension to the unitary matrix $U_{3\times3} \rightarrow U_{N\times N}$. Considering the simplest case of one additional sterile neutrino introduces three new mixing angles, two new CP-violating phases, and one Majorana phase term. Following the Eq. 2.14 and neglecting solar and atmospheric terms, the oscillations at short baselines can be approximated to a two neutrino case

$$P(\nu_\alpha \rightarrow \nu_\beta) \simeq \delta_{\alpha\beta} - \sin^2 2\theta_{\alpha\beta} \sin^2(\frac{\Delta m^2_{14} L}{4E}). \tag{2.16}$$

In case of reactor neutrino experiments which look for $\overline{\nu}_e$ disappearance, this can be written as

$$P(\overline{\nu}_e \to \overline{\nu}_e) \simeq 1 - \sin^2 2\theta_{14} \sin^2(\frac{\Delta m^2_{14} L}{4E}). \tag{2.17}$$

Detailed phenomenology and the implications of eV-scale sterile neutrinos could be found in the Refs. [49, 50].

CHAPTER 3

REACTOR NEUTRINOS AND NEUTRINO ANOMALIES

Nuclear reactors are intense sources of $\overline{\nu}_e$ producing $\sim 10^{20}$ $\overline{\nu}_e \mathrm{GW}_{th}^{-1}\mathrm{s}^{-1}$. Antineutrinos are produced when the unstable daughters of neutron-induced fissions undergo beta decay.

$$n \rightarrow p + e^- + \overline{\nu}_e. \tag{3.1}$$

Most nuclear reactors use Uranium (^{235}U and ^{238}U) and Plutonium (^{239}Pu and ^{241}Pu) isotopes as the primary[4] fissionable fuel.

3.1 Reactor Antineutrino Experiments

Reactors have historically played an important role in neutrino physics. As mentioned in the Sec. 2.1, Savannah River experiment (SRP), a reactor $\overline{\nu}_e$ experiment was the first to establish the existence of neutrinos[5]. [9, 51] Several reactor $\overline{\nu}_e$ experiments since as early as 1959 have started measuring neutrino cross-sections [52–57] and showed agreement with the V-A theory. In 1980 Reines *et al.* [22] while conducting neutrino experiments with heavy water as the target at 11.2 m baseline at SRP noticed that the ratio of charged versus neutral current interactions disagreed with the predicted value at 2–3σ. Considering this 'instability' in the traveling neutrino to arise from oscillations, the amplitude and frequency of the oscillations were estimated to be $22^\circ < \theta < 32^\circ$ and $0.7 < \Delta m^2 < 1.0$ eV^2 respectively. They concluded that it was important to perform more reactor experiments to measure the $\overline{\nu}_e$ spec-

[4]These four primary isotopes contribute to more than $\sim 99.9\%$ of the $\overline{\nu}_e$ in a typical commercial reactor.

[5]For the rest of the thesis, anywhere the term 'neutrino' is used in context of reactor experiments, it should be considered as $\overline{\nu}_e$.

trum as a function of distance before drawing any conclusions. They also noted that atmospheric and solar neutrino experiments would help identify the phenomenon of oscillations at higher energies. The oscillation claim was later withdrawn citing that the results were indicative but inconclusive [58].

The oscillation hints from SRP in addition to the solar neutrino problem motivated another reactor $\overline{\nu}_e$ experiment at Institut Laue-Langevin (ILL) in Grenoble [59]. They used a 377 liter segmented detector with ^{3}He-filled wire chamber neutron detectors sandwiched between cells of liquid scintillator at a distance of 8.5 m from a 57 MW enriched ^{235}U reactor. Employing time-delayed coincidence technique and topological cuts, the IBD was measured. Meanwhile, since one of the biggest constraints for reactor $\overline{\nu}_e$ experiments is the lack of precise absolute $\overline{\nu}_e$ spectrum, a β spectrum measurement of the fissile isotopes ^{235}U, ^{239}Pu, and ^{241}Pu were made at the ILL facility using a magnetic spectrometer [60–62]. To date, these beta spectrum measurements are used as a standard in modeling the reactor $\overline{\nu}_e$ flux. A conversion approach (described in depth in Sec. 3.2) was used to determine $\overline{\nu}_e$ spectrum from the measured β spectrum. The measured spectrum by the ILL experiment found good agreement with this β-converted $\overline{\nu}_e$ model.

The ILL detector was modified and placed close to the Gösgen reactor and measurements were performed at three different baselines by moving the detector, making it a multibaseline experiment. The multiple baseline approach takes advantage of the relative $\overline{\nu}_e$ spectra to isolate the results from reactor and detector related systematic uncertainties. The measured $\overline{\nu}_e$ spectrum and rates were found to be in good agreement with the corresponding β-converted $\overline{\nu}_e$ values.

To make a high statistics neutrino spectrum measurement in search for neutrino oscillations, several detectors were deployed near the 2800 MW Bugey nuclear reactor in France between 1980 and 1996 [63–66]. In one such high statistic experi-

ment, Bugey measured neutrino spectrum at 15m, 40m, and 95m baselines. It was the first reactor $\overline{\nu}_e$ experiment to use liquid scintillator doped with ^{6}Li as the target to aid in efficient background reduction. The Bugey detector also used similar segmentation to the other experiments. Their $\overline{\nu}_e$ measurements were also in agreement with the predictions from the β-converted $\overline{\nu}_e$ spectrum. In addition, they also placed limits of $1 \times 10^{-2}\text{eV}^2$ and 2×10^{-2} on Δm^2 and $\sin^2 2\theta$ [65] respectively.

Meanwhile, motivated by indications of reactor $\overline{\nu}_e$ oscillations and to measure cross-sections, several experiments in varying configurations were conducted at the Rovno nuclear powerplant in Russia [54–56, 67]. The Rovno experiment employed several detectors with varying technologies at 18-25 m baselines and measured $\overline{\nu}_e$ from the 1375 MWth Rovno nuclear reactor from 1983 to 1990. Total IBD yields and decomposed IBD yield of ^{235}U was calculated [54,67] based on the measured $\overline{\nu}_e$ rates. The measured yields showed decent agreement with the theoretical values at the time considering large theoretical and experimental uncertainties.

Another Russian experiment searching for oscillations at lower oscillation frequencies was also performed at multiple baselines from multiple reactors at the Krasnoyarsk power plant using a single detector. Composed of hexagonal prism of polyethylene as the target and ^{3}He counters as the detectors several $\overline{\nu}_e$ measurements were performed at multiple distances (33–231) m. In addition to showing that the measured flux was in agreement with the predicted values, they were also able to exclude significant amount of the oscillation parameter space [57, 68].

In the 1990s, atmospheric neutrino experiments showed hints of ν_μ oscillations with a large mixing angle θ_{23} favoring $\overline{\nu}_e$ disappearance at kilometer scale wavelengths. In search for oscillations at this scale, CHOOZ, a reactor $\overline{\nu}_e$ experiment was setup in France near the CHOOZ power station [69]. The CHOOZ detector used Gadolinium-loaded liquid scintillator as an inverse beta decay target region and a time-delayed

coincidence method for the background reduction. CHOOZ placed limits on oscillation parameters $\Delta m^2 > 7 \times 10^{-4}\text{eV}^2$ for maximal mixing and $\sin^2 2\theta = 0.1$ for large Δm^2. During the same time, another reactor neutrino experiment called Palo Verde was conducted in Arizona at a distance of 800m from the Palo Verde reactor complex. The Palo Verde experiment employed a detector segmentation system similar to Bugey, but much bigger in size and used Gadolinium-loaded liquid scintillator as the target. The Palo Verde experiment saw no oscillation [70] and excluded similar parameter space as CHOOZ.

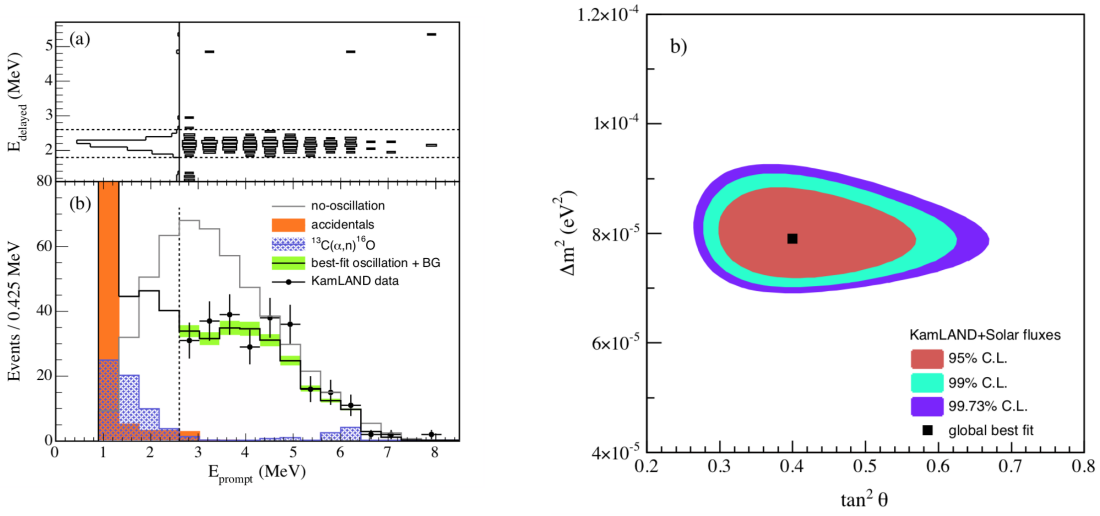

Figure 3.1. Results from a 2005 report from the KamLAND collaboration [71]. (left) The prompt energy spectrum of $\overline{\nu}_e$ events clearly showing a deviation in the shape from the null oscillation hypothesis. (right) KamLAND-suggested best-fit point and oscillation parameters Δm^2_{21} and $\tan^2\theta_{12}$.

A very long baseline $\overline{\nu}_e$ experiment, Kamioka Liquid Scintillator Antineutrino Detector (KamLAND) was built in Kamioka [71] to increase the electron-neutrino oscillation parameter coverage. Surrounded by 53 commercial reactors and located at a flux-weighted distance of 180 kilometers from those reactors, this one kiloton liquid scintillator improved on the existing time-delayed coincidence technique between positrons and neutrons. The first result reported using 145 days of data showed a deficiency in expected antineutrinos favoring oscillations. In conjunction with the solar

neutrino data, the best-fit oscillations were found at $\Delta m^2_{21} = 7.9^{+0.6}_{-0.5} \times 10^{-5}$ eV^2 and $\tan^2\theta_{12} = 0.40^{+0.10}_{-0.07}$ as seen in the Fig. 3.1. With more data, increased fiducial volume, and reduced systematic uncertainties improvements were found in their subsequent measurements.

Increasing evidence in favor of non-zero value of mixing angle θ_{13} from accelerator experiments T2K [72] and MINOS [73] motivated an increased number of multi baseline reactor $\overline{\nu}_e$ experiments. Meanwhile, Double CHOOZ [74], a successor to CHOOZ with a single detector presented its initial measurement of the last mixing angle $\sin^2\theta_{13} = 0.086^{+0.041}_{-0.041}(\text{stat})^{+0.030}_{-0.030}(\text{syst})$ in 2012. The Daya Bay $\overline{\nu}_e$ experiment is the first experiment to precisely measure the value of the last mixing angle θ_{13} in 3-neutrino mixing model. Following Daya Bay's measurements, the RENO and Double CHOOZ experiments also measured θ_{13} precisely. Daya Bay, Double Chooz, and RENO use similar detector designs and perform a similar relative spectral shape measurement to search for the neutrino oscillations. Although θ_{13} is measured last, it is currently the best-known mixing angle with the current best limit [75] of $\sin^2 2\theta_{13} = 0.0856 \pm 0.0029$ from the Daya Bay experiment.

3.2 Reactor Antineutrino Spectrum

As already mentioned, reactors typically use IBD interaction to measure neutrinos. It is given by

$$\bar{\nu}_e + p \rightarrow e^+ + n. \tag{3.2}$$

It is a charged current quasi-elastic interaction mediated by the weak force via the transmission of the W^+ boson. IBD interaction is a threshold interaction with the minimum neutrino energy required for the interaction given by

$$E^{\min}_{\bar{\nu}_e} = m_n + m_{e^+} - m_p. \tag{3.3}$$

Taking $m_{e^+} = 0.511$ MeV, $m_p = 938.272$ MeV, and $m_n = 939.565$ MeV [46],

$$E_{\bar{\nu}_e}^{\min} = 1.804 \text{ MeV}. \tag{3.4}$$

The recoil kinetic energy of the neutron has been neglected in the above calculation. Including this small contribution would raise the threshold to 1.806 MeV.

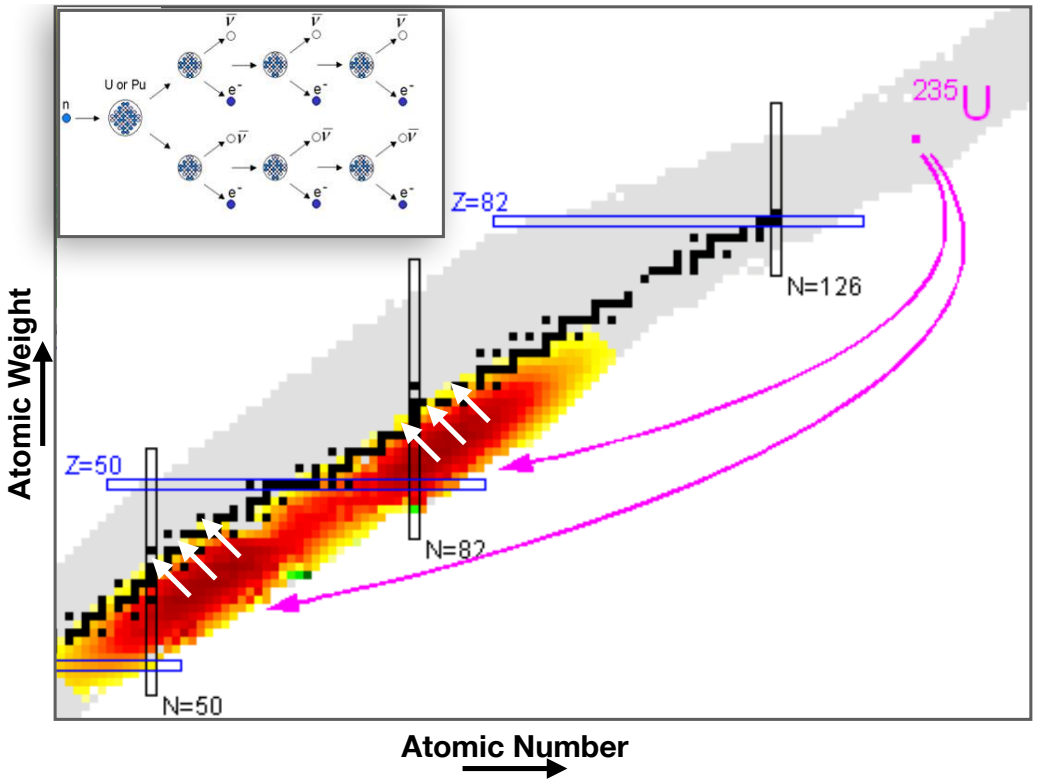

Figure 3.2. Schematic of the fission (pink arrows) and subsequent β decays (white arrows) of ^{235}U [76]. ^{235}U is the primary contributor of the $\overline{\nu}_e$s originating from a typical nuclear reactor. The color scale on the plot indicates the probability of production of the given fission product. Shown in the inset is a schematic of the $\overline{\nu}_e$ production arising from a neutron-induced fission. On average, 6 $\overline{\nu}_e$ are produced per fission.

The IBD reaction has relatively high cross-section and the IBD positron energy is uniquely correlated with the incoming $\overline{\nu}_e$ energy [77]. An IBD interaction is typically detected by tagging a positron and a neutron in coincidence providing a clean signature while enabling high background reduction. The positron signal is detected with a minimum energy of $E_{\text{rec}}^{\min} = 1.022$ MeV which arises from the positron-electron

annihilation in the detector. The neutrino energy can be retroactively reconstructed based on the positron energy by

$$E_{\overline{\nu}_e} = E_{\rm rec} + (E^{\rm min}_{\overline{\nu}_e} - E^{\rm min}_{\rm rec}) = E_{\overline{\nu}_e} + 0.782 \text{ MeV}. \tag{3.5}$$

Nuclear reactors produce neutrinos from the fission and subsequent β decays of the fission fragments. Power reactors have a combination of the ^{235}U, ^{239}Pu, ^{238}U, and ^{241}Pu isotopes with <20% ^{235}U enrichment and hence are called low enriched uranium (LEU) reactors. Although fuel in these reactors is primarily composed of the ^{238}U isotope, ∼60% of the $\overline{\nu}_e$ originating from these reactors are from ^{235}Usince it has higher fission cross-section at the relevant neutron energies. Currently for security reasons, only research reactors are permitted to use Highly Enriched Uranium (HEU[6]) fuel. Reactor $\overline{\nu}_e$ spectrum can be written as

$$S(E_{\overline{\nu}_e}) = \frac{W_{\rm th}}{\sum_i f_i e_i} \sum_i f_i \frac{dN_i}{dE_{\overline{\nu}_e}}, \tag{3.6}$$

where $W_{\rm th}$ is the thermal power of the reactor and the f_i, e_i, and $dN_i/dE_{\overline{\nu}_e}$ are the fission fraction[7], the effective energy released per fission, and the cumulative neutrino spectrum respectively for the i^{th} fission isotope [78].

$W_{\rm th}$ is calculated quite accurately using the temperature of the coolant and it's flow rate. f_i as a function of time are calculated typically using detailed proprietary simulations. e_i are calculated using the energy produced in the fissions taking into account the extra energy released by the neutron captures on the reactor material and the energy carried away by $\overline{\nu}_e$. The total energy released by all the major fission isotopes are showed in the Tab. 3.1.

---

[6]All reactors that use a fuel with more than 20% ^{235}Uenrichment are classified as HEU reactors.

[7]The number of fissions by the isotope as a fraction of total fissions

Table 3.1. The total fission energy (MeV/fission) for dominant fission isotopes [79].

	^{235}U	^{239}Pu	^{238}U	^{241}Pu
E_{Tot}	202.79±0.06	205.93±0.13	207.32±0.08	211.04±0.12

The $\overline{\nu}_e$ spectrum, $\frac{dN_i}{dE_{\overline{\nu}_e}}$ from each individual isotope is the major source of uncertainty. Following the terminology presented in the Ref. [80], assuming a detailed knowledge of the beta decays of the fission fragments and their fission yields, the fission $\overline{\nu}_e$ spectrum for each isotope could be theoretically determined by summing up the $\overline{\nu}_e$ spectra contributions of all the individual beta decays as

$$\frac{dN_i}{dE_{\overline{\nu}_e}} = \sum_n Y_n(Z,A) \sum_{n,i} b_{n,i}(E_0^i) P_{\overline{\nu}_e}(E_{\overline{\nu}_e}, E_0^i, Z). \tag{3.7}$$

Here, $Y_n(Z,A)$ is the fission yield of the isotope with the atomic number Z and weight A and characterizes the number of beta decays at any point of time. $b_{n,i}$ is the branching ratio and $P_{\overline{\nu}_e}(E_{\overline{\nu}_e}, E_0^i, Z)$ is the normalized $\overline{\nu}_e$ energy spectrum from the isotope n,i. This method of summing up the $\overline{\nu}_e$ contributions from all the beta decays is often referred to as the *ab initio* or the summation method. Shown in the Fig 3.3 are the *ab initio* spectra from the four major isotopes.

In practice, there are several issues with spectra determined using *ab initio* method. The $\overline{\nu}_e$ spectrum from a reactor is composed of $\sim$ 1000 daughter isotopes with $\sim$6000 beta branches. Lack of information on the branching ratios of several isotopes in addition to large uncertainties in the fission yields and possible systematic errors in nuclear calculations leads to over 10% uncertainty in $\overline{\nu}_e$ spectrum using summation calculations. A more detailed description of the the difficulties and issues with the summation calculation and several insights into the calculated spectra can be found in Ref. [78, 80, 84–86]

To work around the difficulties associated with the *ab initio* spectrum, another

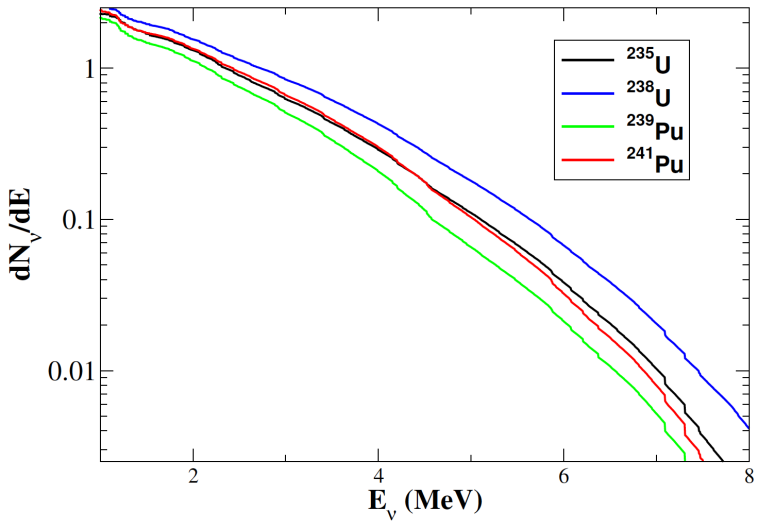

Figure 3.3. The $\overline{\nu}_e$ spectra ($\frac{dN_i}{dE_{\overline{\nu}_e}}$) for the four major fissioning isotopes determined using the *ab initio* method [80]. The fission yields were taken from the JEFF-3.1.1 [81] fission fragment yield database and the ENDF/B-VII.1 decay library [82, 83].

method for determining $\frac{dN_i}{dE_{\overline{\nu}_e}}$ for each individual fission isotope was formulated [60, 87]. In this method, the β spectra are measured by irradiating thin foils of the fissioning isotopes with neutrons. Starting from the highest energy, the measured aggregate β spectra could be successively fit to the virtual beta branches in Fermi-Kurie representation to obtain an endpoint distribution $\{a_i, E_0^i\}$ for each virtual beta branch.

$$\frac{dN_i}{dE_e} = \sum_i a_i P(E, E_0^i, \overline{Z}(E_0^i)). \tag{3.8}$$

where a_i is the amplitude of the virtual beta branch and $\overline{Z}(E_0^i)$ is a function describing the empirical mean proton number of the fission products with the beta branch endpoint energy E_0^i.

The beta branches obtained this way could then be individually converted to $\overline{\nu}_e$ energy and summed as

$$\frac{dN_i}{dE_{\overline{\nu}_e}} = \sum_i a_i P(E_0^i - E, E_0^i)\overline{Z}(E_0^i). \tag{3.9}$$

Table 3.2. One example of the parameters for the analytical approximations of the fission $\overline{\nu}_e$ energy spectra.

a_i	^{235}U	^{239}Pu	^{238}U	^{241}Pu
a_0	0.870	0.896	0.976	0.793
a_1	-0.160	-0.239	-0.162	-0.080
a_2	-0.0910	-0.0981	-0.0790	-0.1085

The obtained $\overline{\nu}_e$ spectrum depends to some extent on the assumptions made about the spectral shapes and the allowed/forbidden energy levels during the conversion process. This process of determining the $\overline{\nu}_e$ spectrum from the measured β spectrum is called *conversion* approach. The most widely used predictions for ^{235}U, ^{239}Pu and ^{241}Pu $\overline{\nu}_e$spectra are from a conversion approach [88].

Another approach attempting to take advantage of both the *ab initio* and the conversion approaches was developed recently. The $\overline{\nu}_e$ and β spectra are determined using *ab initio* approach whenever experimental data are available. The difference in the measured and the *ab initio* β spectra is then fit to virtual beta branches which are then used to convert back to the $\overline{\nu}_e$ spectrum. In addition to the above mentioned methods, purely analytical approximations are used occasionally for convenience. An example of the analytical approximation presented in [89] is given as

$$\frac{dN}{dE_{\overline{\nu}_e}} = \exp(a_0 + a_1 E_\nu + a_2 E_\nu^2), \tag{3.10}$$

and shown in Tab 3.2.

The IBD spectrum accessible to a detector can be estimated using the predicted $\overline{\nu}_e$ spectrum and the IBD cross-section. Shown in the Fig. 3.4 is the oscillation-suppressed predicted IBD spectrum. The IBD cross-section is an increasing function of the energy whereas the $\overline{\nu}_e$ spectrum decreases with energy. It is worth noting

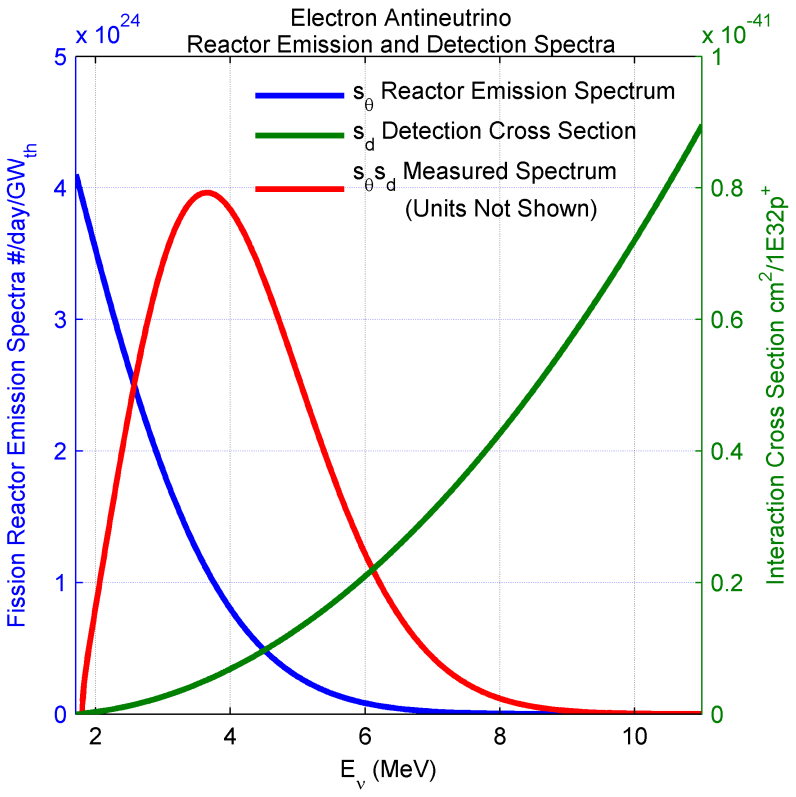

Figure 3.4. An illustration of the IBD spectrum (in red) accessible to a detector as a function of energy [90]. It is obtained by taking product of the IBD cross-section (in green) and reactor $\overline{\nu}_e$ emission spectrum (in blue).

that most ($\sim 75\%$) of neutrinos generated in a nuclear reactors have energies below the IBD threshold and hence go undetected by a detector that uses this detection mechanism. Including the oscillation and the detector response effects, the measured $\overline{\nu}_e$ spectrum can be written as

$$\frac{dN}{dE_{\overline{\nu}_e}} = N_p \eta(E_{\overline{\nu}_e}) \sigma(E_{\overline{\nu}_e}) \frac{P_{ee}(E_{\overline{\nu}_e}, L)}{4\pi L^2} S(E_{\overline{\nu}_e}), \tag{3.11}$$

where N_P is the number of target protons, $\eta(E_{\overline{\nu}_e})$ is the energy-dependent detector efficiency, $\sigma(E_\nu)$ is the energy-dependent IBD cross-section, P_{ee} is the $\overline{\nu}_e$ survival probability, L is the baseline, and $S(E_{\overline{\nu}_e})$ is the $\overline{\nu}_e$ spectrum originating from the reactor.

3.3 Anomalies in the Reactor Neutrino Sector

Predictions of the $\overline{\nu}_e$ rates and the spectra date back to late 1950s [91]. Given the lack of knowledge of individual β decay spectra [92], the earliest predictions have typically used the conversion method [52, 91]. With the improved knowledge of the β decays, attempts were made to perform *ab initio* $\overline{\nu}_e$ predictions in 1970s and early 1980s [93–96]. Predictions performed by different groups showed disagreements based on the inputs. Additionally, the predicted spectra had big uncertainties [94] for the $\overline{\nu}_e$ energies above 4 MeV. In early 1980s, dedicated campaigns of β spectra measurements at the ILL reactor were performed to predict the $\overline{\nu}_e$ spectra using the conversion method [60–62, 97]. These measurements are still the source for the reactor $\overline{\nu}_e$ conversion predictions. ^{238}U undergoes fission only when irradiated with fast neutrons and hence has only been measured recently [98]. Further, the measured β energy spectrum from ^{238}U fission only spans 2.875 to 7.625 MeV. Consequently, the *ab initio* method is used for ^{238}U prediction.

There has been renewed interest in the reactor $\overline{\nu}_e$ predictions in the past few years. Motivated by the need for a precise reactor $\overline{\nu}_e$ spectrum for the Double CHOOZ (far detector only) experiment, the $\overline{\nu}_e$ spectra calculations were revisited [99]. The hybrid approach described in the Sec 3.2 for ^{235}U, ^{239}Pu, and ^{241}Pu and a pure summation approach for ^{238}U were used to calculate the $\overline{\nu}_e$ spectra. These calculations reported an increase in the predicted flux by $\sim$3% compared to the previous predictions. A complementary work including higher order corrections by Huber [88] using the conversion approach also showed an increase in the predictions by $\sim$2–3%. Although the observed event rates from the $\overline{\nu}_e$ experiments remained the same, with a change in the predicted event rates, there is a systematic shift in the ratio of number of the measured versus the expected $\overline{\nu}_e$ events as shown in the Fig. 3.5. This deficit in the observed flux came to be called the *Reactor Antineutrino Anomaly* (RAA) [100]. Fluxes reported by the θ_{13} experiments Daya Bay [101], Double CHOOZ [102], and RENO [103] conducted after the RAA was uncovered also show disagreement with

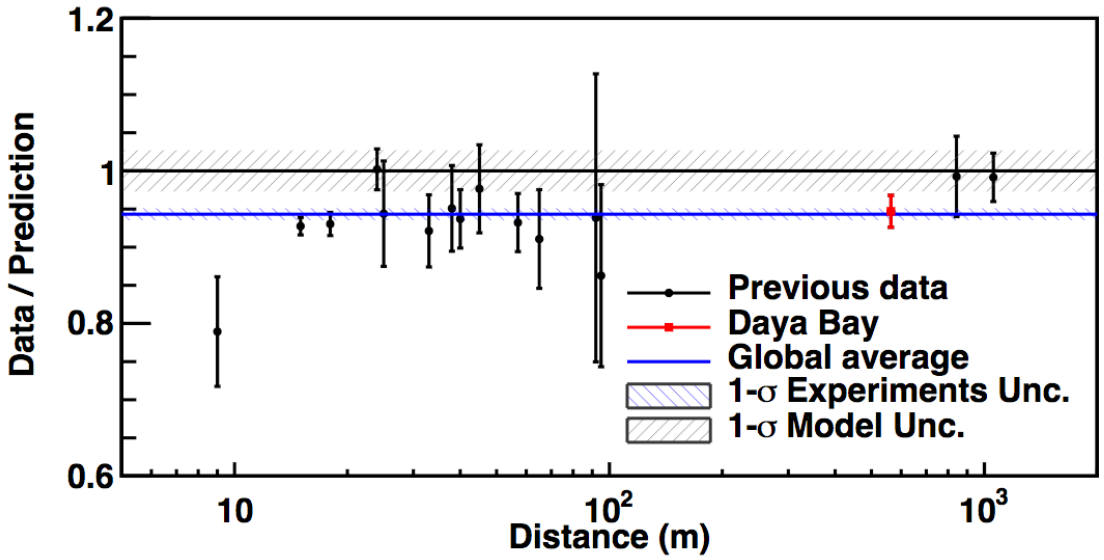

Figure 3.5. Ratio of the fluxes observed versus the new flux predictions for several reactor neutrino experiments [104].

the predictions.

Various interpretations of the anomaly are explored in the Refs. [80,84,85,105, 105–111]. The deficit in the measured flux compared to the prediction could primarily arise from either incorrect flux predictions or some new underlying physics. It was pointed out [80] that the uncertainties in the analysis of the reactor anomaly that arises from structure of forbidden transitions are too high to infer an anomaly. The accuracy of ILL beta spectrum measurements has been brought to question [109].

An additional sterile neutrino being the cause for the RAA [112,113] is strongly motivated in the context of the other anomalies observed in the accelerator and the source neutrino sectors. For sterile neutrino to be reason for the anomaly, they should mix with SM neutrinos. Sterile neutrino mixing leads to high frequency oscillations as shown in the Fig. 3.6. Sterile neutrino oscillations suggested by the anomalies in the other sectors also prefer oscillations at high frequencies.

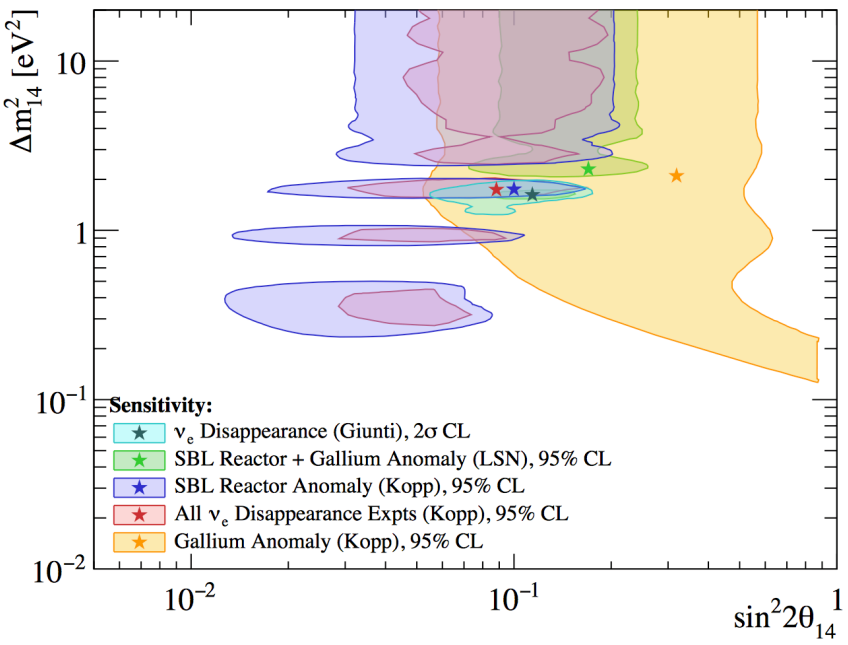

Figure 3.6. The oscillation parameter space suggested by the RAA. Fits include reactor flux data as well as the Gallium anomaly data.

Daya Bay experiment has recently measured the evolution of measured flux as a function of time [114]. Since fission fractions evolve with time in a power reactor, correlations between the measured flux and varying fission fractions were used to measure the IBD yields of ^{235}U and ^{239}Pu. The measured IBD yields showed disagreement with the predictions, in particular for ^{235}U. RENO also recently reported IBD yield measurements generated from flux evolution similar to Daya Bay and showed disagreement with predictions [103] as well. A combination of the evolution measurements and previous reactor flux measurements [108, 110] show that either a combination experiments are wrong, ^{238}U prediction is off by 2σ, or it is a combination of sterile neutrinos and wrong predictions. Several possible explanations for the flux anomaly are put forward but no conclusions are successfully drawn so far with the existing data.

In addition to the flux anomaly, the shape of the reactor $\overline{\nu}_e$ spectrum measured

at LEU reactors [115–118] were found to disagree with the predictions. These shape differences could not be explained by the existence of the sterile neutrinos and hence point out mistakes in the predictions [78, 80, 84–86, 119]. It could be possible that one isotope is the cause for the anomaly or all the isotopes contribute to the shape distortion. Additionally, since a conversion method to compare to the experimental data, it is also possible that a mistake in the conversion method or the underlying beta spectra could have led to wrong predictions in the predicted $\overline{\nu}_e$ spectra.

3.4 Anomalies Hinting at Sterile Neutrinos in Other Sectors

eV-scale sterile neutrinos were hypothesized before RAA was proposed as a possible explanation for the results from the Liquid Scintillation Neutrino Detector (LSND) experiment. LSND [120] was an experiment built at Los Alamos to look for oscillations from a pure $\overline{\nu}_\mu$ beam from Los Alamos Meson Physics Facility to a $\overline{\nu}_e$ beam. The LSND experiment reported an excess in the $\overline{\nu}_\mu \rightarrow \overline{\nu}_e$ appearance channel. In a similar L/E parameter space to the LSND analysis, the Mini-Booster Neutrino Experiment (MiniBooNE) experiment [121] also observed an event excess in $\nu_\mu \rightarrow \nu_e$ and $\overline{\nu}_\mu \rightarrow \overline{\nu}_e$. Although, the $\overline{\nu}_\mu \rightarrow \overline{\nu}_e$ measurement from the MiniBooNE favors a sterile neutrino in the $\Delta m^2 \sim 1$ eV^2, the $\nu_\mu \rightarrow \nu_e$ measurement from the same experiment disfavors it.

During calibration measurements, the solar neutrino detectors GALLEX [24] and SAGE [23], using intense neutrino sources of ^{51}Cr and ^{37} Ar, observed an event deficit of $\sim$24% in the ν_e disappearance channel. This event deficit referred to as the Gallium anomaly can also be explained by a sterile neutrino with the $\Delta m^2 \sim 1$ eV^2. Although interesting in its own right, the discussion on the sterile neutrinos in other sectors is beyond the scope of this thesis.

After the discrepancies between measured and predicted fluxes were pointed

out in 2011 and 2012, there was a flurry of activity in reactor neutrino community to search for sterile neutrinos using reactors. Several experimental proposals were put forward with slightly different detector designs and using either HEU or LEU reactor. The current state of the search for sterile neutrinos using reactors includes experiments that have already run their course, experiments collecting data and have put forward the initial results, and other experiments are collecting data and are actively working on analyzing the data. In a short period of time, most of the suggested parameter space will be covered by these experiments and will be able to resolve anomalies in the reactor neutrino sector.

CHAPTER 4

PROSPECT EXPERIMENT

In chapter 3, anomalies that plague the reactor neutrino sector are discussed. Existing experimental data doesn't provide conclusive statements about the reasons for the anomaly and hence new experimental evidence is needed to decipher the source of the anomalies. PROSPECT takes two pronged approach in resolving the reactor anomalies. The primary goals of the PROSPECT experiment are to search for sterile neutrinos that are hinted by the flux anomaly and measure the HEU $\overline{\nu}_e$ spectrum to resolve the spectrum anomaly. The PROSPECT experiment is located at the Oak Ridge National Laboratory (ORNL) in Tennessee. Located at a closest distance of approach of $\sim$7 m from the neutrino source, the experiment was designed to search for meter scale oscillations. PROSPECT utilizes ^{6}Li-loaded liquid scintillator as the target and IBD reaction as the detection mechanism.

4.1 HFIR as the Source of $\overline{\nu}_e$

The source of $\overline{\nu}_e$ for the PROSPECT experiment is HFIR. Operating since the 1960s, this research reactor has been primarily used for neutron scattering experiments, sample irradiations, neutron activation analysis, and radioactive isotope production for medical and industrial purposes. It is a Highly Enriched Uranium (HEU) reactor [124] with a ^{235}U enrichment of $\sim$93%. A mockup of HFIR reactor and the simulation of the distribution of the fissions in the reactor are shown in Fig. 4.1 Being a research reactor, HFIR is different from typical commercial reactors in the following ways:

1. **Size**: Research reactors are typically not used for power generation and hence are not typically compact. Compact reactors are particularly suited to search

Table 4.1. Parameters of the PROSPECT detector.

	Parameter	Value
Reactor	Power	85 MW
	Shape	cylindrical
	Radius	0.2 m
	Height	0.5 m
	Fuel	HEU
	Duty cycle	∼47% reactor on
Detector	Dimension	$\sim 2.0 \times \sim 1.6 \times \sim 1.2$m
	Scintillator volume	∼3.7 ton
	Closest distance	∼7m
	Baseline coverage	∼2 m (when stationary)
	Energy resolution	4.5% at 1 MeV
Segmentation	Quantity	14(horizonal)×11(vertical)
	Cross-section	0.145m×0.145m
	Position Resolution	0.145m(transverse), 0.05m(longitudinal)

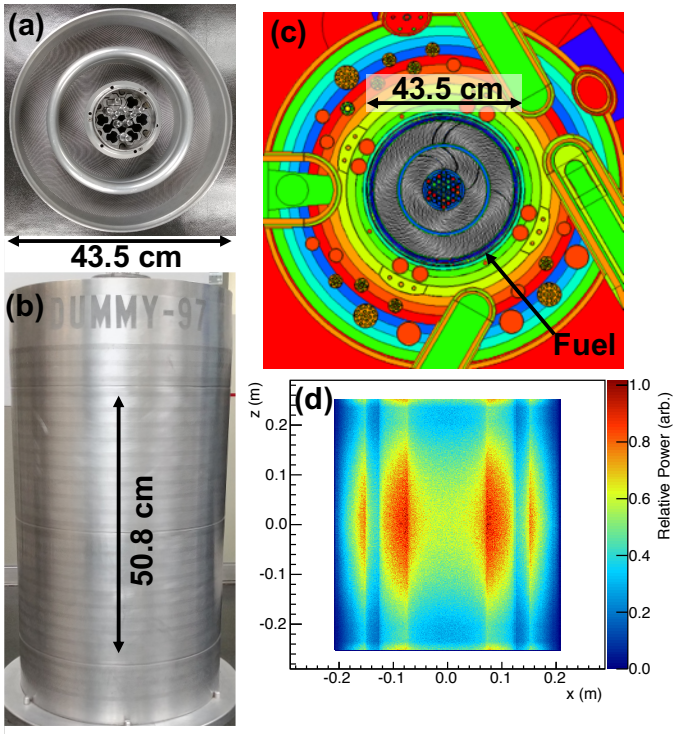

Figure 4.1. Top(a) and side(b) views of a mockup of the HFIR core [122]. c) A Monte Carlo N-Particle code (MCNP) simulation of the HFIR reactor core. d) Distribution of fissions in the core of HFIR.

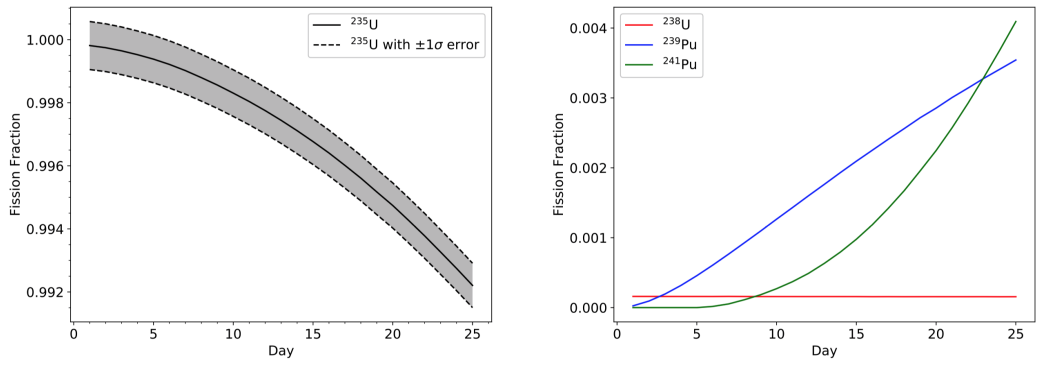

Figure 4.2. MCNP simulation [123] of the evolution of fission fractions of ^{235}U (left) and other major fission isotopes(right) in HFIR over the duration of a single cycle. The contribution from ^{235}U is >99% throughout the cycle whereas the other isotopes contribute <0.5% each.

for short baseline high frequency oscillations because the oscillation washout from the core size is minimal.

2. $\overline{\nu}_e$ **flux**: Since the research reactors are compact, they comprise smaller amount of fuel which in turn implies that the $\overline{\nu}_e$ flux is smaller than the commercial reactors.

3. **Fuel content**: The high ^{235}U enrichment of research reactor implies that a large fraction of the $\overline{\nu}_e$ originate from ^{235}U [123] as opposed to a typical commercial reactor where $\overline{\nu}_e$ originate from a combination of four primary fission isotopes.

4. **Cycle duration**: The length of the reactor cycles for research reactors are typically much shorter than that of commercial reactors. Shorter cycles provide the ability to measure cosmogenic backgrounds at close intervals in time. They also constrain the evolution of fission fractions in the reactor and provides a cleaner single isotope $\overline{\nu}_e$ flux as shown in the Fig. 4.2.

4.1.1 Backgrounds at the HFIR. One of the challenges for the PROSPECT experiment is the cosmogenic and reactor-related backgrounds. The detector's close proximity to the HFIR means that natural overburden cannot be used to shield the cosmogenic backgrounds. The HFIR facility provides very little overburden of $\sim$0.5m concrete [125]. High energy cosmogenic neutrons in particular are notorious for mimicking IBDs in the PROSPECT detector. The detector's close proximity to the HFIR also implies that the reactor related backgrounds should also be carefully considered. Detailed background measurements [125] have shown that a well-designed targeted passive shielding highly suppresses the reactor related backgrounds. Reactor off background measurements could then be used to perform cosmogenic background subtraction.

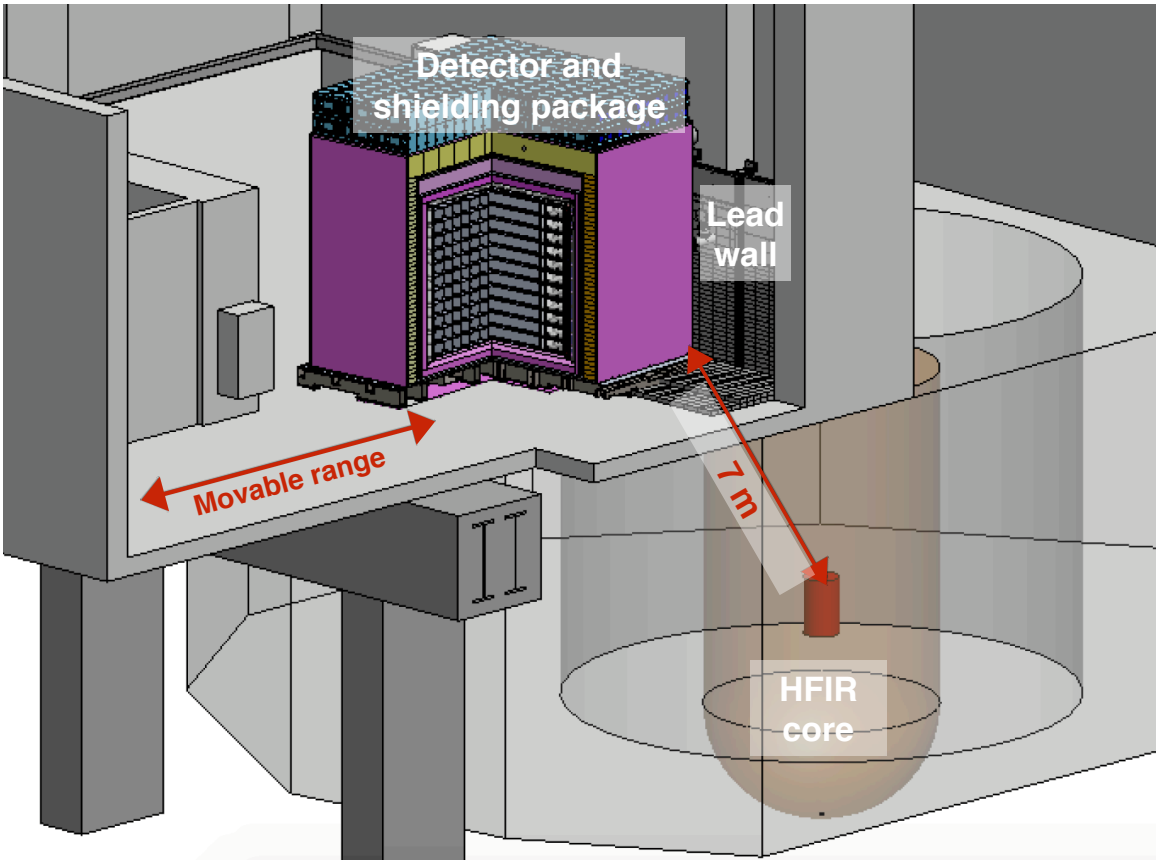

Figure 4.3. Schematic of the PROSPECT detector, the movement and the shielding package in the HFIR facility. The movable range of the detector in the facility is also shown. The electronics rack which is mounted on the side of the detector is not shown in the figure.

4.2 PROSPECT Detector

The PROSPECT detector design is optimized to search for meter scale oscillations. Motivated by the previous studies [126], a few parameters have been identified that prompted the PROSPECT detector design. Design choices were further motivated by the need to reduce cosmogenic and reactor backgrounds. The PROSPECT detector schematic is shown in the Fig. 4.3 and the parameters are shown in Tab. 4.1.

From inside to outside, PROSPECT detector package is composed of:

- Inner detector

- Inner shielding and containment
- Outer shielding and detector movement system
- Electronics.

The following sections give detailed description of the detector subsystems.

4.2.1 Inner Detector. Inner detector includes all the detector components that are inside the containment system. It is composed primarily of the liquid scintillator, the optical grid, the PMTs, the calibration system, and the segmentation support system.

4.2.1.1 Lithium Doped Liquid Scintillator. PROSPECT is a compact on-surface detector. To reach the physics goals, the design requires pulse shape discrimination (PSD) capable liquid scintillator with high light yield. The PSD capability of the liquid scintillator would allow for the discrimination of nuclear recoils from the electron recoils thus helping in background rejection. High light yield of the liquid scintillator allows for good energy resolution. Since the detector is compact, the neutron capture agent used in the detector must be capable of compact neutron capture energy depositions.

PROSPECT uses a novel ^{6}Li-doped liquid scintillator (LiLS) as the target. A commercially available di-isopropylnapthalene (DIN)-based scintillator, EJ-309 [127] was used as the base. In addition to the PSD capabilities and high light yield, EJ-309 is non-toxic and has high flash point and is ideal for deployment in a reactor facility. EJ-309 was modified by adding wavelength shifting agents 2,5-diphenyloxazole (PPO) and 1,4-bis(2-methylstyryl) benzene (bis-MSB) and by doping it with 0.1% ^{6}Li using an ether-based glycol surfactant and a 9.98 mol/L aqueous solution of lithium chloride with 95% enriched ^{6}Li.

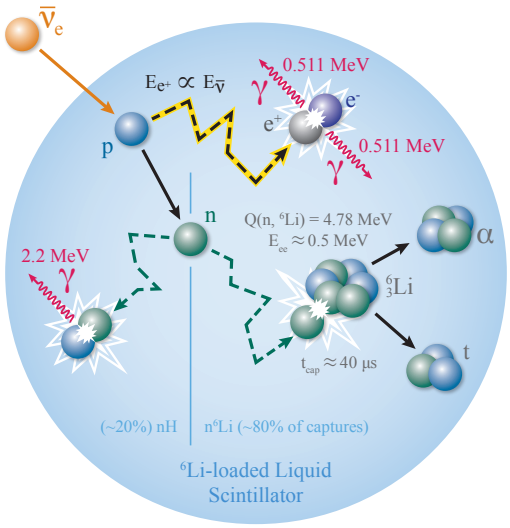

Figure 4.4. Schematic of the IBD interaction in the PROSPECT detector.

The $\overline{\nu}_e$ from the reactor interacts with the protons in the Hydrogen-rich liquid scintillator and via the IBD interaction producing a positron and a neutron:

$$\overline{\nu}_e \ + p \rightarrow e^+ + n. \tag{4.1}$$

The positron deposits all it's kinetic energy in the detector and annihilates with an electron to produce two gammas producing a signal in the visible wavelength. This signal—called the prompt signal—is detected by the PMTs.

$$e^+ + e^- \rightarrow \gamma + \gamma. \tag{4.2}$$

The neutron thermalizes by scattering on several protons in the liquid scintillator and captures on a ^{6}Li atom (and occasionally on a Hydrogen atom) to give rise to a tritium and an alpha with specific energies of 2.05 MeV and 2.75 MeV respectively:

$$n + ^6\text{Li} \rightarrow \alpha + ^3_1\text{H}. \tag{4.3}$$

Both the tritium and the alpha deposit their energy almost instantaneously produces a flash of light (also called delayed signal) which is also detected by the

PMTs. The time separation between the prompt and the delayed signals has a typical signature of $< 100\mu$s and provides a time-coincidence that can be used to reject uncorrelated background events. This, in addition to PSD provides good background rejection capabilities. The schematic of the IBD interaction in the PROSPECT detector is shown in the Fig. 4.4.

Comprehensive long term tests were performed to choose the materials that come in contact with the LiLS in the detector. Samples were soaked in small vials of LiLS for long periods of time and periodic visual and UV-absorption tests were performed. A comprehensive list of compatible materials was established following this procedure.

4.2.1.2 Optical Grid. PROSPECT is a segmented detector optically separated into a 11(vertically)×14(horizontally) grid of 154 segments. To maintain the uniformity in response throughout the detector as well as to reduce the dead volume, PROSPECT utilizes a novel segmentation design. The optical separation was achieved by the use of custom designed multi-layer optical separators. Long 3D printed rods hold the optical separators in place and give them the proper structure. The rods were also designed to provide internal access to the calibration sources. A schematic of the optical grid is shown in the Fig. 4.5 and an in depth discussion of its design is provided in the Sec. 5.

4.2.1.3 PMT Modules. The PROSPECT detector employes PMTs placed at either end of each segment to collect scintillation light. Two kinds of PMTs—Hamamatsu R6594 SEL(Hamamatsu) and ADIT Electron Tubes 9372KB(ET) are used in the detector as shown in the Fig. 4.6.

The PMTs were housed in mineral oil-filled acrylic boxes with square cross-section to maintain compatibility with the LS, reduce background noise, and include

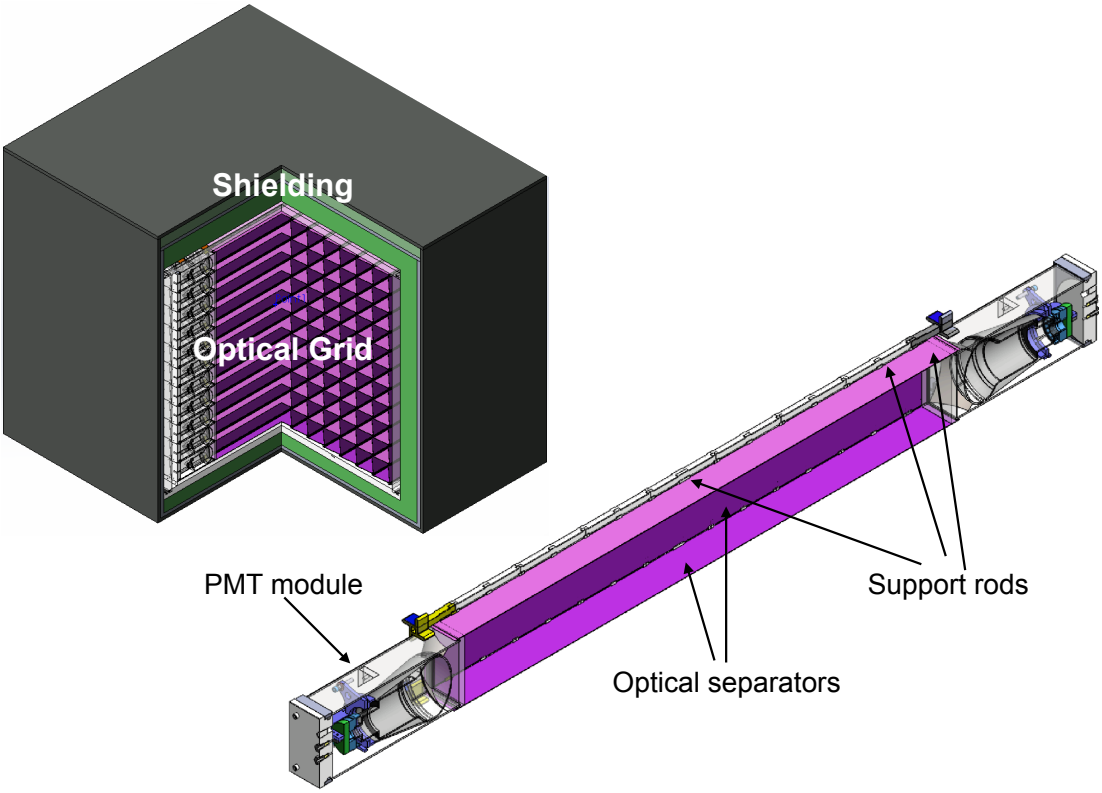

Figure 4.5. (left) Cutaway view of the inner detector showing cross-sections of segments. (right) Section view of a segment showing optical separators, PMT modules, and support rods.

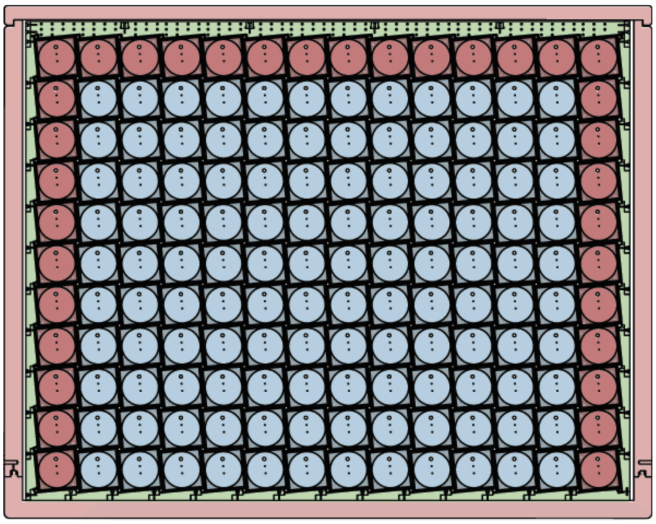

Figure 4.6. Schematic showing the positioning of Hamamatsu and ET PMTs in the detector. Tests with prototypes have shown that the Hamamatsu PMTs have superior performance and consequently are used in the fiducial volume of the detector.

a buffer region. The acrylic tubes were fabricated by gluing together acrylic pieces using Acryfix. UVT acrylic is used as the material for the front window to allow for light over a wide range of wavelengths. A conical reflector was used as a light guide to route light from the segment with a square cross-section to the PMTs with a circular cross-section. Once assembled, the PMTs were filled with mineral oil and sealed shut. A schematic of all the components used in the PMT modules is shown in the Fig. 4.7 and more details about the PMT modules can be found in the Ref. [128].

4.2.1.4 Segment Support Wedges. The segmentation design creates a geometry with each segment slightly twisted which makes for a complicated external geometry as shown in the Fig. 4.6. Acrylic was chosen as the structural material to support the optical grid geometry. Machined acrylic parts (called acrylic wedges) support and constrain the PMT housings on the bottom and the sides. In addition, the support rods in the outermost layer are also constrained by acrylic wedges. Two sets of planks (horizontal and vertical) are used to bind the PMT structure together. The horizontal planks are attached to the back of PMT housings and the side horizontal

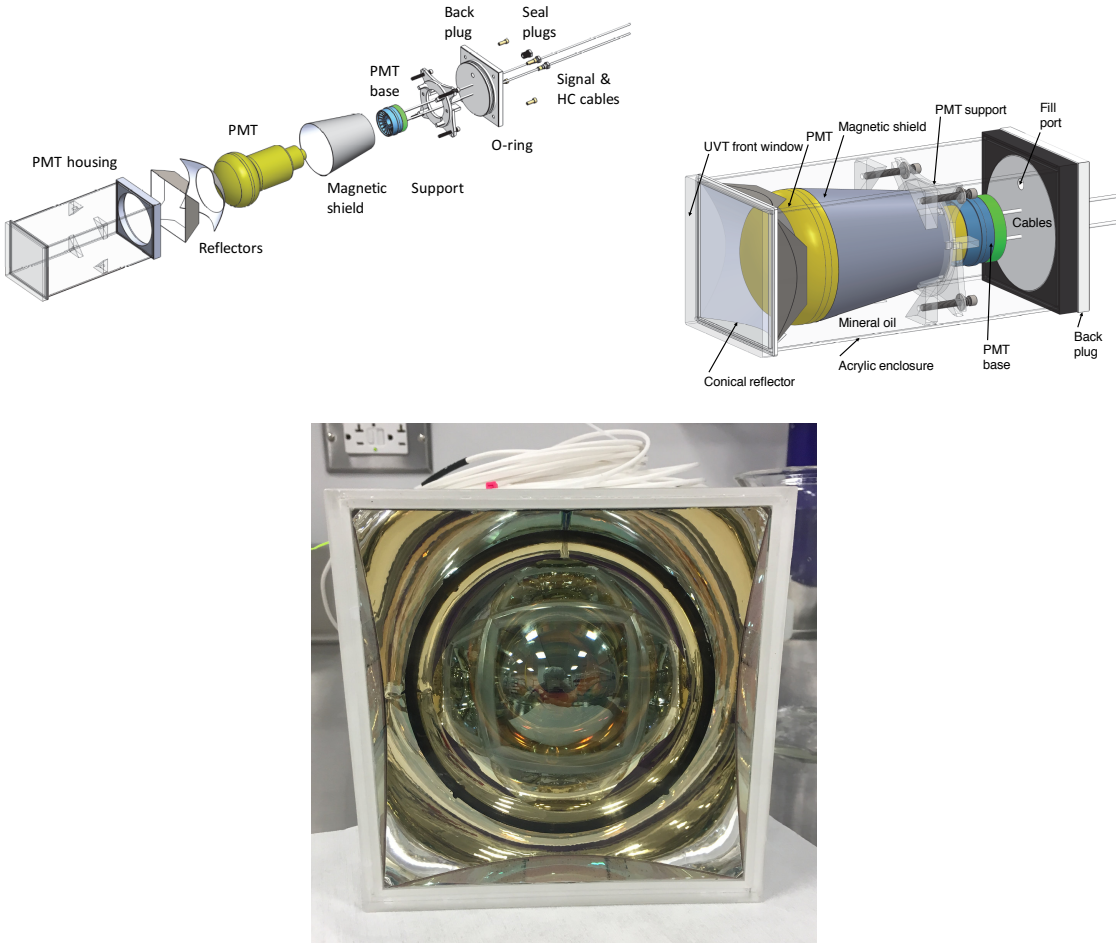

Figure 4.7. PROSPECT PMT module design. Exploded (left) and fully assembled (right) schematic of a PROSPECT PMT module. (bottom) Front view of a fully assembled PMT module.

wedges to constrain the housings relative to the outer geometry and relative to each other. The vertical planks are mounted on the horizontal planks to constrain the relative motion of horizontal planks. These planks are designed to allow for the PMT cables and calibration tubes to be fed out of the detector.

4.2.2 Containment System. The reactor facility requires that a double containment system be incorporated into the design of the detector to avoid leakage of the liquid. Hence two level containment system was designed where only the inner level comes in contact with the LS.

4.2.2.1 Inner Containment Vessel. Similar to the bottom and side supports, the inner containment vessel was also fabricated using acrylic. The vessel is manufactured with a slab at the bottom, tank on the side, and a lid on the top. The inside of the vessel is 1.995 m×2.143 m in cross-section and 1.555 m in height with the bottom slab and the side tank made of 0.0635 m thick acrylic. The bottom slab and the tank have a system of grooves designed to be sealed using two Viton O-rings. A passageway out from the gap between the two seals is used to check for leaks by observing the pressure differential between inside and outside of the containment vessel. The lid on top of the inner containment vessel has several rectangular holes for feedthroughs to accommodate various cables and calibration tubes.

4.2.2.2 Outer Containment Vessel. A second containment vessel of the internal dimensions 2.505 m×2.255 m×1.982 m high was used for LS containment as a redundancy in case of a leak in the first containment vessel. Since LS doesn't come in contact with this containment vessel under normal circumstances, it was made from sheets of aluminum welded at the edges. The acrylic and Aluminum tank have clearance to allow for proper installation of the inner vessel within the outer vessel. Once installed, this gap was filled with borated polyethylene and demineralized water to act as neutron shield. A lid with feedthroughs for instrumentation is placed on the

top and sealed to the walls of the tank using neoprene gasket.

4.2.3 Passive Shielding. As mentioned in the Sec. 4.1.1, most of the IBD mimicking backgrounds come primarily from the cosmogenics, in particular from the high energy neutrons. Background measurements performed using the PROSPECT detector prototypes provided a benchmark for the PROSPECT simulations. Guided by the simulations, a multi-layer shielding package with an additional heavy neutron shielding on the top as shown in the Fig. 4.8 was designed to substantially reduce the cosmogenic neutron backgrounds.

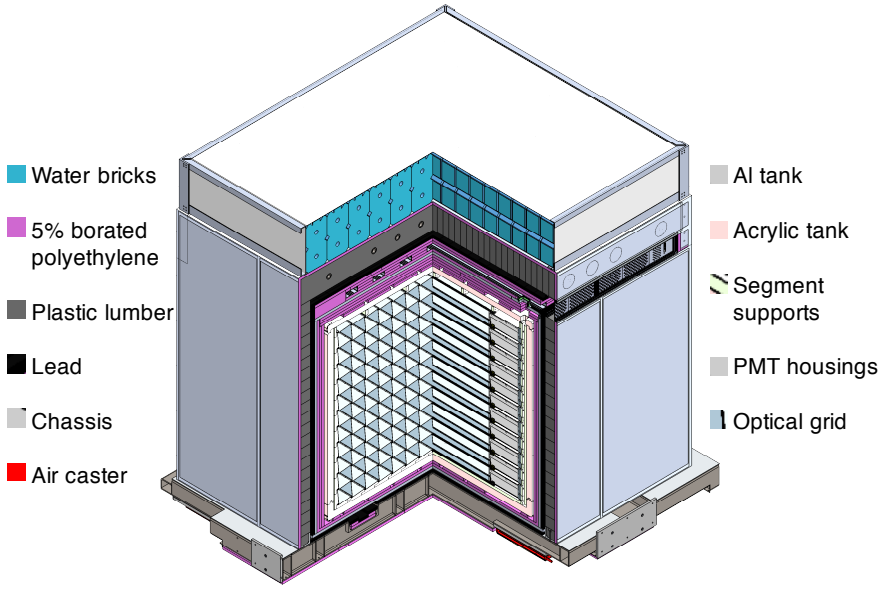

Figure 4.8. Schematic of the PROSPECT multi-layer shielding package. The top layer of the water bricks, the single layer of borated polyethylene, and the plastic acts as a cosmogenic neutron moderator. The layer of lead inside the plastic lumber acts as a generic shielding material. The inner most layer of the borated polyethylene captures the thermal neutrons that are produced from the muon and neutron spallation on the lead in the shielding.

Gamma background measurements [125] performed at the HFIR have identified several hotspots along the concrete wall adjoining the reactor pool. A dedicated

stationary lead wall was installed along the concrete wall to reduce the gamma backgrounds from the reactor and various penetrations in the concrete wall. Simulations performed based on the measured backgrounds have guided the shape, size, and the structure of the shield wall.

4.2.4 Detector Movement System. The whole detector including the shielding package is placed on a 3.242 m×2.946 m×0.21 m steel frame chassis. The frame has c-grooves to allow for the detector to be placed with a forklift and was designed to distribute the weight of the detector uniformly on the floor. It also has allowance for Aerogo air-casters to be placed under the chassis for tilting and moving the filled detector.

4.2.5 Detector Calibration. The segmented design of the detector allows for

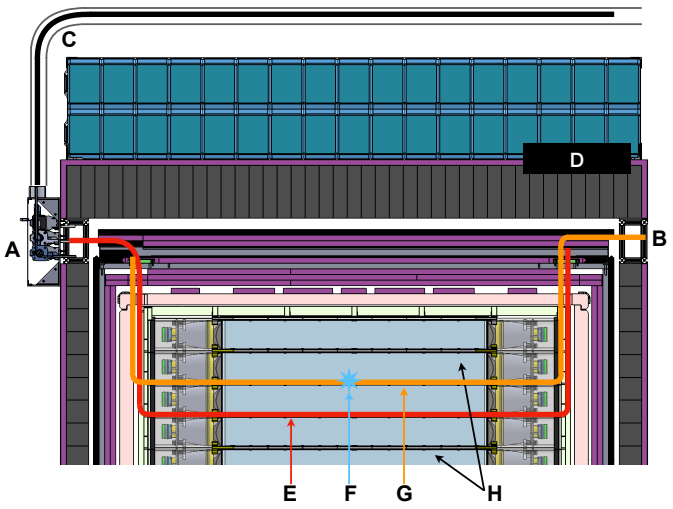

Figure 4.9. The PROSPECT detector optical and source calibration deployment schematics. Shown in orange and red are the instrumented optical and source calibration tubes. In blue is the location of the optical diffuser.

the optical and source calibrations to be placed inside the detector. The calibration of the detector response and its space and time uniformity was surveyed by the use of a combination of sources. The support rods provides access for the *in-situ* optical and source calibrations of the PROSPECT detector. In addition, there are a few

uniformly distributed intrinsic sources in the detector. Optical and Source calibration schematics are shown in the Fig. 4.9.

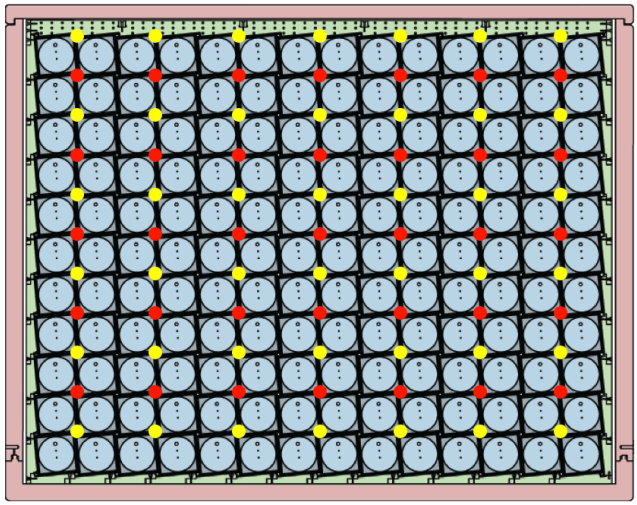

Figure 4.10. The PROSPECT optical and source calibration locations. Yellow dots indicate the deployed locations of the optical sources and red dots indicate the locations that were designed with the capability to deploy radioactive source calibrations.

4.2.5.1 Optical Calibration System (OCS). Optical laser sources were deployed in the detector in an effort to measure the time offset between the PMTs in the same segment, single photoelectric response, and monitor the attenuation length. Light enters the segment via a diffuser which diffuses the light into all the adjoining segments. Diffusers are located along the longitudinal center of the segment and are transfixed in the holes drilled in the center support rods. As shown in the Fig. 4.10, each segment has an optical diffuser at one of its corners and except for the top layer each optical diffuser is shared by four segments.

4.2.5.2 Radioactive Source Calibration System. Similar to the OCS, deployment of the *in-situ* radioactive source calibration is enabled by the presence of the hollow support rods. Unlike the optical calibration system, the radioactive calibration system was designed such that the sources can be deployed at any point along the

length of the segment. Additionally, not all segments have a calibration source adjacent to them as shown in the Fig. 4.10. Sources sealed in an aluminum capsule move inside the teflon tubes instrumented through the support rods during the installation and allows for the sources to move inside the detector longitudinally without coming into contact with the LiLS. The sources could be placed anywhere along the length of the segment within ∼1 cm accuracy and ∼1 mm precision using a timing belt system. Custom designed 3D printed UV-cured resin pulleys are connected to stepper motors to run the timing belt. The sources are encased inside an aluminum capsule which is mounted on to the timing belt. 3D printed belt guides hold the stepper motor-pulley assembly, guides the timing belts, and allows for easy removal and replacement of the sources. The timing belt guides are mounted on the top of the outside of the detector which allows for manual handling of the sources from outside the detector. Extra storage tubes are located on top of the detector to store the timing belt outside the detector when not in use.

4.2.5.3 Volume Calibration using Actinium as the Source. The search for the sterile neutrinos in the PROSPECT experiment is done by comparing the relative $\overline{\nu}_e$ rates as a function of baseline and energy within the detector. Relative segment volume is one of the key systematics in the relative rate comparison. Surveys performed during the assembly have showed a variation in the segment-to-segment volumes within 1%. To provide an *in situ* segment-to-segment volume measurement, the PROSPECT liquid scintillator was uniformly spiked with ^{227}Ac. ^{227}Ac rates provide the relative volume of each segment after filling the LiLS in the scintillator. Furthermore, ^{227}Ac decays also provides a way to continuously monitor the performance of the detector.

Successive αs arising from the decays of ^{219}Rn and ^{215}Po (also called *RnPo*) provide a clean signature of these events. By tracking the rate of $\alpha - \alpha$ coincidences

from RnPo events in individual segments, the rate of ^{227}Ac over time and consequently the relative volume of each segment can be deduced. Additionally, the αs from both Rn and Po could be used to track the uniformity and the stability of various other detector parameters including PSD, energy scaling, resolution, position reconstruction, and energy resolution. 0.5 Bq ^{227}Ac was introduced into the detector by dissolving in the LS an AcCl solution prepared from a commercial Actinium source.

4.2.5.4 Backgrounds as Calibration Sources. Few backgrounds classes could also be used as a source of calibration and to monitor the performance of the detector. Cosmogenic-based backgrounds are extensively employed for calibrating the PROSPECT detector. Muons are one such class of backgrounds which when coupled with the peculiar geometry of the detector can be leveraged to calibrate the timing and the position of the detector. ^{12}B is another source produced from cosmogenic neutron capture on ^{12}C which then beta decays with energy as high as $\sim$13 MeV. Because of the wide β energy range, ^{12}B is very helpful for the energy scale calibration at high energies.

There are naturally occurring radioactive material inherent in the detector that can also be leveraged and can be used to track the position and the energy uniformity and stability. Two such sources used in the PROSPECT are $\beta-\alpha$ coincidences arising from the subsequent ^{212}Bi-^{212}Po and ^{214}Bi-^{214}Po decays collectively called *BiPo*. These BiPo events follow from the decay chains of ^{232}Th and ^{238}U respectively. The energy and the position uniformity and stability can be tracked by tracking the β followed by the α.

^{6}Li is intrinsic to the PROSPECT LiLS and is uniformly distributed throughout the detector volume. Background neutrons capturing on the uniformly distributed ^{6}Li is a great source to perform relative energy scale calibrations as well as to track its stability. A discussion on how each of the above sources are used for calibration

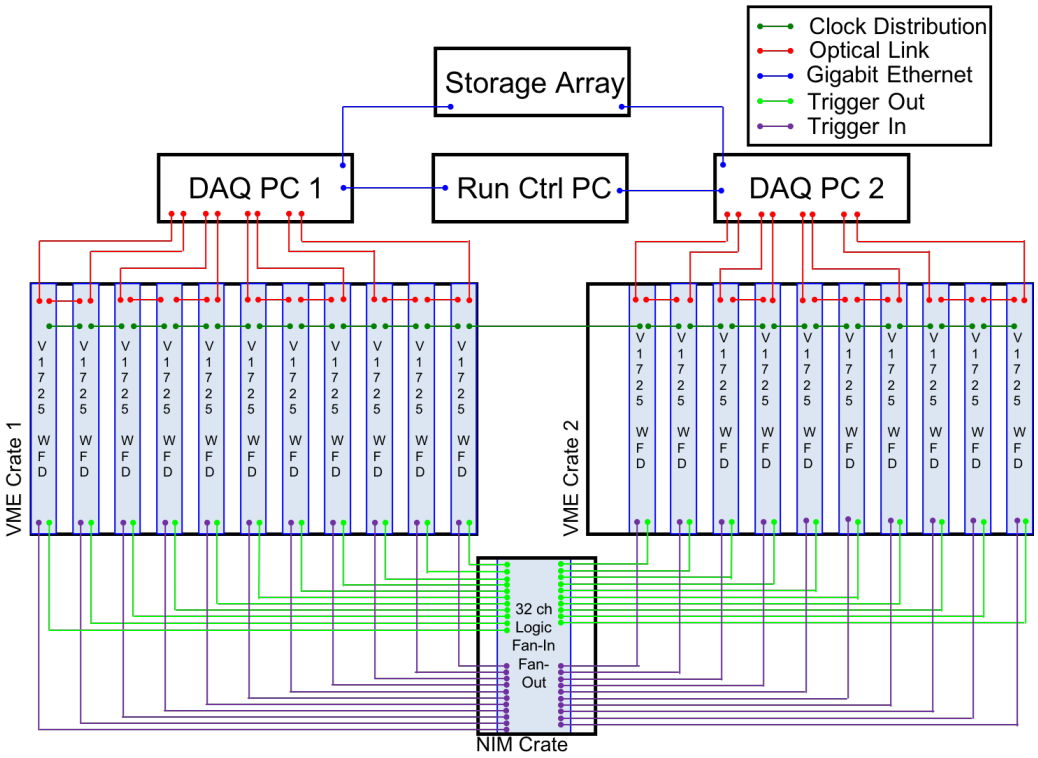

Figure 4.11. The Schematic of the DAQ hardware used in the PROSPECT detector.

and tracking detector performance is presented in the Sec. 6.2.

4.2.6 Electronics and Data Acquisition System. PROSPECT uses CAEN V1725 [129] commercial Waveform Digitizers (WFD) for collecting full waveforms from the PMTs. In addition to providing PSD capability, the 14-bit 250 MHz WFD was chosen to have a wide dynamic range to cover broad energy range while keeping the data collection at manageable rates. A total of 21 WFDs distributed between two Weiner 6023 [130] VME crates are used to cover all 308 PMTs in the detector. The schematic of DAQ hardware used in the PROSPECT detector is shown in the Fig. 4.11.

All PMTs in the detector are triggered if both the PMTs in any segment exceed a threshold of 50 channels (∼100 keV) —called triggering threshold— within 64 ns of each other. The 148 sample long waveforms acquired by each PMT are then

recorded only if they exceed a threshold called zero length encoding (ZLE) threshold of 20 channels ($\sim$ 40 keV). ZLE threshold significantly minimizes the data collection rate by abandoning the uninteresting waveforms.

4.2.7 Detector Monitoring. Several monitors were instrumented into the detector to continuously track and record the health of the detector. A total of 20 high voltage (HV) modules each with 16 channels are used to supply a high voltage bias to all the PMTs. During typical operation, the bias is set at $5{\times}10^5$ with the possibility to vary the gain for calibration or testing. The currents and voltages of the HV is recorded and regularly monitored for any fluctuations.

PROSPECT LiLS is observed to undergo quenching if oxygen dissolves in the LiLS. To avoid the absorption of oxygen in LiLS, nitrogen gas boil-off from a liquid nitrogen dewar continuously flows through the detector to replace the air in the detector. The nitrogen pressure as well as it's flow rate out of the detector is constantly monitored. Additionally, the oxygen and the humidity content are also monitored constantly. The cover gas system is also designed to be able to bubble dry nitrogen through the detector as well to test the acrylic O-ring seals on the acrylic containment.

The temperature of the detector is tracked and recorded every minute at several locations within the detector using resistance temperature detectors. Two ultrasonic sensors at opposite corners of the acrylic tank monitor the level of LiLS at better than 1mm and measure the tilt in the detector during filling. Another ultrasonic sensor is mounted on the inside of the aluminum tank to monitor the water level.

4.3 Detector Assembly

The PROSPECT detector including inner containment and the outer containment was assembled at Wright Laboratory at Yale university. After dry commissioning, the detector was then shipped to HFIR for filling along with the rest of the assembly including shielding. Following the optical grid assembly discussed in Sec. 5.4, top support ribs and vertical bars were mounted. The side acrylic walls were lifted over the assembled inner detector and lowered onto the acrylic base. Calibration tubes and cables were routed through the holes in the acrylic lid and the lid is lowered onto the side walls.

Stainless steel cables were looped around the detector to compress together the sidewalls to the acrylic base. The entire inner detector assembly was lifted and lowered into the aluminum tank lined with borated polyethylene(BPE) liner. The gaps between the acrylic tank and the aluminum tank were shimmed with BPE. After routing the calibration tubes and cables through the aluminum tank lid, it was lowered and bolted to the aluminum tank. The detector is made light- and gas-tight by mounting ICOTEK fittings on the cables and by pouring a potting mixture over the fittings.

Dry commissioning of the detector included PMT functionality checks and OCS measurements for PMT mapping. Additionally, cosmic muon measurements were used as a diagnostic tool to set a standard for the performance of the unfilled detector to be later compared to the performance of the detector after shipping. The fully assembled detector was then packed in a wooden crate for shipping. It was then driven to ORNL in an enclosed air ride trailer with cushioning on bottom and sides. The detector was continuously monitored during shipping for fluctuations in

temperature, humidity, and pressure.

4.4 Detector Installation

The detector received at HFIR was stored under nitrogen cover gas. Another round of dry commissioning was performed and the detector was moved to the desired position before filling with LiLS. The LiLS was produced [131] at Brookhaven National Laboratory and shipped to the HFIR facility. One of the 28 LiLS drums was spiked with ^{227}Acand LiLS from all the drums was then mixed in a thoroughly cleaned 20-ton Teflon-lined shipping container. After filling with the LiLS, the gap between the acrylic tank and the aluminum tank was filled with demineralized water. The detector was filled with 4340 kg of the LiLS and 403 kg of water. Shielding as shown in Fig .4.8 was installed on the detector. Finally, electronics and source calibration motors needed for initial calibration were installed. A detailed description of the assembly, shipping, and installation of the detector can be found in Ref. [128].

4.5 PROSPECT Prototype Detectors

PROSPECT detector has a complicated geometry and uses several novel detection techniques. Several prototypes were constructed in order to determine the design of the components, validate interfacing between them, and characterize various constituents. Multiple configurations of each prototype were produced for various tests and as shown in the Tab. 4.2. The details of the ways in which the prototypes were used in learning valuable lessons and defining the final detector design are discussed in detail in the Refs. [125, 132–136] and are not further discussed here.

Table 4.2. PROSPECT prototypes in the order of increasing detector volume. The locations, timelines, and the specific objectives for each prototype are also listed.

Prototype	Location	Timeline	Capacity (l)	Objective
PROSPECT-0.1 [132]	Yale	2014–2015	0.1	EJ-309 and LiLS characterization
PROSPECT-2 [132]	HFIR	2014–2015	1.7	HFIR background characterization
PROSPECT-20 [125, 134]	Yale/ HFIR	2015–2016	23	HFIR background characterization and scintillator studies
PROSPECT-50 [135]	Yale	2016–2018	50	Design validation

CHAPTER 5

PROSPECT OPTICAL GRID

Optical grid is a key subcomponent of the PROSPECT detector which includes a combination of optical separators and support rods. The purpose of the optical grid is to optically isolate the LiLS into segments while ensuring optimal light transport to the PMTs. In this section a detailed description of the optical grid system is given from the design choices to the assembly of the components in the detector.

5.1 Design of the Optical Segmentation System

The design of the optical grid for the PROSPECT detector is motivated by the following objectives:

- **Efficient light collection:** Efficient light collection is key to good energy resolution.
- **Minimal cross-talk:** Light cross-talk between the segments reduces the accuracy of reconstruction and has to be minimized.
- **Dimensional tolerance:** The volume of each segment has to be well constrained for a relative spectral comparison.
- **Mechanical interfacing:** The detector has intricate design and the components have to interface properly with each other while maintaining tolerances.
- **Mechanically strong and durable:** The structure of the optical grid has to be rigid and be stable during the shipping, movement and regular operations.
- **Minimum inactive volume:** Inactive volume reduces the energy resolution and efficiency of the detector and must be maintained at minimum.

- **Minimal non-reflective surface:** To maintain good light collection at the PMTs, highly reflective surfaces have to be maintained for all the surfaces exposed to the scintillation light.

- **Radiopure:** Radiopure material reduces the chance of intrinsic correlated and accidentals backgrounds.

- **Chemical compatibility with LiLS:** Materials coming into contact should not degrade the LiLS or vice-versa.

- ***in-situ* calibration deployability:** The design has to allow for the optical and radioactive sources to be deployed inside the detector.

After extensive mechanical R&D using several prototypes and using the above guidelines, the final design of the optical grid geometry is as shown in the Fig. 5.1.

5.1.1 Design of Optical Separators. The main functionality of the optical separators (or separators) is to transport any energy depositions in the scintillator to the PMTs. The general design requirements of the optical grid has already been discussed in the Sec 5.1. The following specific requirements were used as guidelines in designing of the optical separators:

- **High Specular Reflectivity:** Prior tests with prototypes [134] have shown that specular reflectors have better uniformity in light collection and PSD performance.

- **Optically opaque:** To reduce the cross-talk between the segments, the separators have to be opaque.

- **Rigid:** To maintain dimensional tolerance and stability, the separators have to be rigid.

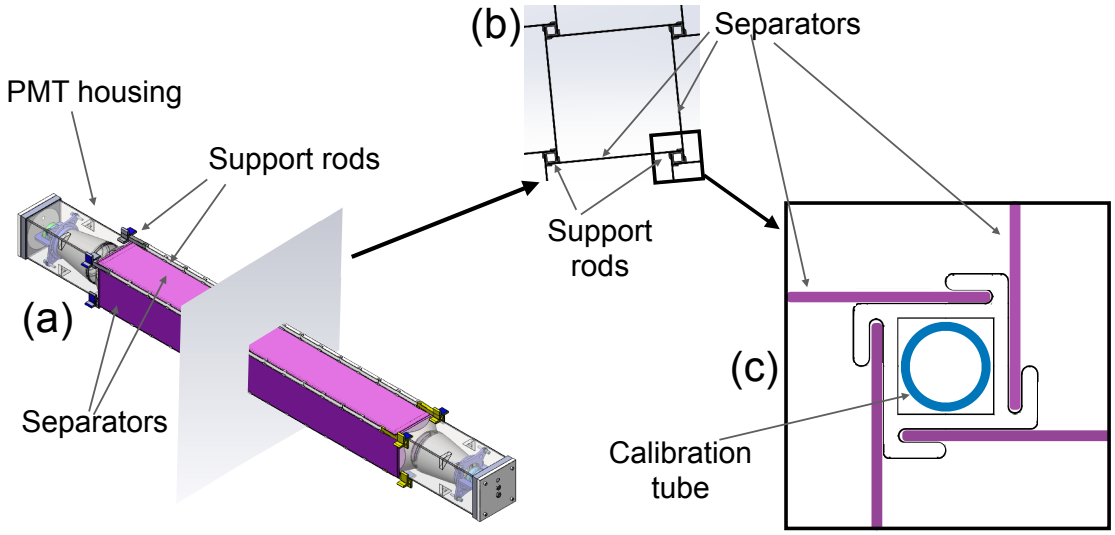

Figure 5.1. Design of the optical grid. (a) Single segment showing the interface between the separators, support rods and the PMT modules. (b) Sectional view of a segment with separator and support rod interface. The tilted design of the optical grid is evident from the figure. Also seen are portions of the adjacent segments. (c) Detailed view showing the positioning of the separators in the support rod tabs. Also shown is the calibration tube.

- **Thin:** Since the contents of the separators are non-scintillating, thinner separators reduces the inactive volume.

Optical separators were produced by laminating together several layers of material to obtain thin highly reflective sandwiches. The schematic of the cross-section of optical separators is shown in the Fig. 5.2. The rigidity is provided by epoxy resin-coated carbon fiber (CF) sheets. Reflectivity is primarily provided by adhesive backed DF2000MA [137] which is laminated on both sides of the CF sheets. Compatibility is enforced by the use of Flourinated Ethylene Propylene (FEP) film. Because of the difference in the refractive indices between FEP and the liquid scintillator, FEP also provides additional total internal reflection for light incident at grazing angles. The interface between DF2000MA and FEP is provided by double-sided adhesive with high optical transparency.

Lamination of all the layers was performed at room temperature using cold roll lamination process utilizing pressure sensitive adhesives. Pressure sensitive adhesives are activated and acquire their adhesive properties when exposed to pressure. Unlike hot roll laminators the adhesives in case of pressure sensitive lamination do not need heat for activation. Cold roll lamination has the following advantages over hot roll lamination.

- Hot roll lamination needs the rollers to be heated to the around 100 °C which could lead to damage to the other constituents of the separator.
- Cold roll lamination is widely used in the sign making industry which provided ample prototyping opportunities.
- Cold roll laminators are commercially available for very low prices and do not typically require expensive components.

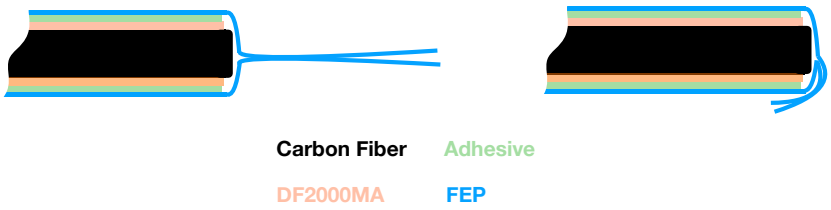

Figure 5.2. Laminated and heat sealed optical separator with excess FEP(left) on the edge and with overhanging FEP folded(right) as used in the assembly.

Epoxy coated Carbon Fiber (CF) sheets have superior characteristics and makes a good choice for the backbone. CF sheets are rigid, light and opaque. Additionally, since the backbone is the bulk of optical separator it is desirable to have materials with low atomic number (low-Z) to reduce the interaction of charged particle within the separator. Commercially available CF sheets are typically epoxy coated woven carbon fibers and are primarily made from low-Z material. Furthermore, the surface quality of the backbone defines the surface quality of the separator, hence a smooth CF surface is desired.

The dimensions of the CF sheets are governed by the size of segments and the requirement to have minimum dead volume. The diameter of PMTs define the cross-section of the segment which in turn defines the width of the optical separator to be 6.045”$\pm$0.015”. After accounting for the allowable tolerance in the width of CF sheets and the possible extra material from slitting, the CF sheets are defined to be 6.030”$\pm$0.015”. Maximum length of commercially available CF sheets with low variability in thickness is 48”. The manufacturing process of the CF sheets yields

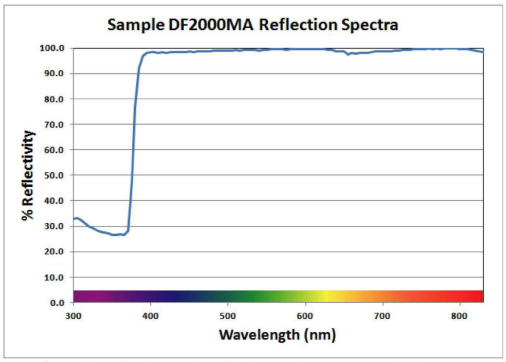

Figure 2. Typical Normal Angle Spectral Response DF2000MA

Figure 5.3. The normal reflectivity of DF2000MA in air as provided by the manufacturer 3M. The emission spectrum of the EJ-309 is in 400-500 nm range and DF2000MA has high reflectivity in this range.

slight bulge at the edges and the length of the CF sheets were thus limited to 47.5". The thickness of the CF sheet is a balance between rigidity and the dead volume. Additionally, a minimum amount of epoxy is needed to mask the texture of CF fibers and make the CF sheets smooth. Given these constrains, 0.023" thick epoxy-prepegged CF sheets commercially sold by ACP Composites, Inc [138][8] were chosen as the backbone.

DF2000MA, a specular reflective film manufactured by 3M acts as the primary photon reflector and is laminated on either sides of the CF sheets. The specular reflectivity in the visible region of wavelengths at normal angle of incidence as tested by the manufacturer is shown in Fig. 5.3. It is made of 100% polymer and is generally used in daylighting applications. DF2000MA is sold with protective liners on both adhesive and non-adhesive sides. Excluding the liners, the thickness of the film is 4.1 mil.

The specular and diffuse reflectivity of DF2000MA is shown in Fig. 5.4 in comparison with 3M ESR [139] as well as now discontinued 3M manufactured metal-

[8]A company out of Livermore, California specialized in design and fabrication of high-quality composite materials

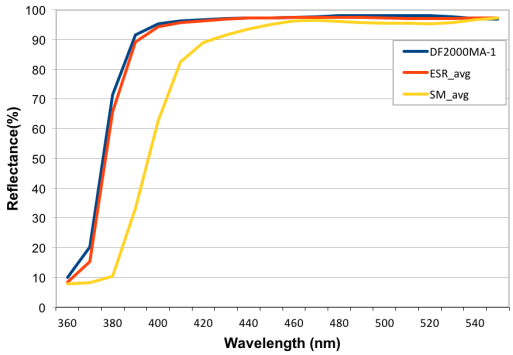

Figure 5.4. The normal reflectivity of the DF2000MA in the LiLS medium in comparison with the reflectivity of ESR and Solar Mirror 2020. ESR and DF2000MA have similar reflectivity within the uncertainties of measurements.

coated reflector called Solar Mirror 2020. DF2000MA exhibits similar optical properties as ESR which has been used in previous neutrino experiments [140,141] and widely used in several positron emission tomography applications [142,143]. DF2000MA has the advantage that it is sold with pressure sensitive adhesive mounted on one side which makes is easier to use for lamination applications. It is also sold in 50 yard long rolls and is relatively inexpensive per yard.

On either side of DF 2000-laminated CF sheets, an optically clear double-sided adhesive film, General Formulations Concept 106 [144] (henceforth referred to as the CON106) is laminated. CON106[9] is a combination of polyester film with optically clear acrylic adhesive mounted on both sides. The adhesive couples the reflector to FEP while maintaining uniform surface and optical quality of the separators.

0.002" FEP is laminated on top of the adhesive on either sides. FEP when thin is highly transparent which allows for the light to pass through it towards DF2000MA to be reflected back efficiently. Since the refractive index of FEP ($\sim$1.34) is lower than refractive index of LiLS ($\sim$1.57), the light traveling towards the separators at a

[9]These sheets are widely used to produce optically clear laminates in sign making industry.

Figure 5.5. Picture of a fully laminated optical separator.

Table 5.1. Nominal dimensions of the separator.

Constituent	Thickness(1/1000")
CF	23 $\pm$4
DF2000MA	4.1
CON106	2.7
FEP	40.6^{+3}_{-1}

grazing angle is total internally reflected back into the segment.

FEP is demonstrated to be one of the few materials that have shown long term chemical compatibility with LiLS. During FEP lamination, excess FEP was left extending beyond the edge of the separator on all four sides. The excess FEP around the edges were heat sealed to fully isolate the rest of the separator materials from the LiLS. After sealing all the four edges, the excess FEP past the heat seals was cut to yield the final optical separator as shown in the Fig. 5.5.

5.1.2 Design of Support Rods. Support rods provide the interface between the optical separators and two internal structural elements; the PMT housings and the acrylic wedges. Support rods also provide structure to the optical separators along the length of the segment helping maintain longitudinal uniformity. Additionally support rods provide access for the calibration sources to be deployed at several locations inside the detector.

Several techniques were investigated in producing support rods. The design of the support rods is defined by the interfacing components. The list of LiLS compatible material restricts the choice of usable materials for fabrication of the support rods. The following requirements were used as guidelines in the design of support rods in addition to the ones mentioned in Sec. 5.1.

- Uniformity along the length at over $\sim$1m
- Load bearing capabilities
- Ability to produce complicated structures

Fused Deposition Modeling (FDM) of Polylactic Acid (PLA) was chosen as the process for producing PROSPECT support rods. FDM is an additive manufacturing (3D printing) process where a desired thermoplastic filament is heated past it's

glass transition temperature and extruded though a nozzle onto a flat surface called a *bed*. Desired shapes can be generated by this process by translating the nozzle with respect to the bed during the process of printing. By stacking multiple layers of the filament, a 3D print of the desired dimensions is obtained. Salient features of FDM relevant to use in producing support rods are the following:

- **Complicated geometries:** FDM is ideal for generating long drawn out parts with consistent cross-section.
- **Rapid prototyping:** Since the startup costs and time for producing different designs are low, rapid prototyping is possible with FDM.
- **Wide availability of the commercial vendors:** There has been a recent proliferation of commercially available 3D printing services.
- **Parallel printing:** Several 3D printers can be used at the same time to produce identical components providing the ability to print several components in parallel.
- **Post-printing modification of parts:** PLA is soft material and can be easily machined. This provides the ability to modify printed parts.
- **Limitations on the length:** Commercial 3D printers are typically designed to produce parts $<$ 1m lengths. The support rods had to be designed to take this limitation into consideration.
- **Cost effective**

All the FDM printing for the PROSPECT support rods was done by Autotiv Inc [145][10]. Autotiv Mfg used multiple identical FDM printers for producing support

[10]A company based in Salem, New Hampshire specializing in additive manufacturing, CNC machining, casting, and molding applications

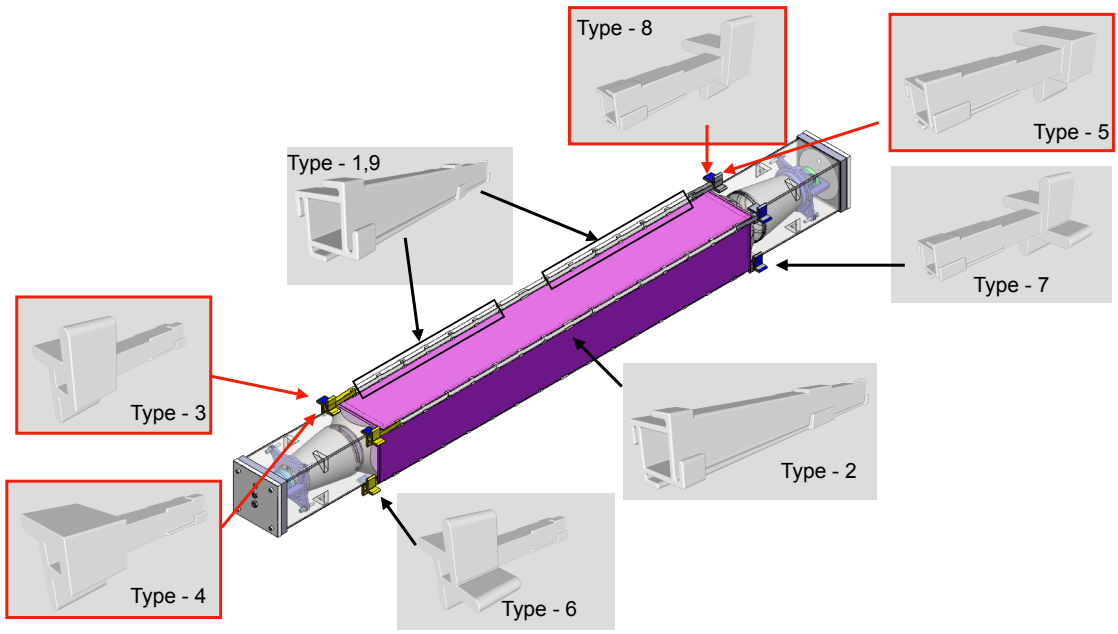

Figure 5.6. Support rod types shown by their longitudinal position along the segment. PMT-supporting rods highlighted in red boxes are located along the edge of the detector and hence have fewer than four arms.

rods for the PROSPECT detector. It was identified that with the desired printers any prints longer than 8" exhibited non-uniformity in the cross-section. To overcome the length restrictions of FDM process, 9 support rods were strung back-to-back to produce >1m long support rod assemblies. Keeping the rods at $\lesssim$ 8" allowed for maintaining the quality and precision of the prints.

The shapes and the sizes of the rods vary based on their location along their longitudinal position of the segment as well as their location in the detector. All support rods have tabs to clasp separators. Additionally, the rods that interface with housings or wedges also have thick arms in the interface to enforce the right amount of spacing. A total of 8 rod types were designed initially. Measurements have shown that the length of all the rods were consistently shorter than their nominal dimensions. Two rods in each strung assembly were printed slightly longer at a later date to fill the gap created by the shorter rods. As such a total of 9 rod types were

Table 5.2. Types of support rods and their dimensions.

Type	S.No.	Length (in)	Center Tab length(in)	End tab length(in)
Center	2	6.179	1.030	0.258
Standard	1		0.515	
Long	9	6.223		
PMT-supporting rods	3-8	3.75	N/A	0.515

produced and the details are shown in Tab. 5.2. Shown in Fig. 5.6 are the rod types, their cross-sections, and their locations in the detector.

5.2 Fabrication and QC/QA of the Optical Separators

The primary steps involved in the fabrication of the optical separators includes lamination and heat sealing. The PROSPECT detector requires an overall of 333 optical separators. To account for the failures and contingency, 388 CF sheets CNC machined to the proper size were ordered. DF2000MA, CON106, and FEP were sold as rolls and were cut to wider sizes prior to the procurement. DF2000MA and CON106 were cut to rolls of 7" wide to accommodate for potential lamination misalignment. FEP was acquired in 8" wide rolls to allow for ∼1" excess FEP on either edges for heat sealing.

DF2000MA was laminated on one side of cut-to-size CF sheets followed by CON106 lamination on the same side. The same steps were then carried out on the second side. After each of the above steps, the excess material extending past the edges was removed. The lamination process is finished with FEP lamination on both sides and the excess FEP was then heat sealed to produce a fully sealed sandwich. A schematic of the process is shown in the Fig. 5.7. All the lamination process was performed at Illinois Institute of Technology (IIT). The separators were then

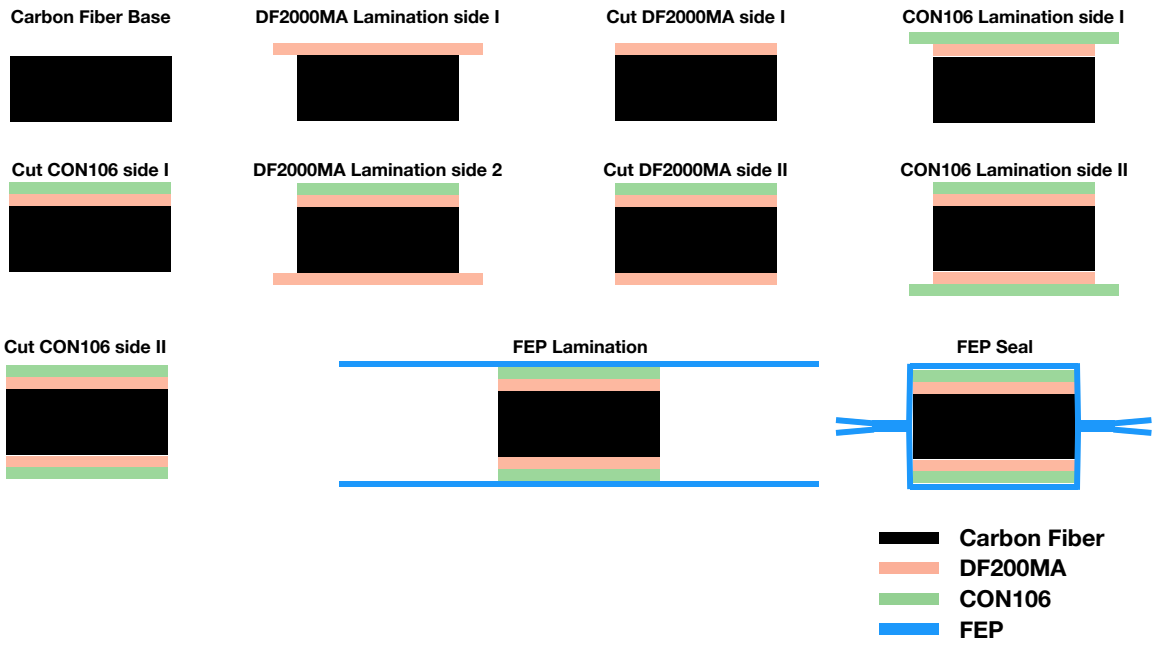

Figure 5.7. Step-by-step fabrication of the optical separators. The cross-sections are not to scale.

shipped to Ingeniven LLC [146][11] for heat sealing. In practice, the lamination is done in batches where a batch of separators go through each of the lamination steps shown in the Fig. 5.7.

Early prototypes showed that particulate matter embedded into the laminated layers has the potential to damage the FEP layers and consequently minimize the optical advantages of the separators. To reduce the damage to FEP, all the lamination was performed in a ISO class 7 soft-wall cleanroom. The cleanroom was wiped clean after each day of lamination. A household laser air quality monitor Dylos DC1100 [147] was used to monitor the particle count in the cleanroom.

The separator fabrication starts with cut-to-size CF sheets. The thickness of the CF sheets were recorded at 6 different locations along the edges and three different

[11]A company based in Hampton, New Hampshire specializing in production of high-performance teflon heat seals using an array of custom-built machinery

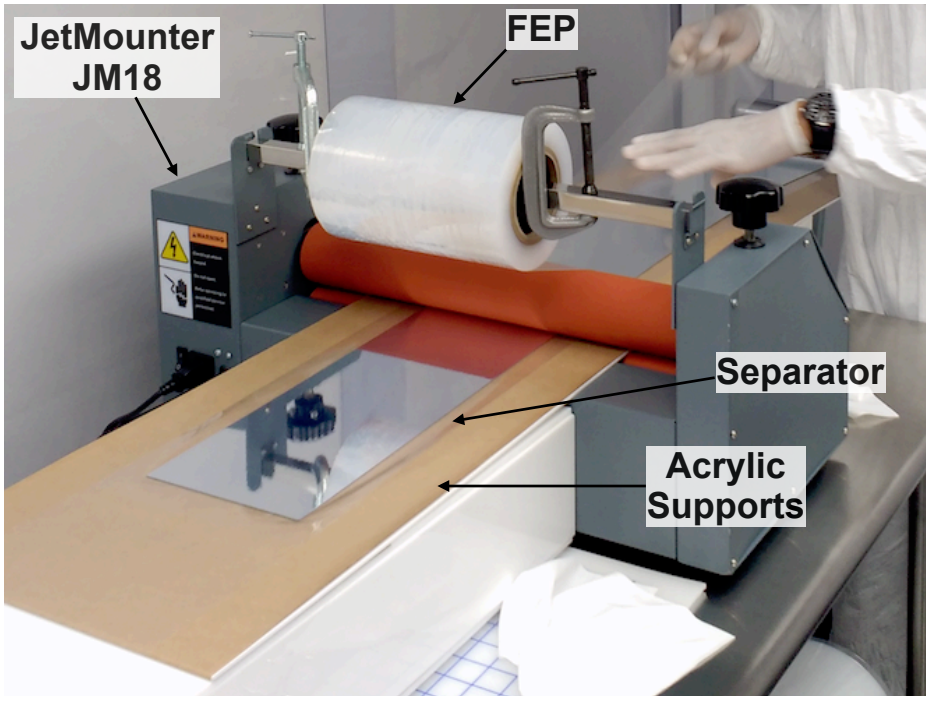

Figure 5.8. Lamination process showing FEP lamination on the separator.

locations at the center and are shown in the Tab. 5.1. CF sheets that exceeded 0.027" in thickness at the edges were rejected. Since they were CNC machined, no variations from the nominal value were found in the width of the bare CF sheets and consequently were not included as part of the QC measurements. The sheets that passed the thickness test were beveled along the edges using steel files to avoid rough surfaces that could potentially abrade FEP sheets. The corners of CF sheets were filleted to avoid them from potentially tearing into the FEP. The CF sheets were then cleaned twice with ethyl alcohol and once with water and transported into the cleanroom.

All the lamination was performed using JetMounter JM18 Cold Roll Laminator [148] as shown in the Fig. 5.8. Since cold roll lamination uses pressure for activating the adhesives, an optimum amount of pressure has to be applied during lamination. Too little pressure would not let the film properly adhere to the substrate and may lead to delamination, whereas too much pressure could force trapped air be-

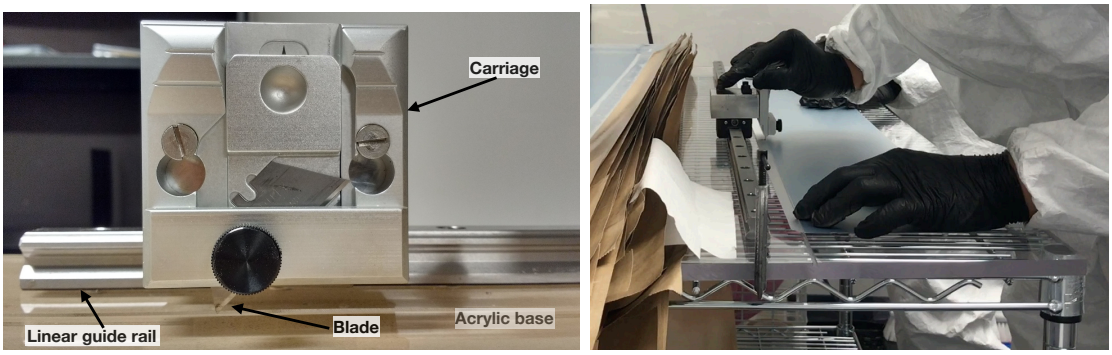

Figure 5.9. (left) Trimmer used for trimming excess material after lamination. (right) A picture showing trimming of excess DF2000MA.

tween layers and subsequently lead to blisters. The pressure was manually adjusted before each shift as well as every time the film was replaced. 1/4" thick × 18" wide × 58" long acrylic sheets were used as base to provide rigidity and enable relatively uniform application of pressure. Polyethylene coated paper was used on top of the acrylic sheets to prevent the adhesive from adhering to the base.

The trimming of extra DF2000MA and CON106 was performed using a custom-built trimmer for the long edges and by hand for the short edges. The trimmer is made from a 1/2" thick, 12" wide, and 54" long acrylic sheet base that has a steel linear guide rail affixed via CNC machined screw holes. A ball bearing carriage slides on the rail that has a blade affixed to it via a machined aluminum block. Precise placement of the separators on the acrylic sheet is achieved by aligning the separators to strategically placed steel dowel pins inserted into CNC machined holes in the acrylic sheet. Excess material was then trimmed by sliding the blade-affixed carriage along the rail as shown in Fig. 5.9.

Before FEP lamination, the width of the panels were measured at 3 different locations and recorded and checked for agreement with the nominal width shown in Tab. 5.1. The recorded widths are shown in the Fig. 5.10. The main purpose of this measurement was to make sure that the trimming of excess DF2000MA and CON106

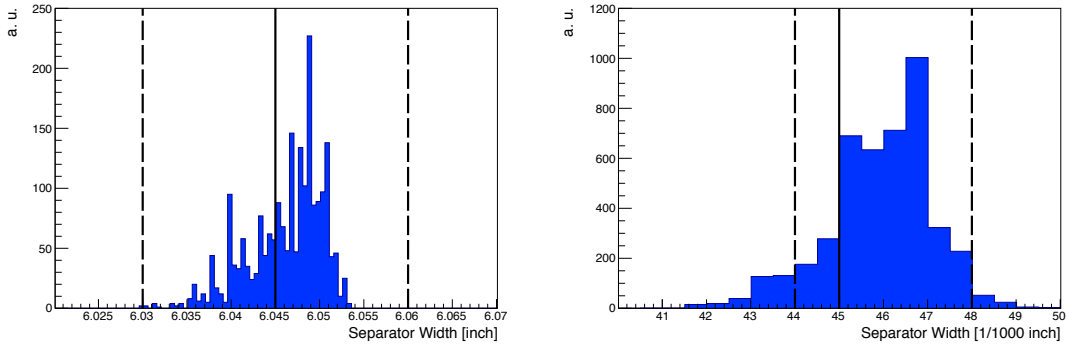

Figure 5.10. Separator width (left) and thickness (right) measurements performed before FEP lamination. Solid lines indicate the nominal width and the dashed line indicate the tolerance.

didn't leave any extra material adding undesired excess to the width of the separator. FEP lamination was the last step in the lamination process performed at IIT. Each separator was numbered after lamination by placing a label between the two layers of the FEP. Since FEP is prone to attract particulate matter, each separator was transferred into an ISO class 3 polyethylene cleanroom bag as soon as the lamination was performed.

After each batch of lamination was finished, the thickness of the separators and the reflectivity were measured. The thickness of the separator was measured at 12 different locations, 8 along the edge and 4 along the centers of the separator. Fig. 5.10 shows the measured edge thicknesses of the separators. The reflectivity of all the separators in 400-700 nm was measured and recorded at three different locations on either side of the separator. Ocean optics STS-VIS spectrometer reflectance was used to measure the total and specular reflectivity of all the separators. Consult Ref. [1] for a detailed assessment of the QC measurements performed on the separators. The separators were transferred back to the cleanroom bags and the bags were sealed to be packed for shipping.

Five 1/8" wide heat seals were performed on the separator. Four of the seals

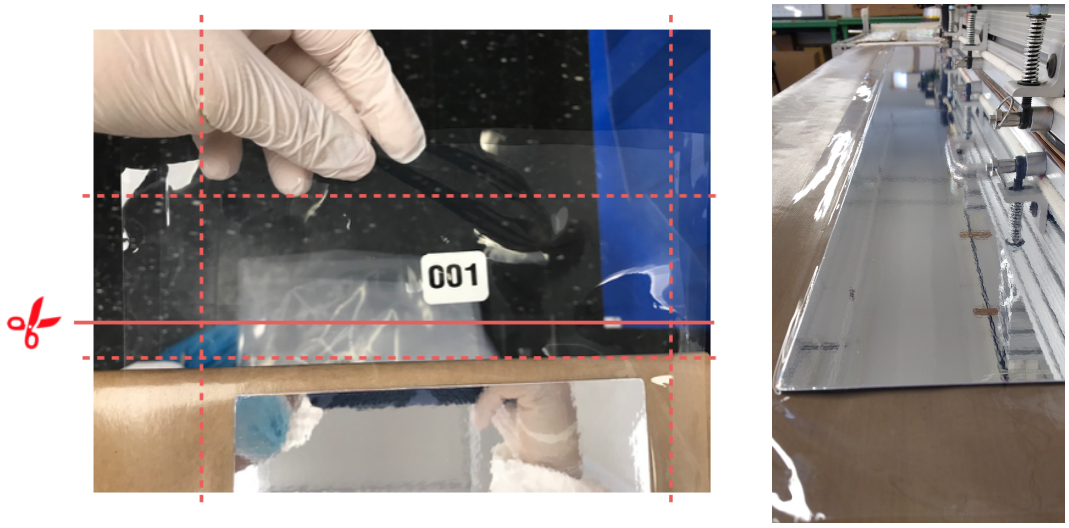

Figure 5.11. (left) Heat sealing scheme of the optical separator showing locations of four of the five heat seals (dashed line) and the trim line to remove extra FEP before assembly. (right) Heat sealing process with the heat sealing bar holding the FEP under pressure. A teflon coated sheet was placed under the separator to avoid scratches on the separator.

were performed 1/4" away from the edges of separators and an additional seal was performed on the shorter edge containing the label at ∼2" away from the edge to encompass the label as shown in the Fig. 5.11. Thermal impact heat sealing was employed for performing all the separator seals. This process utilizes a heating element that is heated and cooled under constant, uniform, and controlled pressure.

Two sealing machines, one for long and the other for short seals were used. ASTM F88 Peel Test [149] was performed using a Mark-10 force gauge. Two 1" wide sealed FEP samples, one for each machine were produced and subjected to increasing amount of tension as shown in Figure 5.12. Samples were deemed to pass the test if the seals did not peel before the load reached 3 lbs. Three peel tests equally spread out in time were performed each day. All samples successfully passed the peel tests indicating high fidelity of the heat sealers.

After heat sealing, all the seals were visually inspected for any imperfections. Any imperfections if found were salvaged by resealing if possible or were rejected

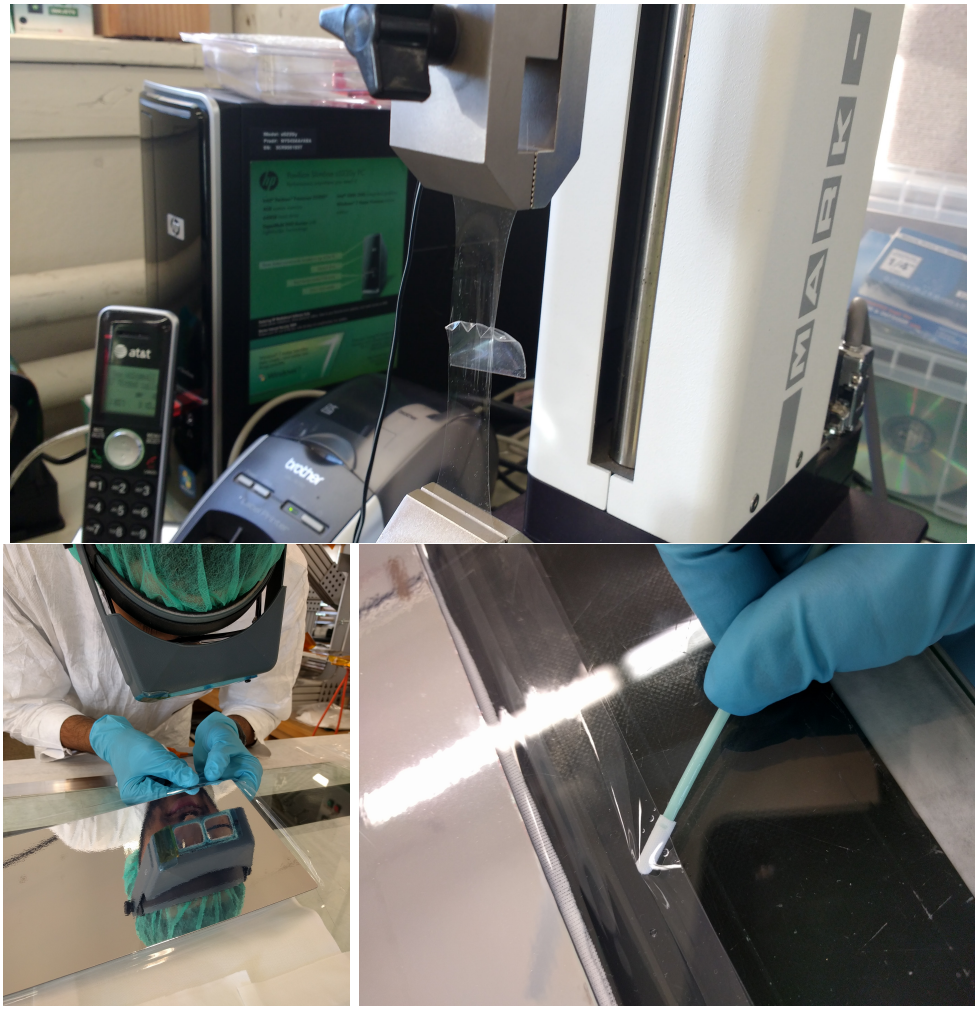

Figure 5.12. (top) Heat sealing QA showing the peel test using Mark-10 force gauge.Visual (bottom left) and probe (bottom right) tests performed on each individual separator.

otherwise. Ethyl alcohol was generously applied on the separator with an emphasis on edges and any noticeable imperfections. An ethyl alcohol-soaked polyester swab was used to probe between the films as shown the Fig. 5.12. Ethyl alcohol reacting with the adhesive in the separator was noticed to produce a milky white residue within $\sim$1 minute. Any separator displaying the white residue because of alcohol seeping into the separator was rejected. The extra FEP on all four sides were trimmed using an precision knife and all the leftover ethyl alcohol was wiped off the separator. The panels were bagged and shipped for cleaning and assembly to Yale university.

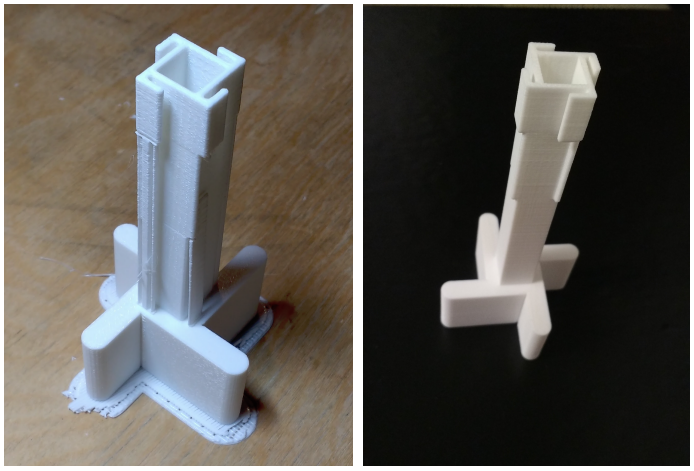

Figure 5.13. PMT-supporting rod immediately after printing (left) and after removing the extra support material and cleanup (right).

5.3 Fabrication and QC/QA of the Support Rods

For PROSPECT detector, a total of 1620 support rods were needed. After taking into account the spares, contingency, and rejects more than 2000 rods were printed. All the support rods were printed using 100 μm Hatchbox [150] white PLA filament with 100% infill. PLA was also used as the support material during printing. After printing, the support material and any undesired excess PLA was removed at Autotiv. Shown in the Fig. 5.13 is an example of 3D printed PMT-supporting rod before and after removing support material.

A thorough manual inspection and any possible rectification of all the rods was individually performed at IIT. An inherent characteristic of FDM based 3D printing is possibility of intermittent burrs on the printed surfaces. The burrs on the surfaces that would come into contact with separators were manually filed using stainless steel files. Occasionally, there is also a possibility of the small specks of burnt PLA getting deposited during the printing process leaving a dark brown blemish. The extruder was regularly checked and cleaned to reduce the incidence of burnt PLA. The support rods with burnt PLA that were not able to be filed off were rejected.

After filing, the smoothness of the insides of PLA tabs was tested by sliding a separator sample through each individual tabs of all the support rods. The rods were filed until they didn't leave any marks on the surface of the FEP of the separator sample. A 3/8" teflon tube was passed through each support rod and any rod that showed resistance was filed until the tube could pass through unobstructed. Lengths and tab dimensions of support rods were measured and recorded to 0.001" precision. The thickness of all the arms were measured for all the PMT-supporting rods and recorded. The center support rods that would consist optical calibration system were machined at Yale to create allowance for teflon diffusers.

5.4 Preparation and Assembly of the PROSPECT Optical Grid

The optical separators and the support rods were cleaned in an ISO class 3 cleanroom at Yale prior to the assembly. All the separators were cleaned with 1% Alconox solution and subsequently rinsed with deionized water until the conductivity of the rinse-off water was found to be below 0.1 μS/cm. The separators were then stored in cleanroom bags until assembly. The support rods were cleaned in an ultrasonic cleaner in 1% Alconox solution. They were rinsed with deionized water until the conductivity of the rinse-off water was found to be below 0.1 μS/cm and were left to be air-dried in the clean room at room temperature.

The support rods were pre-assembled ahead of the final detector assembly. In the PROSPECT detector, there are three different kinds of support rod assemblies based on the type of calibration sources used as shown in the Fig 4.10; no-source rod assemblies, optical calibration rod assemblies, and radioactive calibration rod assemblies. More details on the optical calibration assemblies and their assembly in the detector can be found in the Ref. [128]. The center support rods for the optical calibration rod assemblies were fit with the optical calibration system. Two long transparent acrylic rods with a rectangular cross-section and a groove for the teflon

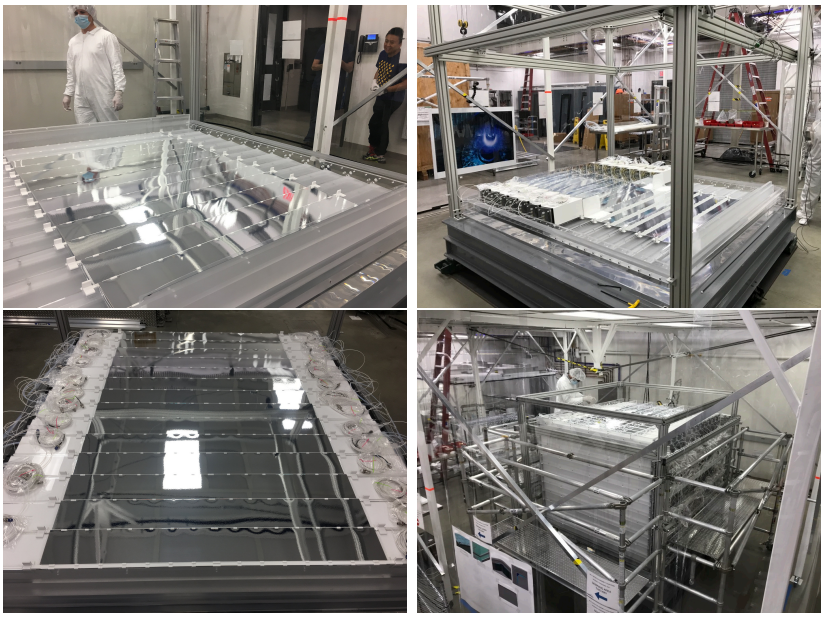

Figure 5.14. (top left) Assembled bottom most layer of separators. Partially finished (top right) and fully finished (bottom left) row of segments. (Bottom left) Fully assembled row (Bottom right) After complete assembly of the optical grid.

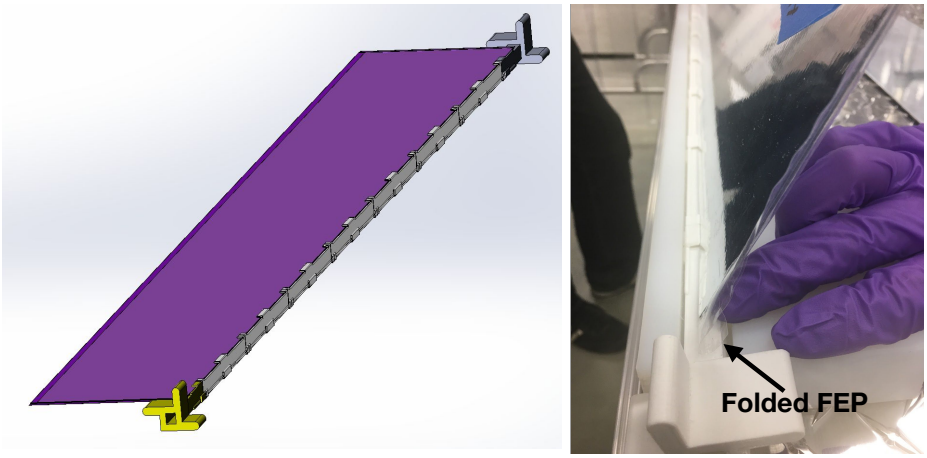

Figure 5.15. (Left) Schematic of the pre-inserted separator into the support rod assembly. (Right) A separator being inserted into the tabs of the support rod assembly.

tubes were used to help in the assembly of the rest of the support rods on the optical calibration rod assemblies. The support rods for the no-source rod assemblies were strung on long transparent acrylic rods. The radioactive calibration rod assemblies were similarly strung together on acrylic rods with the exception that these acrylic rods were replaced by 3/8" teflon tubes after the detector assembly. The support rod assemblies were then stored in long cleanroom bags awaiting assembly.

The assembly of the inner detector was performed in an ISO class 4 soft-wall cleanroom. The acrylic tank base was used as the starting point of the inner detector assembly by supporting it on strategically arranged polyethylene blocks which were placed on a steel base. The steel base has four vertical aluminum posts mounted on the four corners to perform layer-by-layer QA measurements. An adjustable stage having a movable bar is mounted on the vertical posts to allow for mounting of jigs and laser scanner for the QA measurements.

The inner detector installation started with the installation and centering of acrylic support wedges on the base. The bottom most layer of the horizontal optical separators pre-inserted into the support rod assemblies were then installed as shown in the Fig. 5.14. A jig was designed to pre-insert the optical separators into the tabs of the support rod assemblies prior to their assembly in the inner detector as shown in the Fig 5.15. The excess FEP on the long edges of the separators were folded during the insertion of the separator into the support rod tabs. PMT housings and the vertical optical separators were then installed alternatively until the complete row is assembled. Following the assembly of the next horizontal layer of the separators, a visual inspection followed by a survey of the layer is done using jigs and laser scanner at 7 locations along the segments. Based on the QA measurements, shims were added on top of the arms of the PMT-supporting rods to avoid buildup in height variations. The rest of the layers were assembled following the same procedure. A

detailed description of the the complete optical grid, and the assembly procedure can be found in the Ref. [1].

CHAPTER 6

CALIBRATION, RECONSTRUCTION, EVENT CLASSIFICATION AND PERFORMANCE OF THE PROSPECT DETECTOR

In the chapters 4 and 5, the experimental layout and the details of the PROSPECT detector were discussed. This chapter will discuss the details of calibrating the detector, reconstructing the physics quantities from raw data, and systematically classifying events into groups based on the reconstructed physics quantities.

6.1 PROSPECT Data Analysis Framework

Conversion from the raw waveforms to the physics quantities for PROSPECT is performed in multiple stages within PROSPECT2x_Analysis (P2x) [151], a data analysis framework designed for the PROSPECT experiment.

- **Raw data**

  Raw data recorded by the WFD modules as described in the Sec 4.2.6 are stored on disk in CAEN-proprietary file format. The raw data in binary format consists of the waveforms as well a header that includes start time of the file and the configuration settings of the digitizer. Each file typically has data from $\sim$16 PMTs collected over a duration of one hour.

- **unpacked data**

  At this stage the binary files from all the digitizers are unpacked and merged into ROOT [152] TTrees of waveform samples. The waveforms are time-ordered with the channel numbering from the digitizers converted to PMT positions in the detector. The global time information is stored as metadata to be added for each waveform later. No data analysis is performed at this stage. The unpacked data file stores the following key attributes for each sample:

  - Event number: Number assigned to the waveform by the P2x
  - Channel number: The position in the detector of the PMT that collected the waveform
  - Waveform number: Number of waveforms offset from the first waveform in the file
  - Waveform: An array containing the digitized waveform

- **DetPulse data**

  The digitized waveforms are examined and the important components of the waveforms are extracted from the unpacked files and stored in the DetPulse files. All the quantities remain uncalibrated at this stage. The DetPulse data file stores DetPulse objects, the key attributes of which are the following:

  - Event number: Reproduced from the Event number from the unpacked data
  - PMT number: Reproduced from the Channel number from the unpacked data
  - Arrival time: Pulse arrival time at the PMT
  - Waveform integral (s): Area of the pulse in analog-to-digital convertor (ADC) units
  - PSD: Pulse shape discrimination parameter

- **PhysPulse data**

  Calibrations are applied to the DetPulse data and the physics quantities are extracted at this stage and stored in PhysPulse format. The physics quantities are extracted by combining DetPulses from both the PMTs in the segment corresponding to the pulse. The key attributes of the PhysPulse objects are the following:

- Event number: Event number from the DetPulse data
- Segment number: The position in the detector of the segment where the sample was collected
- Event time: Time from the start of the run
- Differential time *(dt)*: Difference in the time of arrival of the pulses to the PMTs in the segment
- Longitudinal position of the pulse *(z)*: Reconstructed position of the pulse along the length of the segment
- Energy(E_{rec}): Reconstructed energy in electron equivalent energy
- PSD: PSD obtained from the combination of PSDs of both the DetPulses
- PID: Particle ID based on the Energy and PSD information

It is to be noted that the above data objects have more attributes but are not discussed here since they weren't used in this analysis.

The energy deposits of interest typically cover more than one segment. For full event reconstruction, a transient data structure called *PhysCluster* is used by grouping together pulses where each pulse is separated by the next one by no more than 20 ns. The energy of each cluster (E_{rec}) is the sum of calibrated energies of the pulses in the cluster; and the longitudinal position (Z_{rec}) of the cluster is the reconstructed position of the highest energy pulse in the cluster. Most classes of events of interest including IBDs are tagged by coincidence. For coincidence analysis, another transient data structure called *PhysClustersWindow* is used which groups clusters if they occur within a defined characteristic time of each other. The characteristic time varies based on the event class being tagged.

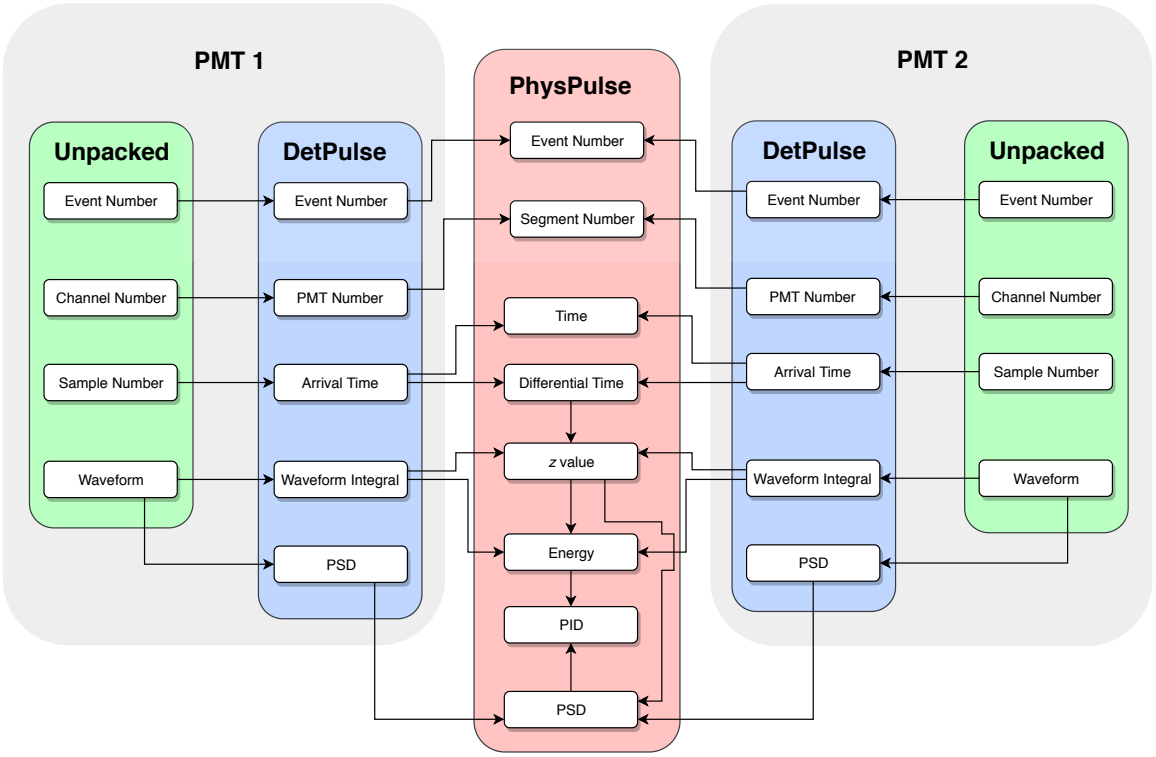

Figure 6.1. Relation between analysis data structures showing associations between various attributes. DetPulses are uncalibrated data objects that are extracted from unpacked data. PhysPulses contains physics quantities that are extracted from a combination of DetPulses corresponding to both PMTs in a segment.

6.2 Detector Calibration

The primary quantities used in the sterile neutrino search through neutrino oscillations are the energy and position of the IBD-induced positrons. The other physics quantities of interest that are used for the event selection are PSD, timing, and position of the prompt and delayed events. All these quantities are built from the raw data collected in form of PMT waveforms and recorded by the digitizers. The response of the detector is position and energy dependent and accordingly segment- , z-, and energy-dependent calibrations were applied in generating these physics quantities.

6.2.1 Muon-based Calibration. Being a surface detector, there is an abundance

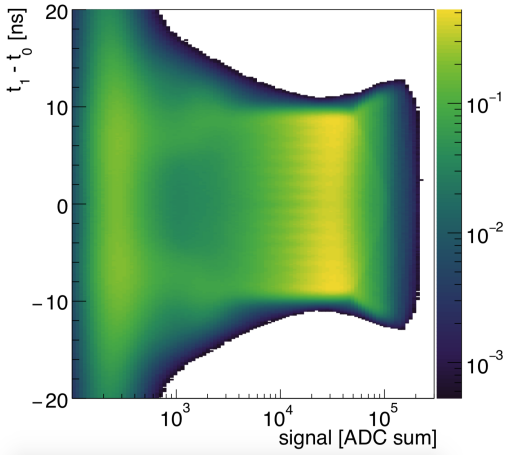

Figure 6.2. The selection of down going muons as a function of the ADC integral sum and the arrival time difference between the DetPulses from the PMTs in the segment.

of muons constantly traveling through the PROSPECT detector. The distinct design of the detector gives an ability to take advantage of muons and use them as a source for calibration. For this analysis, DetPulses corresponding to down going tracks with small transverse spread were selected with the requirements that they span at least four segments with $\sum_i s_i > 10^5$ and $4 \times 10^3 < \sqrt{s_a s_b} < 5 \times 10^4$, where i spans over all PMTs that register energy of the track and a, b are PMTs from the same segment. The specific choice of the geometric mean of the waveform integrals in a segment for

muons requires them to travel less than the full width of the segment and are hence called *corner-clipping* muons.

6.2.2 Timing Calibration. The corner-clipping muons described above provide coincident DetPulses between PMTs within a segment as well as the other segments in which they deposit the energy. The timing differences between all the PMTs in the detector were calibrated by using the arrival time of the coincident corner-clipping muon DetPulses and taking the muon transit time into account. Following this procedure, an average precision in timing of 0.1 ns between the segments and 0.2 ns within the segments were found.

6.2.3 Position Calibration. The reflectivity of the PLA in the support rods is different from the reflectivity of the optical separators and consequently the corner-clipping muons depositing energy closer to the support rod tabs have slightly modified light transportation. Since the locations of the support rod tabs are well known, the timing difference dt between the PMTs in a segment for the corner-clipping muons can be used to calibrate z position along the segment. Shown in the Fig 6.2 are the rates of the corner-clipping muon events as a function of the timing and the sum of ADC integral (s_1+s_2). Shown in Fig 6.3 is a small subset of the selection used for muon-based position calibration. The functional form of the relation between differential timing and the z-position agrees well with the known positions of the radioactive source deployments as shown in the Fig 6.3.

6.2.4 Energy Calibration. The background neutron captures on ^{6}Li (nLi) described in 4.2.5.4 plays an important role in energy calibration of the detector. To set the energy scale, ADC-to-MeV values for each segment were defined such that the nLi peak from a subset of PhysPulses in the center of the segment results in a

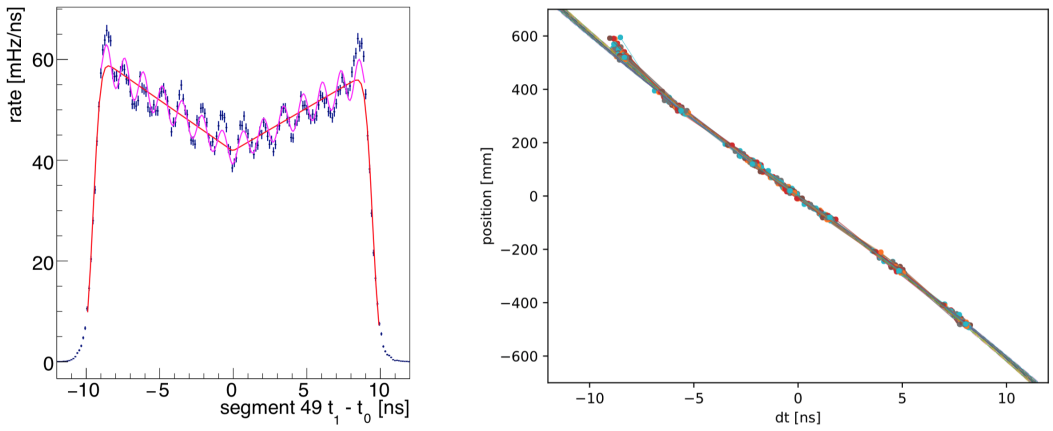

Figure 6.3. (left) A narrow band ($1 \times 10^4 < s_a + s_b < 2 \times 10^4$) of the corner clipping muon event selection for one particular segment and the fit performed on it. (right) $z(dt)$ extracted from down going muons compared to the known z from the source calibrations.

constant value 0.54 MeVee[12], similar to the value obtained with the PROSPECT-50 detector. By fixing the nLi peak at a well-defined value, all the segments were constrained to have the same absolute energy scale independent of the differences in electronic and scintillator responses. Additionally, z-dependent corrections extracted from a combination of the ratio and geometric mean of s_i for both PMTs in each segment were applied independently to each PMT. Shown in the Figs. 6.4, 6.5 are the ratio and geometric mean of s_i and the light curves for all the segments in the detector . Radioactive calibration sources in addition to the intrinsic and background sources as discussed in the Sec 4.2.5 were used to then set the absolute energy for the full detector. The radioactive calibration sources used for this analysis are shown in the Tab. 6.1.

[12]Because of quenching in liquid scintillator, all the energy deposited in the scintillator is not converted into photons. This process called quenching is higher for heavier particles. The quenched energy is described in electron-equivalent energy ($MeVee$). is used to describe the quenched energy.

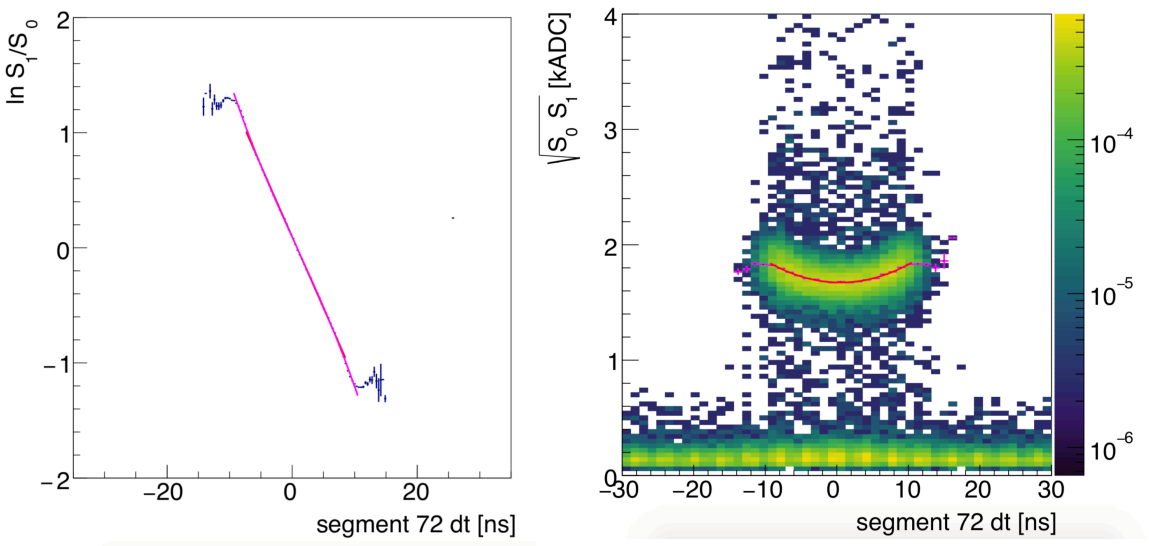

Figure 6.4. Ratio (left) and geometric mean (right) of the waveform integrals measured by both PMTs for a single segment. The ratios were fit to cubic polynomials (magenta) and the geometric means were fit to a quadratic polynomials (red). The functional form obtained from these fits were used to make z-dependent corrections to the energy.

Table 6.1. Radioactive calibration sources used for calibration in this analysis. ^{252}Cf and AmBe sources were later deployed in the detector and used for later analyses.

Source	Primary decay type	Calibration type	Energy[MeV]
^{137}Cs	β^-	γ	0.662
^{60}Co	β^-	$\gamma+\gamma$	1.333+1.173
^{22}Na	β^+	$\gamma+\beta^+$	1.274+2×0.511

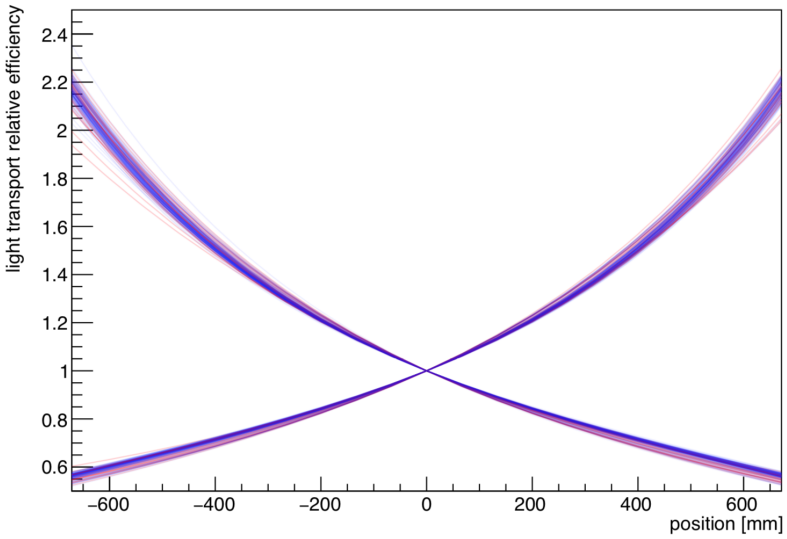

Figure 6.5. The light curves used to correct for the z-dependence of the energy. Curves in blue are for the Hamamatsu PMTs and in pink are for the ET PMTs.

6.2.5 PSD Calibration. Due to the chemistry of liquid scintillators, scintillation light has two components; short lived (fast component) and long lived (slow component). The ratio of amount of light emitted as the fast component to that emitted as the slow component is dictated by the type of interaction. Nuclear recoils with higher energy deposition density emit light with significantly more slow component compared to electronic recoils. The shape of pulse can then be used to distinguish nuclear recoils from electronic recoils.

PSD parameter used for this analysis is defined as the ratio of the integral of the tail of a pulse to its total integral as shown in Fig 6.6. Because of the elongated nature of the segments, the arrival time for the pulses get broader with distance from the event to the PMTs. The PSD dependence of corner-clipping muons on the longitudinal position is used for each segment to correct for the z-dependence of PSD for all the pulses at the DetPulse level. PSD for the backgrounds after the calibration is shown in Fig. 6.7.

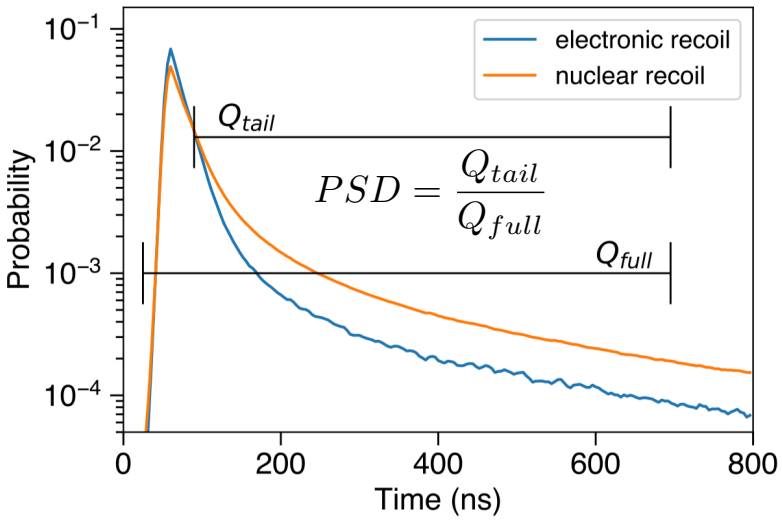

Figure 6.6. Probability distribution of waveforms showing a clear distinction between the waveform shapes of electronic recoils and nuclear recoils. Shown are also the ranges used to define the PSD parameter.

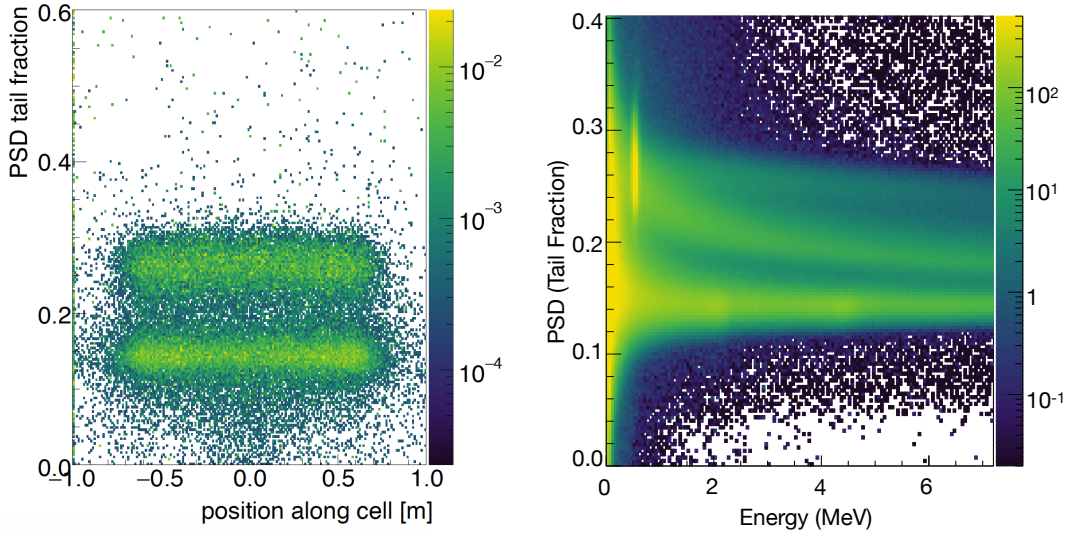

Figure 6.7. Post-calibration PSD of background PhysPulses. (left) PSD as a function of longitudinal position. Two distinct bands corresponding to electronic/neutron (bottom/top)-like recoils could be seen. No noticeable z-dependence can be seen for either of the bands. (right) PSD as a function of Energy. The energy dependence of both electron- and neutron-like PSD can be noticed.

6.3 Event Classification

In this section the classification of events at the PhysCluster level are discussed for signal, backgrounds, and the classes of events used for tracking the detector performance. Most of the event classes are tagged by using delayed coincidence between PhysClusters belonging to a particular class (defined by PSD) and placing a constraint on the relative position between them. The selection criteria for various PROSPECT coincident event types are shown in Tab. 6.2.

6.3.1 Signal. The signals in PROSPECT experiment are IBDs initiated by neutrinos originating from the reactor. With the lessons learned from the PROSPECT prototypes and guidance from the commissioning data of the detector, an initial set of analysis cuts were defined for the selection of IBD events. A combination of two PhysClusters is defined as an IBD candidate if a low PSD prompt cluster (positron) in time- and position-coincidence with a high PSD delayed cluster (nLi) with appropriate capture energy. Additionally, cosmogenic backgrounds are reduced by requiring no occurrence of muon-like or fast neutron-like events close to the delayed cluster. Following are the analysis cuts used to classify IBD candidates:

- Prompt PSD: Any cluster with PSD of all pulses in the clusters falling within 3σ of the mean of the gamma-like PSD band. As shown in the Fig. 6.7 PSD is energy dependent, hence the PSD selection is also chosen to be energy-dependent.
- Prompt Energy of PhysCluster: N/A (No analysis cut was placed at this stage but only 0.8-7.2 MeV range was considered for the sterile neutrino search.)
- Delayed PSD: Any single-pulse cluster with PSD of the pulse falling at least 3.6σ away from the mean of the gamma-like PSD band and below 0.4. The mean of the gamma-like PSD band is extracted on regular basis from distributions similar to the one showed in the Fig. 6.7.

- Delayed Energy of PhysCluster: 0.46-0.60 MeV
- Time correlation: The delayed PSD has to occur (+1,+120) μs after the prompt event.
- Position correlation: Prompt and delayed clusters have to happen within 180 (140) mm along z for the same (adjacent) segments.
- Shower veto: Neutron capture events occurring within +100 μs of muon events defined by E_{rec} >15 MeV are vetoed. Similarly neutron capture events occurring within $\pm$200 μs of other nLi and recoil events with PSD> $3\sigma_\gamma$ are rejected.
- Fiducialization: Both prompt and delayed events cannot occur in the segments on the edge and within one segment wide away from the edge along z.

6.3.2 Backgrounds. Background mimicking IBD events can be classified into correlated and accidentals. Correlated IBD-like events in the PROSPECT detector arise primarily from cosmogenics [125].

6.3.2.1 Cosmogenics. A significant number of cosmogenic backgrounds arise from fast neutrons. Multiple neutrons could originate from the same primary source and produce two PhysClusters close in time with PSD signatures similar to the IBD events. One such event class is when one neutron captures on hydrogen and produce a 2.2 MeV γ followed by another neutron capturing on ^{6}Li.

$$\begin{aligned} n +^1 \mathrm{H} &\rightarrow^2 \mathrm{H} \\ n + {}^6\mathrm{Li} &\rightarrow \alpha +^3 \mathrm{H} \end{aligned} \tag{6.1}$$

Another predominant source of backgrounds is when a fast neutron inelastically scatters off of a Carbon atom forcing it into a metastable state which then retreats to its ground state releasing a 4.4 MeV γ. The neutron then captures on

Table 6.2. Selection cuts for various coincidence event classes used for this analysis. Shower veto cuts and fiducial cuts are not shown in the table. For IBD accidentals identical cuts as the ones used for the IBD selection were used with the exception that Δt is (-12,-2) ms. For PSD $n\overline{\sigma_\gamma}$ corresponds to the n sigma away from the PSD mean of the γ band.

Event \ Cut		E_{rec} (MeV)	PSD	Δt (μs)	Δz (mm)
IBD	Prompt	N/A	$< \lvert 3\overline{\sigma_\gamma}\rvert$	(1,120)	180 (140)
	Delayed	(0.46,0.60)	$> 3.6\overline{\sigma_\gamma}, < 0.4$		
^{12}B	Prompt	(0.7,10.0)	$> 3.6\overline{\sigma_\gamma}, < 0.4$	(1×10^3,30×10^3)	40
	Delayed	(0,20)	$< \lvert 3\overline{\sigma_\gamma}\rvert$		
^{212}BiPo	Prompt	$\leq$4.0	(0,0.26)	(0.2,6)	200
	Delayed	(0.97,1.26)	(0.18,0.34)		
^{214}BiPo	Prompt	$\leq$4.0	(0,0.26)	(10,711)	200
	Delayed	(0.75,1.00)	(0.18,0.34)		
RnPo	Prompt	(0.57,1.15)	(0.19,0.36)	$< 12.85 \times 10^3$	200
	Delayed	(0.57,1.15)	(0.19,0.36)		

^{6}Li generating a delayed capture signal.

$$\begin{aligned} n +^{12}\mathrm{C} &\rightarrow^{12}\mathrm{C}^{*} + n' \\ ^{12}\mathrm{C}^{*} &\rightarrow^{12}\mathrm{C} + \gamma \\ n + ^{6}\mathrm{Li} &\rightarrow \alpha +^{3}\mathrm{H} \end{aligned} \tag{6.2}$$

Since all the reactor-related correlated IBD-like backgrounds are effectively shielded by the passive shielding, all the correlated backgrounds are from cosmogenic neutrons and muons. This cosmogenic contribution was then used to subtract the correlated backgrounds from the IBD candidate dataset.

6.3.2.2 Accidentals. Accidentals are defined as a pair of uncorrelated signals resembling an IBD event as defined in 6.3.1 in the detector. Accidentals are significantly higher during the reactor on period because of the high rates of singles from the reactor. Since cosmogenic-induced events in the PROSPECT detector have lower single rates and are efficiently reduced by veto, PSD, and timing analysis cuts and their rates are smaller than the reactor-related background, their contribution to the accidental rates are minimal. This can be seen in the Fig. 6.13. Reactor-related singles vary significantly within the detector depending on the gamma activation within the reactor facility and the structure of the passive shielding. Since the main source of accidental are from the reactor-related gamma-like singles, the accidental rates are also position dependent.

The accidental contribution to the IBD candidate dataset was estimated by searching for a prompt PhysCluster followed by an nLi PhysCluster within a time window of (-12,-2) ms. The rest of analysis cuts were identical to signal selection cuts. By searching for the pairs of PhysClusters reversed in time compared to the IBD events and extending the closest time separation to 2 ms, it was ensured that there is no correlation between the PhysClusters. The accidental dataset time separation

was chosen to span a wide range of 10 ms to minimize the statistical uncertainty.

6.3.3 Event Classes for Tracking Detector Response and Performance. PROSPECT utilizes various intrinsic sources and backgrounds that are distributed throughout the detector to track the response of the detector. These event classes do not mimic the signal events and hence do not play a role in IBD selection.

6.3.3.1 ^{12}B. As described in the Sec 4.2.5.4, cosmogenically produced ^{12}B could be used to validate the detector performance. ^{12}B provides β spectrum spanning energies up to its endpoint at 13.37 MeV and provides the ability to benchmark energy response over full range of neutrino spectrum. Cosmogenic neutrons undergo ^{12}C(n, p)^{12}B and the resultant ^{12}B beta decays producing βs with a lifetime of 29.14 ms.

^{12}B events were selected by searching for nuclear recoil PhysClusters depositing energy in (0.7, 10) MeV within one segment followed by an electronic recoil (PSD-based) PhysCluster with a Δt =(3,30) ms depositing less than 20 MeV within a maximum of 3 segments. Accidentals were removed by selecting PhysClusters using the same analysis cuts with the exception of Δt =(-199, -5) ms.

6.3.3.2 BiPo. The decays of ^{212}Bi and ^{214}Bi both produce a β followed by an α. The chain for these decays include

$$\begin{aligned} ^{212}\text{Bi} &\rightarrow ^{212}\text{ Po} + \beta \\ ^{212}\text{Po} &\rightarrow ^{208}\text{ Pb} + \alpha, \end{aligned} \tag{6.3}$$

$$\begin{aligned} ^{214}\text{Bi} &\rightarrow ^{214}\text{ Po} + \beta \\ ^{214}\text{Po} &\rightarrow ^{210}\text{ Pb} + \alpha. \end{aligned} \tag{6.4}$$

With lifetimes of 299 ns (0.1643 ms) for ^{212}Po (^{214}Po). The β decay end point of ^{212}Bi(^{214}Bi) is 2.252 (3.275) MeV and quenched α energy of ^{208}Pb(^{208}Pb)

decay is ∼1.1 (0.9) MeV. Although topology and PSD signatures are similar to IBDs, the quenched energies of the delayed α events are higher than neutron captures and hence cannot be mistaken for IBD events. A delayed coincidence of electron recoil PhysClusters with 0<PSD<0.26 and $E_{rec} \leq 4$ MeV followed by nuclear recoils with 0.18<PSD<0.34 and 0.97 (0.75) MeV<$E_{212\ (214)}$ <1.26 (1.00) MeV within a time window of 0.2 (10)μs < $\Delta t_{212\ (214)} < 6$ μs (0.69 ms) and a distance $\Delta z \leq 200$ mm was used to select BiPo events as described in Tab.6.2.

6.3.3.3 RnPo. Actinium is an intrinsic source that was deliberately doped into the PROSPECT LiLS before detector filling as described in Eq. 4.2.5.3. ^{227}Ac is part of the decay chain of ^{235}U which produces two successive αs

$$\begin{aligned} {}^{219}\mathrm{Rn} &\rightarrow {}^{215}\mathrm{Po} + \alpha \\ {}^{215}\mathrm{Po} &\rightarrow {}^{211}\mathrm{Pb} + \alpha. \end{aligned} \tag{6.5}$$

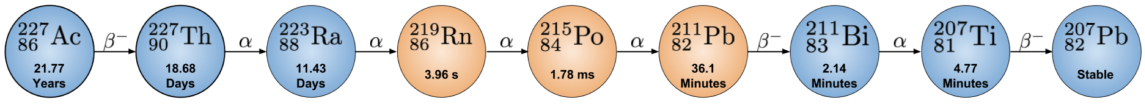

Figure 6.8. ^{227}Ac decay chain showing ^{219}Rn and ^{215}Po decays. Coincidence rate measurement of α from the decay of ^{219}Rn followed by another α from the decay of ^{215}Po in each segment provides a proxy for the volume of the segment. With a lifetime of ∼21 years, ^{227}Ac lasts longer than PROSPECT experiment runtime.

These α, α coincidences (RnPo)events are separated by a half-life of 1.78 ms as shown in the Fig. 6.8. The quenched energies and PSDs of RnPo events are outside the IBD selection windows and therefore are not a source of backgrounds. A delayed coincidence of nuclear recoils with 0.19<PSD<0.36 and 0.57 MeV<E<1.15 MeV followed by another nuclear recoils with 0.19<PSD<0.36 and 0.66 MeV<E<1.15 MeV within a time difference of Δt <12.85 ms and position difference of Δz <200 mm was used to select RnPo events as described in Tab.6.2. Both RnPo and BiPo events

being distributed throughout the detector were used to track the energy, position, and PSD uniformity and stability over time.

6.4 Performance of the Detector

The performance of the detector as a function of segment and time was gauged using reconstructed physics quantities for various event types: radioactive calibration sources as shown in the Tab. 6.1 for uniformity of E_{rec}, energy resolution (σ_E), and z_{rec}, BiPos for stability and uniformity of σ_z and E_{rec} and uniformity of σ_E, RnPos for uniformity of E_{rec}, σ_z, and σ_E and uniformity of event rate (proxy for size of the segment), and nLi for the stability of E_{rec} and σ_z.

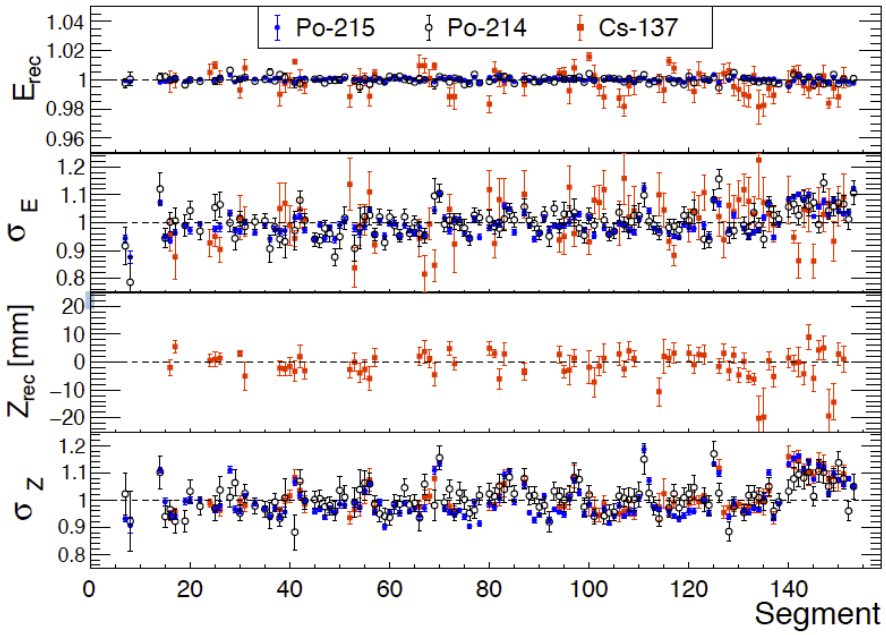

Figure 6.9. (From top to bottom) Uniformity of the reconstructed energy, energy resolution, longitudinal position and its resolution within the detector. Only ^{137}Cs was used for longitudinal position reconstruction because all the other sources are distributed throughout the detector. The gaps in ^{137}Cs shows the segments that did not have a calibration tube with a dedicated ^{137}Cs run. Error bars in all cases represent statistical uncertainties only.

Fig. 6.9 shows the uniformity of these reconstructed quantities within the detector. The reconstructed energy (resolution) is within ~1%(10%) and the recon-

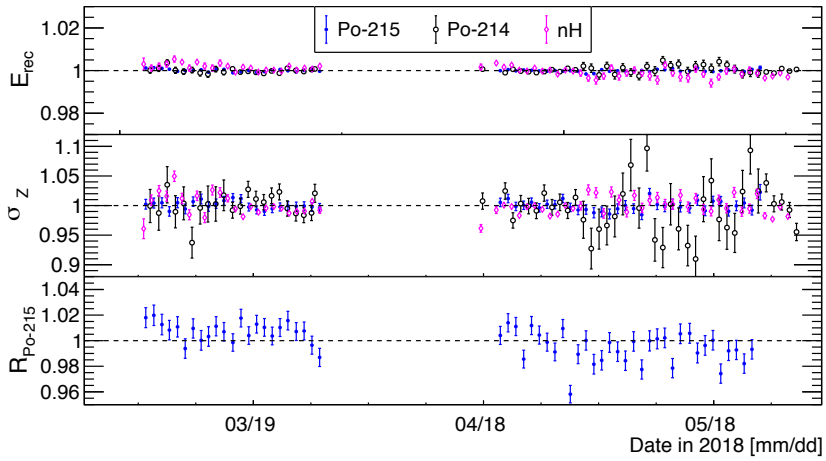

Figure 6.10. (From top to bottom) Stability of the reconstructed energy, position resolution, and RnPo rates with time. Empty periods at the end of March 2018 shows the calibration and maintenance periods. Error bars in all cases represent statistical uncertainties only

structed longitudinal position (resolution) is within ∼10mm(10%) for all the sources. Fig. 6.10 shows the stability of the reconstructed quantities with time. The reconstructed energy is within ∼0.5% and the reconstructed longitudinal position resolution is within ∼10% over ∼2 months. Additionally, the measured RnPo rates were found to be within ∼2%.

6.5 Validation of PROSPECT Monte Carlo Simulations

PROSPECT detector is small (similar in size to the attenuation length of light EJ-309) and has a complicated geometry and the response of the detector is highly position- and energy-dependent. Since PROSPECT searches for $\overline{\nu}_e$ oscillations by performing a position-dependent spectral comparison, it is important to generate an accurate position-dependent detector response. Monte Carlo (MC) simulations using PROSPECT-G4 (PG4) [13] was used to generate the detector response. In addition to

[13]A Geant4-based [153] MC simulation package for the PROSPECT detectors [154]

generating position-dependent energy response, PG4 was used to quantify systematic uncertainties in energy response and examine and alter the absolute energy scale.

To validate MC simulations in PG4, data from the calibration sources ^{137}Cs, ^{60}Co, and ^{22}Na as shown in the Tab. 6.1 and ambient source ^{12}B described in the Sec. 6.3.3.1 were compared to the respective MC simulations generated using PG4. Four parameters were used to tune MC simultaneously of all the sources and fit to the data. Best fit parameters from this fit were then used to fix the response generated from PG4 simulations. Two of the four parameters correspond to quenching effect of the LS. An empirical equation due to Birks [155] was used to model the light yield per track length

$$\frac{dL}{dx} = \frac{\frac{dE}{dx}}{1 + k_B \frac{dE}{dx}}, \tag{6.6}$$

where dL and dE are the differential light yield and energy loss per track length dx; k_B is Birk's constant with units mm/MeV that is empirically extracted from the the fit. The modeling was done at PG4 step level which is the smallest element of PG4 simulation where the energy loss is simulated.

In addition to producing scintillation light by electromagnetic interactions, charged particles traveling at speeds past the Cherenkov threshold could also deposit a small amount of energy via Cherenkov radiation. Optical photon transport simulations are extremely processor intensive and PG4 was not optimized for optical simulations. Therefore to include the Cherenkov contribution, an ad-hoc component based on the Ref. [156] was added in PG4 simulations at the step level using

$$\frac{d^2N}{dxd\lambda} = k_C \frac{2\pi\alpha z^2}{\lambda}(1 - \frac{1}{\beta^2 n^2(\lambda)}). \tag{6.7}$$

This equation gives the number (N) of Cherenkov photons generated per track length (x) of a given wavelength (λ) for a particle with charge z traveling at a speed β through a material of refractive index $n(\lambda)$. In adding Cherenkov contribution, the refractive index was assumed to be identical for all the wavelengths. α is the

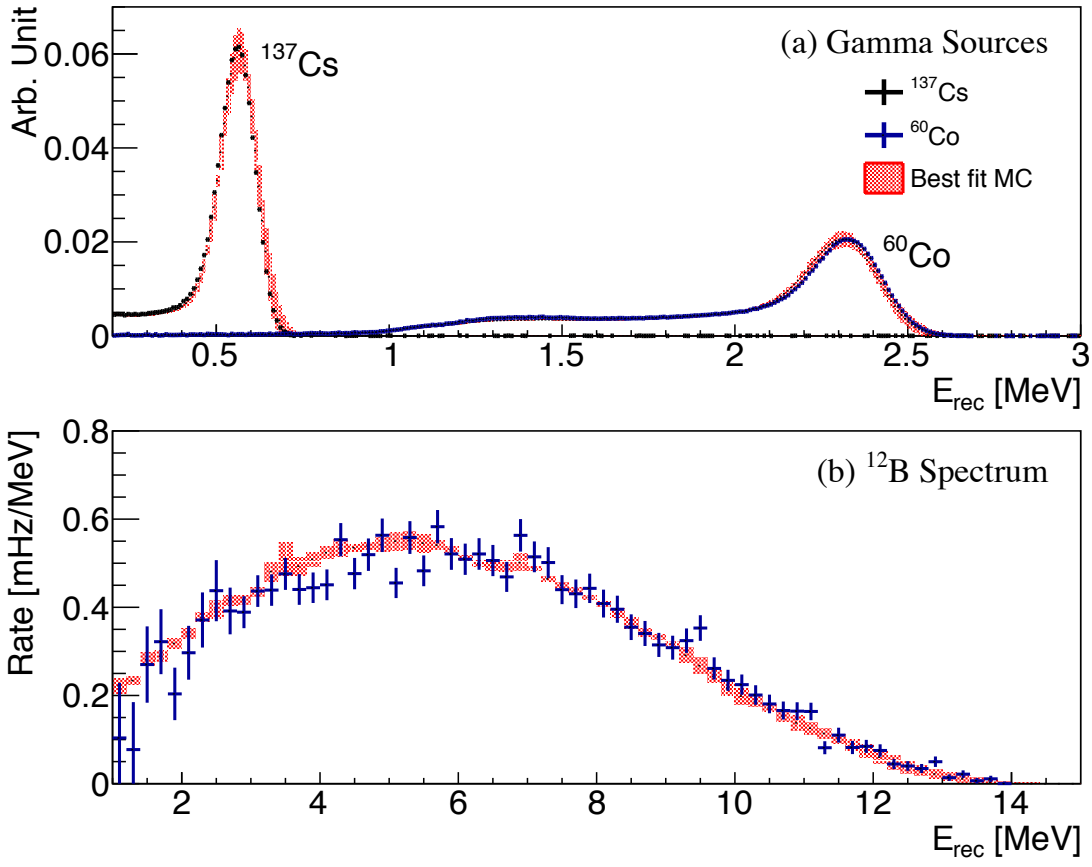

Figure 6.11. (a) Comparison of measured ^{137}Cs and ^{60}Co γ spectra to the respective MC-generated spectra using the best-fit parameters. (b) Measured ambient ^{12}B spectra comparison with MC-generated ^{12}B spectrum. Blue error bars are statistical errors and red bands were generated from uncertainty in the best-fit energy model parameters. Good agreement can be seen between data and MC.

fine structure constant and k_C is the tunable parameter that defines the fraction of emitted Cherenkov light detected.

PROSPECT energy resolution effects are dominated by photostatistics. Energy-dependent smearing was applied to the reconstructed energy spectrum during the P2x data analysis stage[14] using the function

$$\frac{\sigma}{E} = \frac{b}{\sqrt{E}}, \tag{6.8}$$

where b is the tunable parameter.

Finally, absolute energy scale β_{rec} is included. Unlike the other parameters this is an energy independent scaling factor. By performing a simultaneous fit between the above mentioned calibration data and the respective MC simulations, four energy model parameters k_B, k_C, b, and β_{rec} were extracted. The calibration datasets are shown in comparison with best-fit MC in Fig. 6.11.

6.6 Neutrinos in the PROSPECT Detector

IBD data selection is done by subtracting reactor off correlated events from the reactor on correlated events. Correlated events in reactor on (off) case was defined by subtracting the reactor on (off) accidental rates from the respective IBD selection.

$$\mathrm{N_{corr}} = \mathrm{N_{on}} - (\Delta t_{\mathrm{corr}}/\Delta t_{\mathrm{acc}}) \cdot \mathrm{N}_{acc} \tag{6.9}$$

where $\mathrm{N_{on}}$ is the number IBD candidates that pass the IBD selection, and $\mathrm{N_{acc}}$ is the number of accidentals that pass the IBD selection. As shown in the Tab. 6.2 a wide window was used to obtain high statistics accidental dataset and the scaling factor $\kappa_t = (\Delta t_{\mathrm{corr}}/\Delta t_{\mathrm{acc}})$ was used to normalize the accidentals dataset to IBD window size.

[14]The order of operations for the analysis of MC is PG4 followed by P2X.

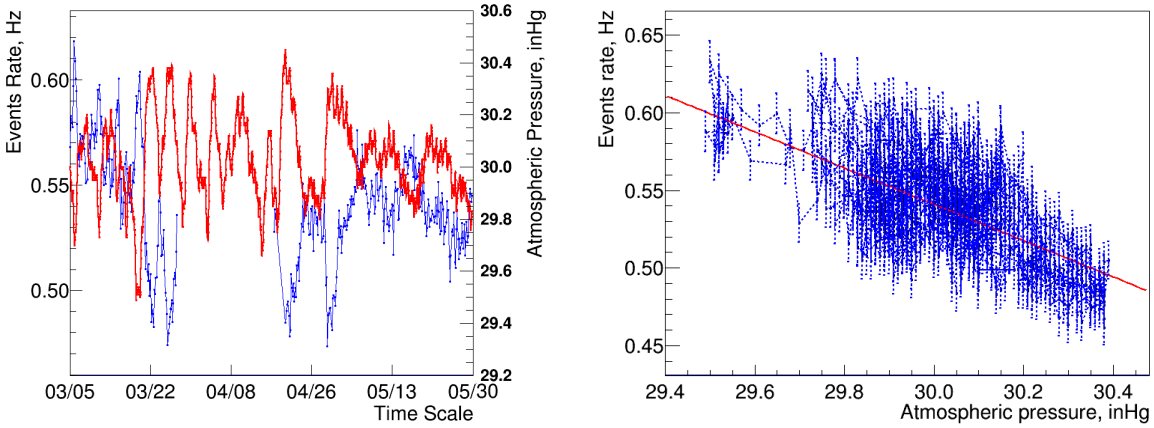

Figure 6.12. (left) FN+nLi rates and atmospheric pressure as a function of time. Anticorrelation between the two quantities could be noticed. (right) FN+nLi rates as a function of atmospheric pressure and a linear fit to extract correlations between them. Error bars shown are statistical only. The fit parameters for the red line in the right plot were used to scale the cosmogenic IBD-mimicking background rates before subtracting from the reactor on IBD candidates. See text for more details.

As defined in the Sec. 6.3, selection cuts were placed to veto cosmic muon and neutron backgrounds that mimic IBD events. These veto cuts result in dead-time during which IBD events were discarded. Being an on-surface detector, PROSPECT detects an abundance of cosmic backgrounds and consequently induces considerable dead-time. For this dataset, the dead-time varies between 6.9% to 5.5% [157] for reactor on and off cycles respectively. The variation between the on and off cycles primarily arising from the increased gamma ray backgrounds during the reactor on period. The reactor on and off times include impact from the veto dead time.

As mentioned in Sec 6.3.2, the reactor off IBD mimicking backgrounds are primarily from cosmogenic sources. Cosmogenic background rates scale inversely with pressure and has to be properly accounted for before performing on–off subtraction. To quantify the impact of pressure variations on backgrounds, delayed coincidence of fast neutron events followed by neutron capture on ^{6}Li (FN + nLi) were investigated as a function of pressure. The event selection is similar to IBD event selection with

Table 6.3. Reactor on and off correlated and accidental event rates. The effective days were calculated after scaling by veto inefficiency. Correlated rates in both reactor on and off cases are calculated by subtracting accidental rates from IBD candidate rates.

	Event type	Effective(Calendar) days	Counts	Counts/day
On	IBD candidates	30(33)	56378	1708
	Accidentals		11581	351
	Correlated		44797	1357
Off	IBD candidates	26(28)	17534	626
	Accidentals		801	29
	Correlated(scaled)		16733(19337)	598
	Signal	-	25461	771

the exception that the prompt event was required to be a fast neutron event. Shown in the Fig. 6.12 are the FN+nLi events as a function of time as well as a function of pressure. The red line shows a linear fit performed on the dataset and the fit parameters were used to define cosmogenic pressure-dependent scaling factor

$$\kappa_p = \frac{m \cdot \overline{p}_{\text{on}} + c}{m \cdot \overline{p}_{\text{off}} + c}, \tag{6.10}$$

where m and c are the slope and y-intercept of the fit and $\overline{p}_{\text{on (off)}}$ is the average pressure when the reactor is on (off).

Overall, the IBD selection is defined by

$$\begin{aligned} \mathrm{N_{IBD}} &= \mathrm{N_{corr,on}} - \kappa_p \cdot \mathrm{N_{corr,off}} \\ &= (\mathrm{N_{corr,on}}) - \kappa_t \cdot \mathrm{N_{acc,on}} - \kappa_p(\mathrm{N_{corr,off}} - \kappa_t \cdot \mathrm{N_{acc,off}}) \\ &= \mathrm{N_{on}} - (\Delta t_{\text{corr}}/\Delta t_{\text{acc}})\mathrm{N} \cdot \text{acc,on} - \kappa_p \cdot (t_{\text{on}}/t_{\text{off}}) \cdot (\mathrm{N_{off}} - (\Delta t_{\text{corr}}/\Delta t_{\text{acc}}) \cdot \mathrm{N_{acc,off}}). \end{aligned} \tag{6.11}$$

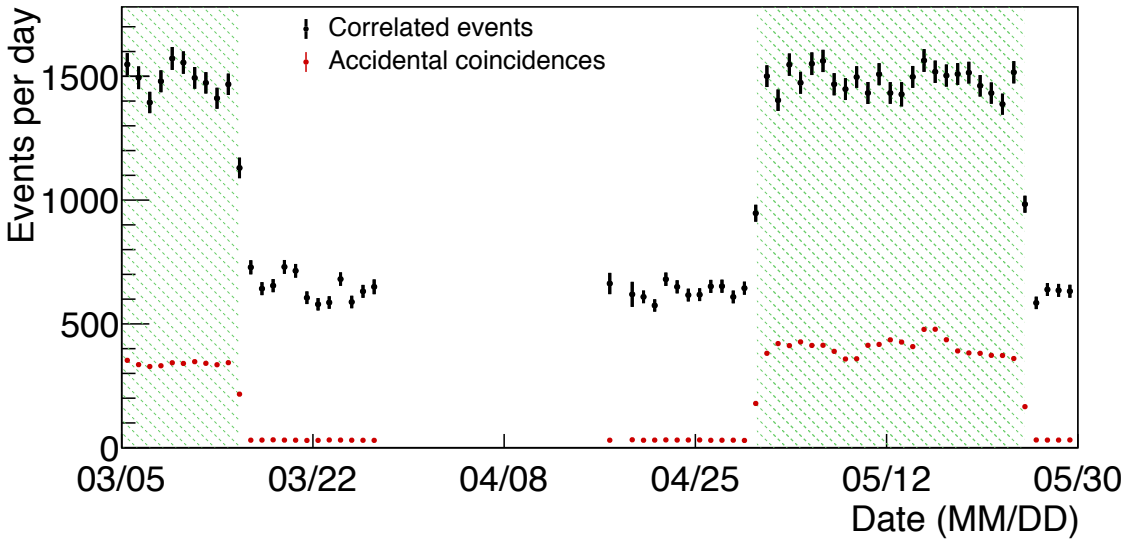

Figure 6.13. Reactor on and off correlated and accidental rates as a function of calendar days. Each bin corresponds to a single calendar day and the error bars are statistics only. Reactor on durations are shown in green shaded regions and the gaps between data corresponds to calibration and maintenance periods. The high reactor on accidental rates are due to high reactor related single rates and accidentals significantly go down when the reactor is turned off.

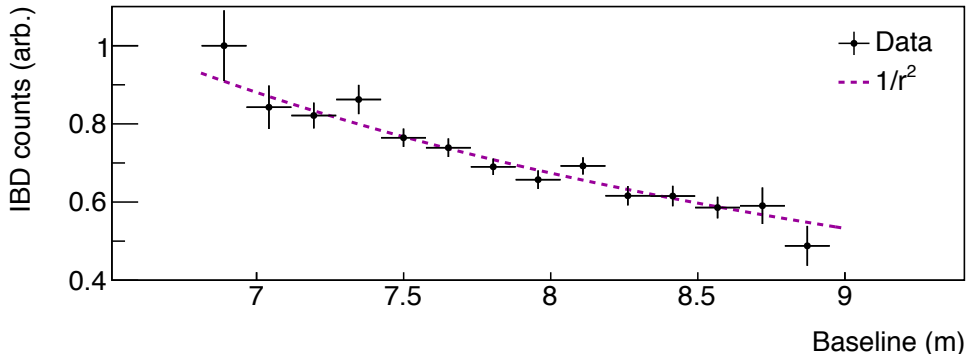

Figure 6.14. IBD event rates as a function of distance from the reactor center binned into 14 equally-spaced bins. The rates are fit to a function A/r^2, where A is the normalization fit parameter. The fit produces a $\chi 2$/NDF= 10.89/13 indicating a good agreement. The errors shown in the plot and used for the fit are purely statistical.

The dataset for this analysis includes a total of 30 (33) reactor on and 26 (28) reactor off effective (calendar) days. Using the selection criteria as described in Sec. 6.3.1, IBD candidates were selected for both reactor on and off cases. Accidental rates were also determined employing a wide time window as shown in the Tab. 6.2. The correlated event rates for on and off cases were then determined using the Eq. 6.9. IBD rates in PROSPECT detector were then estimated using the Eq. 6.11. Tab. 6.3 shows the resultant event counts and effective event rates per day for each of the event types. It can be seen that the reactor on correlated rates are higher than the reactor off correlated rates indicating Signal to background ratio of better than 1. The correlated and accidental IBD rates were relatively stable in time as shown in Fig. 6.13. The background subtracted IBD rates demonstrates inverse square law behavior as shown in Fig. 6.14.

CHAPTER 7

OSCILLATION SEARCH WITH THE PROSPECT EXPERIMENT

Chapter 6 shows the uniformity and stability of the data collected using the PROSPECT detector. The search for oscillations via disappearance of nuclear reactor-generated electron $\overline{\nu}_e$ using this data is described in this chapter. Section 7.1 describes the strategy used in searching for sterile neutrinos. Reactor and detector modeling, Monte Carlo generation of IBD events and oscillation modeling are described in the Sec 7.2. Details of the data and other inputs that went into sterile neutrino search are discussed in the Sec 7.3. Uncertainty handling and the list of uncertainties associated with the data are discussed in the Sec 7.4. The statistical approach used in assigning confidence levels is detailed in Sec 7.5. The validation and performance of the fitter is described in the Sec 7.6. Sterile neutrino search results with 33 days of reactor on PROSPECT data are reported in the Sec 7.7. Cross-checks performed on the results are described in the Sec 7.8. Finally, the impact of uncertainties on the results are shown in the Sec 7.9.

7.1 Sterile Neutrino Search Strategy

Sterile neutrino search was done by comparing the reconstructed IBD spectrum shape to the predicted IBD spectrum shape at multiple baselines. The predicted IBD spectrum as a function of baseline (called L vs E spectrum) was constructed based on a combination of MC simulations of the experiment and detector-wide reconstructed IBD spectrum. A covariance-matrix based test statistic was used to compare 3 neutrino (no sterile neutrino) hypothesis to a wide range of 3+1 neutrino (sterile neutrino) hypotheses. For sterile neutrino hypothesis, two fit parameters – Δm^2_{14} and $\sin^2 2\theta$ were defined uniformly in $\log(\Delta m^2_{14})$ and $\log(\sin^2 2\theta)$ from

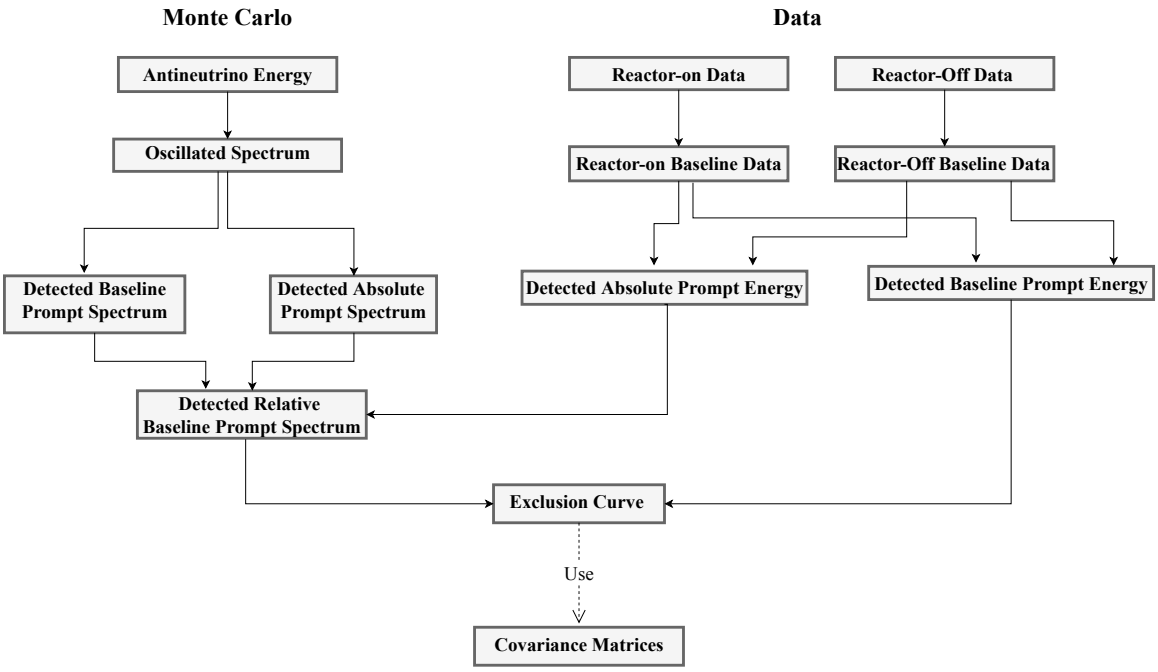

Figure 7.1. High level outline of the procedure used for sterile neutrino search with the PROSPECT experiment. The left side of the flow chart describes how detected relative baseline prompt spectrum is simulated. The right side shows the measured prompt spectra. Note that the predicted spectrum depends on the total (or absolute) measured values as described in the Eq. 7.2.

(0.1,15.0) and (0.01,1) respectively. Finer details in the exclusion curve were inspected by adding more points to Δm^2_{14} for values above 1 eV^2.

A covariance-matrix based χ^2 test-statistic was built according to the following definition:

$$\chi^2 = \mathbf{\Delta}^{\mathrm{T}} \mathbf{V}^{-1}_{\mathrm{tot}} \mathbf{\Delta}, \tag{7.1}$$

where,

$$\Delta_{l,e} = O_{l,e} - P_{l,e} = O_{l,e} - O_e \frac{M_{l,e}}{M_e} \tag{7.2}$$

where $O_{l,e}$, $P_{l,e}$ and $M_{l,e}$ are the reconstructed L vs E spectrum rates in in l^{th} position bin and e^{th} energy bin for data, prediction, and MC respectively. O_e and M_e are the reconstructed detector-wide and MC event rate respectively in e^{th} energy bin and are related to the corresponding L vs E spectra by

$$O_e = \sum_{l=1}^{L} O_{l,e}, M_e = \sum_{l=1}^{L} M_{l,e}. \tag{7.3}$$

The predicted L vs E spectrum $M_{l,e}$ includes oscillations when the hypothesis being tested is a sterile neutrino hypothesis,

$$\begin{aligned} M_{l,e} &\equiv M_{l,e}(\Delta m^2_{14}, \sin^2 2\theta) \\ &= M_{l,e}(0,0) \cdot \Big(1 - \sin^2 2\theta \cdot \sin^2 \big(1.27 \cdot \Delta m^2_{14} \ \frac{L}{E}\big)\Big), \end{aligned} \tag{7.4}$$

where, Δm^2_{14} and $\sin^2 2\theta$ are the parameters describing neutrino flavor mixing between the active flavor states and a single additional sterile neutrino state. The χ^2 defined in Eq. 7.1 can be minimized by varying the fit parameters Δm^2_{14} and $\sin^2 2\theta$. A critical characteristic of the test statistic defined in Eq. 7.1 is that it effectively eliminates the dependence of oscillation parameter fit results on the choice of the input reactor antineutrino model as shown in Sec. 7.8. The sterile neutrino search strategy used for the PROSPECT experiment is outlined in Fig. 7.1.

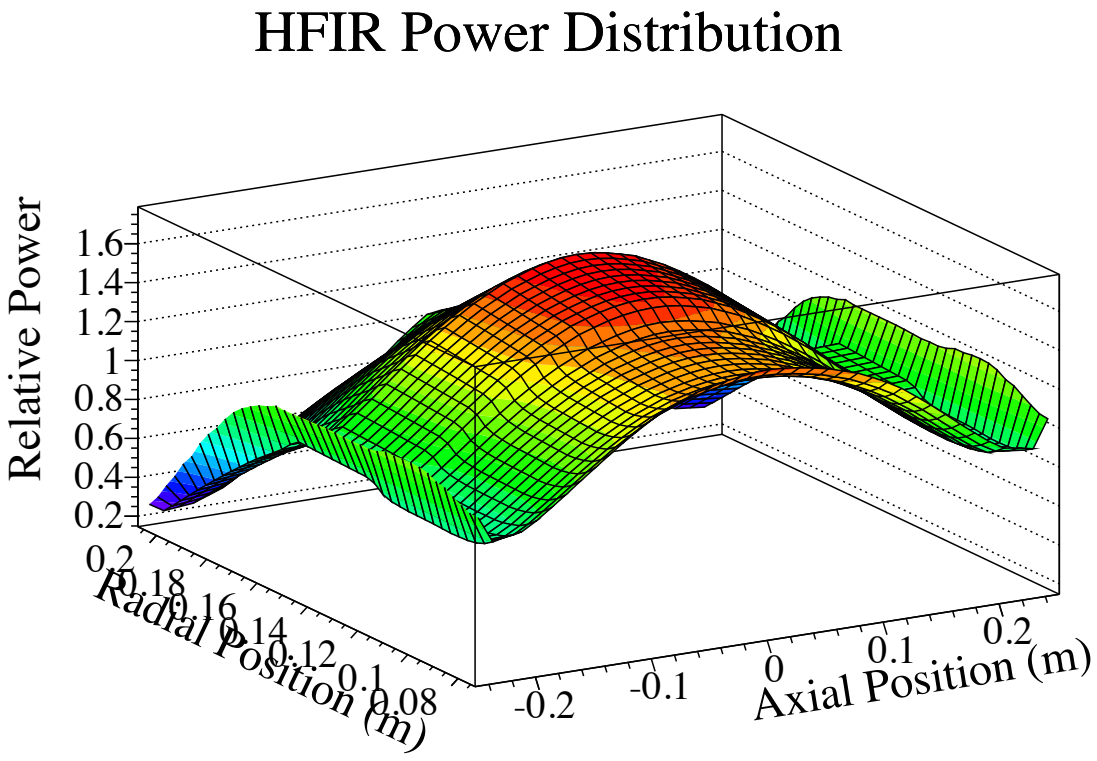

Figure 7.2. Power distribution of the HFIR reactor as a function of axial and radial positions. The fission antineutrino rate at any position in the reactor is proportional to the power at that location.

7.2 Modeling the Experiment

The IBD spectrum was built by simulating a large number $\mathcal{O}(10^7)$ of reaction points (points of origin of the neutrinos in the reactor) and corresponding detection points (IBD interaction points in the detector) assuming neutrinos travel isotropically from the reactor. The number of detection points were then scaled to the number of events detected in the IBD data set.

7.2.1 Reactor. [htpb!] HFIR is composed of two concentric core regions separated by water [158]. In case of an HEU reactor like HFIR which predominantly produces neutrinos only from a single isotope, the reactor power density is effectively proportional to the density of neutrino yield. A realistic time-averaged reactor power model

as shown in the Fig. 7.2 was utilized[15] for the MC generation of the reaction points. Detailed simulations [160] show a variation of less than 0.5 cm along the axial direction of the center of fission from the beginning through the end of a cycle. This variation is dwarfed by the uncertainty in the baseline measurement survey (10 cm) and was neglected.

7.2.2 Detector. The detector was modeled as a cuboidal box of dimensions (x,y,z)=(2044.7 mm, 1606.6 mm, 1176 mm) and placed at (6.08721 m, 0 m, 5.08508 m) away from the reactor and at a 11.31° azimuthal angle [133,161,162]. The fiducial volume of the detector was considered fully active and separated into segments by imaginary boundaries as set by the segment width (14.605 cm [163]). The proton density was assumed to be 5.46×10^{28} m^3, the same as EJ-309 proton density [127].

Detection points were randomly simulated throughout the detector with each detection point in the detector having a corresponding reaction point in the reactor. A weight of $1/r^2$ was assigned to each detection-reaction point pair where r is the baseline. The position weights of the events as a function of true baselines and segments is shown in Fig. 7.3a where the segment numbering scheme is shown in Fig. 7.8. For increased statistics, the events anywhere along the length of the segment were collapsed into one segment bin. Segment bins were further collapsed into six equally spaced baseline bins. The correspondence between segments and MC reconstructed baselines is shown in Fig. 7.3b.

Neutrinos originating from a nuclear reactor have a range of energies between ∼0-12 MeV with a very small contribution past ∼7 MeV. There are several models [84,89,99,164] describing the reactor neutrino spectrum. In this analysis, a widely

[15]It is worth pointing out that although a realistic model was used, a simplistic model of the reactor as a cylinder of height 0.5 m and radius 0.2 m has been shown [159] to accurately reproduce the core for the sake of this analysis.

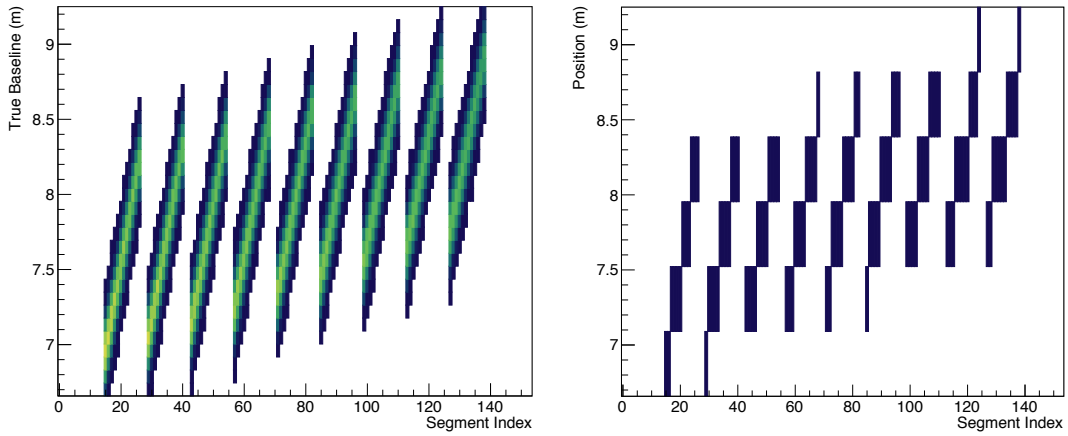

(a) The relationship between the true baselines and the fiducial segment numbers. This map shows the contribution of individual true baselines to each segment. The z scale in the map is arbitrary.

(b) The relationship between the reconstructed baselines and the fiducial segment numbers. This map shows the segments contributing to a a particular baseline.

Figure 7.3. Mapping from segments to baselines. Only fiducial segments are shown.

used model developed by Huber [164] was used. Vogel-Beacom model for IBD [89] cross-section was used to convolve antineutrino flux with the IBD cross-section to produce antineutrino spectrum. Using the above antineutrino spectrum model and the segment-baseline map from Fig. 7.3a, antineutrino spectrum models for each fiducial segment were built. Considering the outer layer of segments as non-fiducial segments, a total of 108 spectra identical in shape but varying in normalizations were built each corresponding to one fiducial segment. Figures 7.4a and 7.4b show respectively the antineutrino spectra for all the segments and the detector-wide spectrum in arbitrary units.

7.2.2.1 Non-equillibrium Isotope Contribution. The beta decays of fission isotopes are not immediate and it takes a finite amount of time to reach equilibrium. A handful of isotopes take longer to reach equilibrium and produce $\overline{\nu}_e$ above the IBD threshold. The ILL beta spectra measurements that are used as the the basis for the

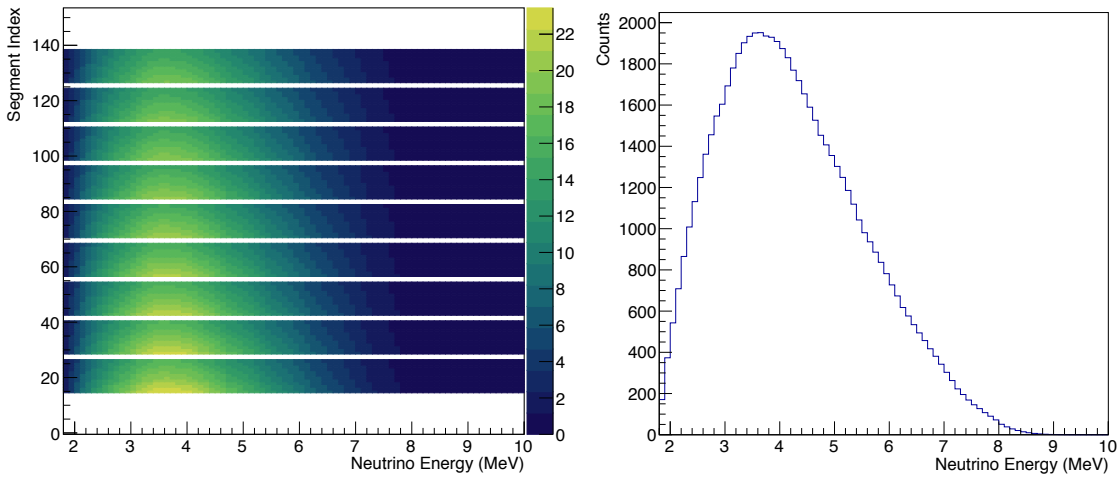

(a) Antineutrino spectrum model for all the segments.

(b) Antieutrino spectrum over the fiducial volume of the full PROSPECT detector.

Figure 7.4. Modeled $\overline{\nu}_e$ spectra convolved with the IBD cross-section.

Huber spectrum prediction were done after short irradiation time ∼1 day. Since that is not enough irradiation time for the long-lived of the isotopes to reach equilibrium, small contribution from the long-lived isotopes has been accounted for in this analysis by extrapolating from the suggested corrections in the Table VII from Ref. [99]. Non-equilibrium corrections are estimated [165] to contribute ∼0.5% over the full analysis period with most of the contribution in the low energy (below 4MeV) region as shown in the Fig. 7.5.

7.2.2.2 Contribution from non-fissile material. The fuel used in HFIR reactor core is U_3O_8-Al [16]. In addition to Aluminum being part of the fuel, it is also used as fuel filler and in structural components of the core. ^{27}Al has a non-negligible neutron capture cross-section converting it into ^{28}Al which then beta decays to produce $\overline{\nu}_e$ as

[16]The reactor core uses ^{9}Be in the reflector. Neutron capture on ^{9}Be could produce ^{6}He which beta decays to ^{6}Li producing $\overline{\nu}_e$. The $\overline{\nu}_e$contribution from the ^{6}He beta decays <0.5% and was not considered for sterile neutrino search [166].

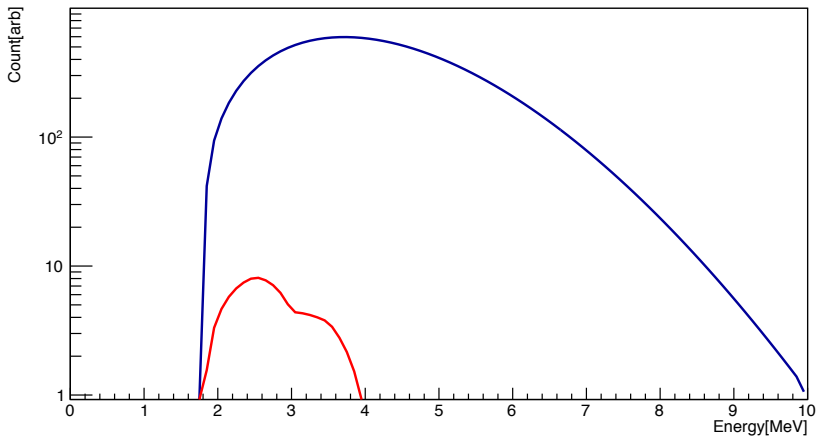

Figure 7.5. Contribution from non-equilibrium isotopes (red) in comparison with ^{235}U Fission spectrum (blue).

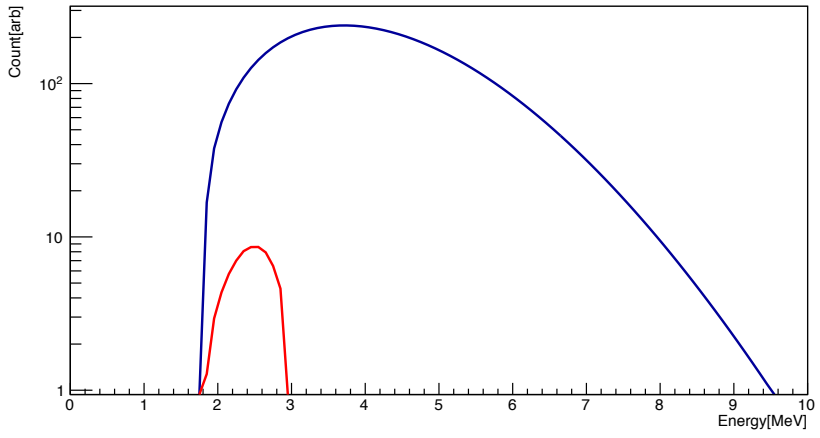

Figure 7.6. Contribution from beta decay of ^{28}Al (red) in comparison with ^{235}U Fission spectrum (blue).

follows:

$$^{27}_{13}\mathrm{Al} + ^{1}_{0}n \rightarrow ^{28}_{13}\mathrm{Al} \rightarrow ^{28}_{14}\mathrm{Si} + \beta^{-} + \overline{\nu}_e. \tag{7.5}$$

The beta decay of $^{28}_{13}$Al has a half-life of 2.24 minutes with an end point energy of 2.86 MeVčitefirestone1999table. MCNP [167] was used to model [123] the $\overline{\nu}_e$ contribution from the beta decay of ^{28}Al. Aluminum corrections are estimated [168] to contribute ∼1.0% over the full analysis range with a significant amount of contribution below 3 MeV as shown in the Fig 7.6.

7.2.3 Detector Response. To build a realistic detected spectrum from the MC antineutrino spectrum, several response effects must be taken into account. Following detector effects play an important role in the PROSPECT experiment:

- **$\overline{\nu}_e$ to e^+ conversion**

  In IBD interaction, the prompt energy is lower than the $\overline{\nu}_e$ inducing it by 0.782 MeV as described in Sec. 3.2.

- **Quenching and Cherenkov contributions**

  The quenching of energy by the scintillator is a nonlinear effect that changes the amount of scintillated light with significantly lower amounts of scintillated light emitted for lower energies. The quenching effect is modeled using Birk's law [155, 169, 170]. Cherenkov effect also introduces a small amount of energy nonlinearity with relatively more scintillated light emitted for higher energies. The amount of visible Cherenkov light is modeled by an ad-hoc efficiency parameter. Birk's and Cherenkov parameters were extracted from MC fits to calibration data as described in Sec. 6.2.4.

- **Efficiency**

  The detector is not 100% efficient in detecting IBD events. Analysis cuts reduce the backgrounds by a few orders of magnitude, but they also cause a reduction

in detection efficiency of IBDs. The detection efficiency varies with energy and position of the IBD event in the detector.

- **Energy Loss**

  The PROSPECT detector consists of $\sim 4\%$ inactive volume within the fiducial volume contributed primarily by separators, pinwheels, and calibration tubes. Some of the positron and annihilation gamma energy is absorbed by the dead volume and goes undetected. Since higher energy positrons travels through more dead volume, the energy loss increases with increasing $\overline{\nu}_e$ energy.

- **Escaping Gammas**

  Positron from IBD annihilates with an electron in the detector and releases two gammas each with at least 0.511 MeV. These gammas have a long range in a scintillator detector and some of the gammas escape from the scintillating volume before depositing all their energy. This will be seen as a reduction in the energy detected from the true deposited energies. The effect gets more pronounced the farther away from the center the IBD interaction takes plays.

- **Energy Resolution**

  The observed prompt spectrum is smeared out primarily from the poisson photo-statistics in addition to the PMT quantum efficiency and the detector geometry as described in the Sec. 6.2.4.

The response of the detector to IBD interactions was taken into account through detector response matrices. In PG4, neutrinos were simulated with a flat energy spectrum in the range of 1.8-10 MeV in 0.1 MeV wide bins. Using the same analysis chain (P2x) [151] as the one used for data, simulated $\overline{\nu}_e$ rates were mapped to reconstructed IBD prompt rates individually for all segments. The total reconstructed energy of an IBD event is the sum of calibrated energies detected by all

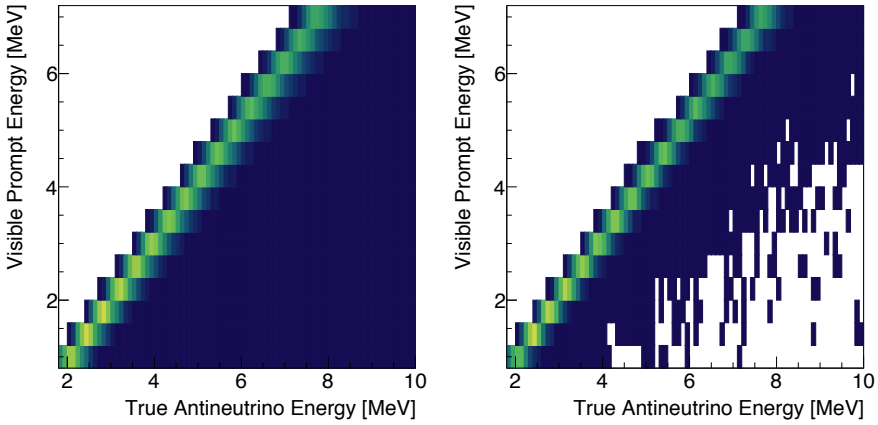

(a) Detector response matrix for the full detector.

(b) Detector response matrix for a segment (segment number 77) in the center of the detector.

Figure 7.7. Response of the detector to neutrinos over the energy range of interest. These response matrices were generated using PG4 for IBD interactions generated throughout the detector. Note that the binning is finer in true antineutrino energies and coarser in visible energies.

the segments. For this analysis, only reconstructed prompt energy spectrum range of (0.8,7.2) MeV with 0.4 MeV wide bins were used. Some PMT channels in the detector had fluctuating currents, therefore these PMTs were turned off for further investigation and the segments (inactive segments) containing these PMTs were not included in the analysis. Consequently, to accurately build response matrices, the contribution to reconstructed energy from these segments were deliberately ignored. Any segment that contained a turned-off PMT at the end of the data taking period was considered non-functional for the complete analysis period. [171]. Fig. 7.8 shows the map of inactive segments considered in this analysis.

The full detector response matrix and the detector response matrix of segment 77 are shown in the Fig. 7.7. A convolution of true $\overline{\nu}_e$ for a segment with the corresponding response matrix produces the MC prompt energy spectrum for that segment. The outcome of folding the detector response matrices with the true

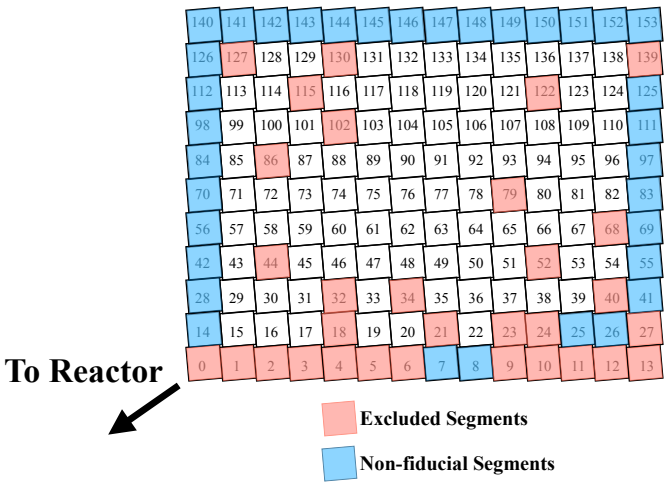

Figure 7.8. The segment numbering scheme [172] used for this analysis. Also shown are the ignored segments (pink) and non-fiducial segments (blue). Due to a beam pipe running close to the east edge of the detector, segments 25 and 26 had relatively high accidental background rates and hence these segments were assumed to be non-fiducial as well.

$\overline{\nu}_e$ from 7.4a, 7.4b are shown in the Figs. 7.9a and 7.9b.

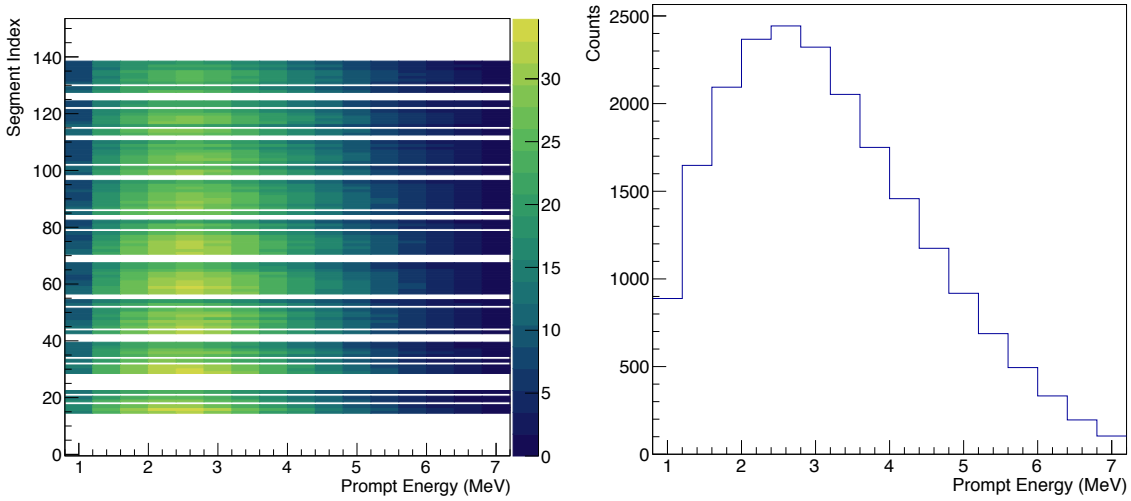

(a) 2D histogram of visible energy spectrum as a function of segments. Blank spaces indicate inactive and non-fiducial segments.

(b) visible spectrum over the full detector.

Figure 7.9. Reconstructed MC prompt energy spectrum.

7.2.4 L vs E Spectra. Using the segment-baseline map as shown in the Fig. 7.3b, the segment-energy histogram shown in Fig. 7.9b was translated into baseline-energy histogram. Spectra from all the segments that corresponds to a particular baseline as indicated by Fig. 7.3b were added to obtain the spectrum for that particular baseline.

Overall, the unoscillated MC visible spectrum $P_{null}(L, E_p)$ as a function of baseline (L) and prompt energy (E_p) can be written in mathematical form as:

$$M(L, E_p) = W_{th} \cdot s(E_\nu)/4\pi L^2 \cdot t \cdot \epsilon_D(L, E_\nu, E_p) \cdot \rho_P V_D \cdot \sigma(E), \tag{7.6}$$

where W_{th} is the thermal power of the reactor, $s(\overline{\nu}_e)$ is the $\overline{\nu}_e$ spectrum at energy E, L is the $\overline{\nu}_e$ baseline, t is the exposure time, ρ_P is the proton density of liquid scintillator, V_D volume of the detector, $\sigma(E)$ is the IBD interaction cross-section, and $\epsilon_D(L, E_\nu, E_p)$ is the efficiency of detecting neutrino of energy E_ν at a baseline L. It is important to note that M is a function of prompt energy and $\epsilon_D(L, \overline{\nu}_e, E_p)$ is not just the efficiency, but it encompasses all the detector effects and it maps from neutrino energy to prompt energies. The visible baseline spectra generated using the above procedure are shown in Fig. 7.10.

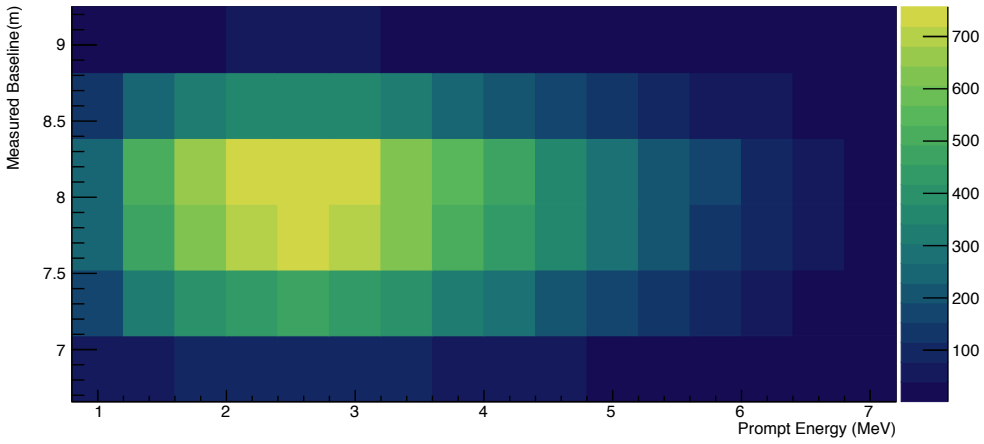

Figure 7.10. 2D histogram of modeled visible energy spectrum as a function of baseline. Higher rates around 8 meters is because dividing the baselines into equal width bins places more segments in the baseline bins in the center than the edges.

7.2.5 Oscillations. [htpb!] The survival probability of reactor antineutrinos under two-neutrino approximation is given by

$$P_{ee} = 1 - \sin^2 2\theta \cdot \sin^2 \left(1.27 \cdot \Delta m^2 \frac{L}{\overline{\nu}_e} \right), \tag{7.7}$$

where L is in meters and E is in MeV. Fig 7.11 gives an idea of the number of entries in the baseline-energy bins and the effect of the oscillation in one particular case. Oscillation will appear as a small difference in the shape of the spectrum which is evident from the ratio of oscillated to unoscillated spectra.

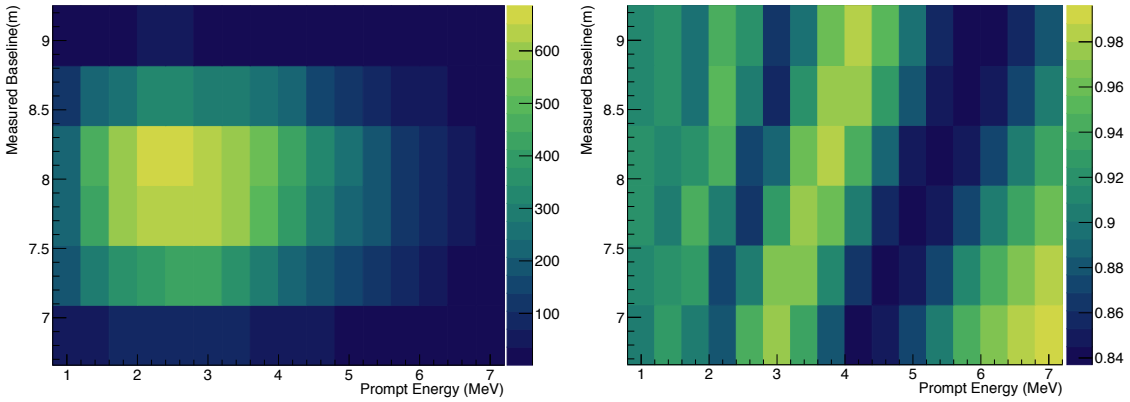

(a) L vs E spectrum in case of sterile neutrino oscillations.

(b) Noticeable oscillation pattern seen in the ratio between the oscillated and unoscillated spectra.

Figure 7.11. The expected number of events in each L and E bin in presence of oscillations. For this example the oscillations corresponding to RAA best-fit were used.

7.3 Data and Inputs

Data taking with fully installed PROSPECT detector started on 4^{th} March 2018. After finishing initial calibration work, the wet commissioning commenced at the end of February. The commencement of production data which includes part of wet commissioning started 14 days into the HFIR cycle 478. The production data taking was halted for part of the reactor off period between cycles 478 (ending on

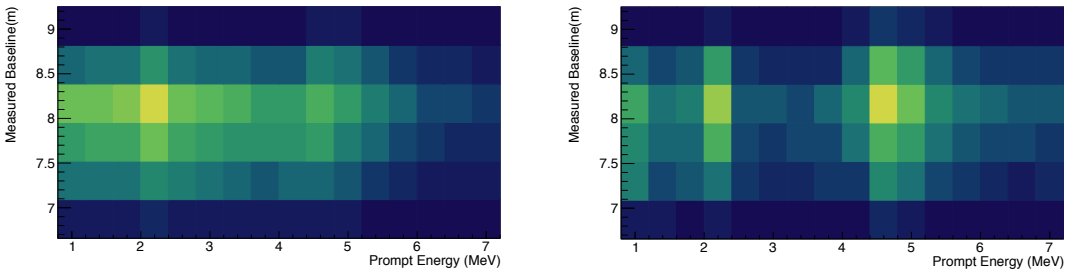

(a) Reactor on correlated+accidental spectra

(b) Reactor off correlated+accidental spectra

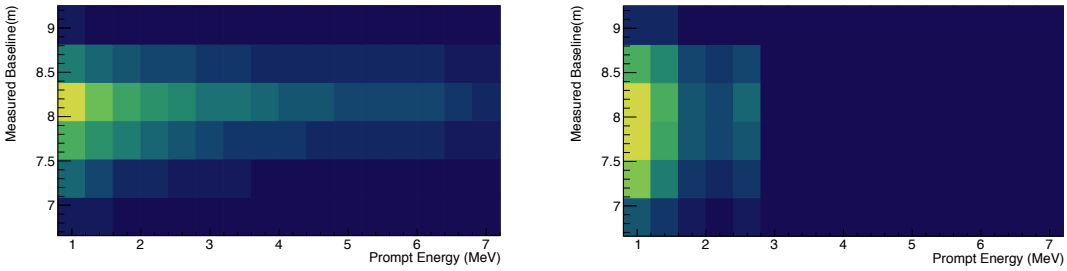

(c) Reactor on accidental spectra

(d) Reactor off accidental spectra

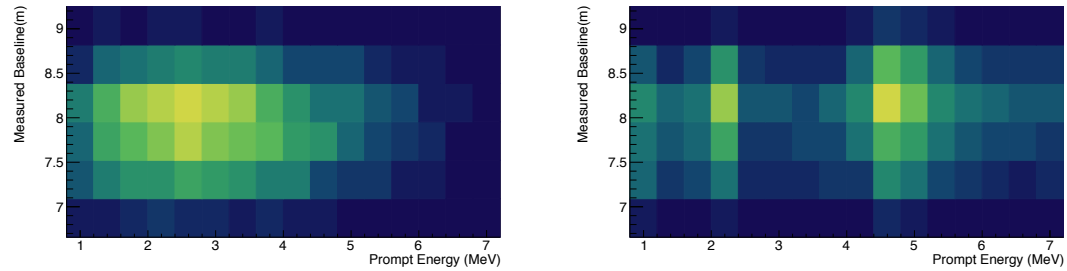

(e) IBD signal spectra used for the oscillation analysis

(f) IBD-mimicking reactor off spectra

Figure 7.12. Measured spectra as a function of baseline. Significant peaks could be noticed around 2MeV and 4 MeV for the reactor on correlated+accidental, reactor off correlated+accidental which arises from the cosmogenic backgrounds. Event rates are higher for the baselines in the center these baselines encapsulate more segments.

16^{th} March) and 479 (starting on 1^{st} May) to perform detector maintenance and calibration work. For this analysis, the dataset from 4^{th} March to 25^{th} May was used which includes 2 reactor on cycles and 1 reactor off cycle.

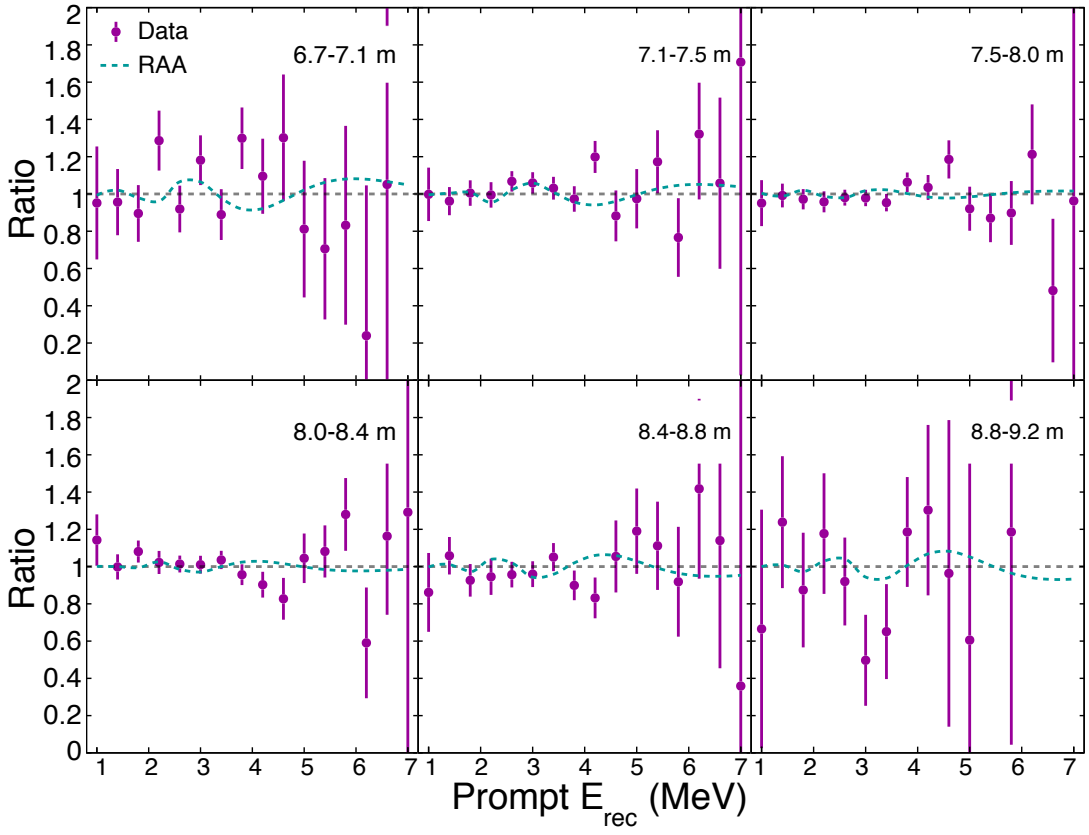

Figure 7.13. Ratio of measured to the predicted IBD spectra($O_{l,e}/P_{l,e}$) for six baselines from 6.7 to 9.2 m. Error bars include both statistical and systematic uncertainties. Also shown are $O_{l,e}/P_{l,e}$ spectra for the unoscillated (dotted gray) and RAA best-fit (dotted green) oscillation scenarios.

As mentioned in the Sec. 7.2.3, several segments were turned off because they showed current fluctuations and were removed from dataset altogether. During the maintenance period PMT functionality tests have shown that some of the turned off PMTs gained back their functionality and were consequently turned back on. The dataset was optimized roughly to maximize the total IBD signal by discarding some data collected right before the maintenance period such that PMTs that were turned

off for a very short period of time could still be used.

After processing through the calibration, reconstruction, and event selection phases, four distinct IBD-like event classes were generated as described in Sec. 6.3. The segment grouping described in the Sec. 7.2.2 was used and all the four datasets were grouped into six baselines. The reconstructed IBD candidate spectra as a function of baseline for all the four event types are shown in Fig. 7.12. Also shown in the figure is the signal and reactor off background rates constructed using Eq. 6.11. After background subtraction, a total of 25461 IBD events were collected over 33 (30) calendar (effective) reactor on days yielding 771 IBDs per day. Fig. 7.13 shows $O_{l,e}/P_{l,e}$ for data, null oscillation and the RAA best-fit oscillation case. In case of no sterile neutrino oscillations, a flat line for all baselines as the spectrum shape should remain unchanged over the detector baseline. The figure also shows the oscillation signature for RAA best-fit oscillation parameters.

7.4 Uncertainty Handling

For this analysis, all uncertainties (both statistical and systematic) were introduced in form of covariance matrices. Mathematical description and the motivation behind using covariance matrix approach is described in detail in Appendix A.1. With 16 energy bins and 6 position bins, the covariance matrix is a square matrix consisting of 96×96 terms. Uncertainties associated with stochastic fluctuations of the measured IBD rates (statistical uncertainties) are uncorrelated between baselines and are just extracted from the dataset. Systematic uncertainties associated with detector and reactor are input in form of a reduced covariance matrix. A reduced covariance matrix is a statistics-free (or normalized) version of the covariance matrix describing the correlation between bins as described in App. A.1. Each systematic uncertainty has an associated reduced covariance matrix which was produced via the generation of toy datasets. More details of the covariance matrix generation using

toys are provides in App. A.1. Under the assumption that all the errors are gaussian, total covariance matrix is just the sum of all statistical and systematic covariance matrices.

$$\mathbf{V}_{\text{Total}} = \mathbf{V}_{\text{Stat}} + \sum_i \mathbf{V}_{\text{Syst},i}. \tag{7.8}$$

Shown in the Tab. 7.1 is the list of covariance matrices, their associated uncertainties and the rationale behind generation of the covariance matrices. Uncertainty assignment and the generation of associated covariance matrices are described in the following sections.

7.4.1 Statistics. The statistical uncertainties were generated by taking poisson error of the measured IBD statistics. The measured IBD rates were given in the equation Eq. 6.11, the resultant statistical covariance matrix is given by

$$\mathbf{V}_{\text{Stat}} = \mathbf{V}_{\text{Total,rxOn}} + \mathbf{V}_{\text{Acc,rxOn}} + (\text{t}_{\text{on}}/\text{t}_{\text{off}})^2 \cdot (\kappa_p)^2 \cdot \big(\mathbf{V}_{\text{Total,rxOff}} + \mathbf{V}_{\text{Acc,rxOff}}\big), \tag{7.9}$$

where $\mathbf{V}_{\text{Total}}$ and $\mathbf{V}_{\text{Acc}}$ are the covariance matrices obtained from the measured total and accidental IBD candidates respectively for reactor on and off cases, κ_p is the scaling factor associated with the average pressure differential between reactor on and reactor off and t_{on} and t_{off} are given by the reactor on and reactor off run times respectively as shown in the Eq. 6.11.

Since the predicted spectra for each baseline is generated by scaling the total reconstructed L vs E spectrum (O_e) as shown in the Eq. 7.2, the statistical covariance matrix has to take the correlation between $O_{l,e}$ and O_e into account. The statistical covariance matrix including correlations arising from the addition of baseline-integrated spectrum is given by

$$\mathbf{V}_{\text{Stat,l,e}} = \sigma^2_{\text{Stat,l,e}} \cdot (1 - 2\frac{M_{l,e}}{M_e}) + \sigma^2_{\text{Stat,e}} \cdot \big(\frac{M_{l,e}}{M_e}\big)^2, \tag{7.10}$$

Derivation for the covariance matrix is given in Appendix A.3.

Additionally, off-diagonal terms in the covariance matrix that correspond to same energy bins across all the position bins have correlations arising from the usage of baseline-integrated spectrum O_e in the prediction. These correlations are included by generating MC toys and extracting the reduced covariance matrix from the resultant correlations.

7.4.2 Fully Correlated Detector-wide Systematics. The systematics that impact the full detector in a similar manner are considered here. In all the cases below the covariance matrix was generated by generating toys by varying the relevant parameters the same way throughout full detector.

7.4.2.1 Energy Response. The full detector energy response covariance matrix takes the following four full detector energy response effects into account. A full description of the these response effects and their evaluation is given in the Sec. 6.2.4.

1. Scintillator quenching
2. Cherenkov effect
3. Energy independent energy scale
4. Energy resolution

These four parameters were estimated simultaneously by comparing MC to calibration. Consequently a single covariance matrix was generated for all the four parameters. For generating the covariance matrices, the default values (μ) and the uncertainties (σ) of all four parameters were considered as shown in the Tab. 7.1. Four random values were independently generated assuming four corresponding gaussian distributions $\mathcal{N}(\mu, \sigma)$ one for each response effect. Several toys each corresponding to one set of randomly generated response parameters were simulated using PG4. After

Table 7.1. List of systematic uncertainties assumed in generating the covariance matrices.

Systematic uncertainty	Default Value	σ	Motivation for value/sigma chosen
Background normalization	-	5%	Cosmogenic FN+nLi has an uncertainty in correlation coefficient of <0.2%. 5% assumed as conservatively.
Birks' non-linearity	0.1	0.012	Fit parameters and the corresponding fit uncertainties obtained from simultaneous fits between data and MC for a combination of sources as described in Sec. 6.5. Conservatively, the uncertainties considered here are slightly higher than
Cherenkov Contribution	51%	4%	
Energy scale	1	0.007	
Energy resolution	0.0445	0.002	
Energy loss	N/A	30 keV	Maximum variation anywhere within the detector between data and MC for ^{22}Na was found to be 30 keV and was conservatively used.
Background scaling	-	0.002	Variation in BiPos between reactor on and off periods were of the order 0.2%
Uncorrelated volume	-	-	The uncertainty in fits to the RnPo rates for each segment.
Uncorrelated efficiency	-	5%	Variation of the MC-generated efficiencies within the detector found to <5%, 5% conservatively assumed.
Uncorrelated energy resolution	0.0445	0.002	Replicated the value obtained from the full detector data-MC fits.
Uncorrelated energy loss	-	30 keV	Replicated the value from the full detector data-MC comparison.
Baseline uncertainty	7932 mm	100 mm	Estimated from the detector survey.
^{28}Al contribution	-	100%	Assumed 100% since the contribution is very small (0.5%).
Non-equillibrium isotope contribution	-	100%	Estimates were based on theory, and the uncertainty conservatively assumed 100% since the contribution is very small(<1%).
Background peak non-uniformity uncertainty	-	5%	The variation in nH to nC peak heights found to be <5%. A conservative estimate of 5% assumed.

passing each MC through P2x, covariance matrix was generated using Eq. A.31.

7.4.2.2 Escaping Gamma Energy. The PROSPECT detector being relatively small has some of the annihilation gamma energy escaping from the detector. The energy loss is simulated by PG4 package and an uncertainty was assigned based on the inaccuracy of the PG4 simulation. ^{22}Na, a positron source was deployed at multiple positions along the length of the segment at multiple positions in the detector. The maximum difference noticed between ^{22}Na calibration data and the corresponding MC was conservatively used as the energy loss uncertainty [173].

7.4.2.3 Background Energy Scale. The IBD dataset was generated by subtracting reactor off correlated IBD candidate spectrum from reactor on correlated IBD candidate spectrum. The IBD signal could be impacted if the detector energy scale varies between reactor on and reactor off data taking periods. This has been taken into account in form of a BG scaling covariance matrix. Energy scale was estimated by examining the shift in the BiPo [174] and the RnPo [175] energy scales over time.

7.4.2.4 Background Normalization. The main source of reactor off correlated backgrounds are cosmogenic neutrons. Both cosmogenic neutrons are atmospheric pressure dependent, the pressure dependence is taken into account by normalizing the reactor off correlated IBD candidates spectrum as shown in the Eq. 6.11 before subtraction. The total uncertainty in the pressure over the data taking period translates to an uncertainty in the background normalization [176].

7.4.2.5 Baseline Uncertainty. Markers indicating the position of the detector segments in relation to the outside edge of the detector were installed on the detector during the post-assembly survey. The reactor to detector distance was estimated by measuring the distance from the detector markers to already existing markers in the

reactor facility. The uncertainty corresponding to the baseline was estimated to be 10 cm [161] based on the markers in the detector. The covariance matrix was generated assuming a gaussian error in the baseline.

7.4.2.6 ^{28}Al Uncertainty and Non-equilibrium Contribution. The MC L vs E spectrum includes a contribution from Aluminum activation and Non-equilibrium isotopes as mentioned in the Secs. 7.2.2.2, 7.2.2.1. The $\overline{\nu}_e$ spectrum for both of these cases is in (0,4) MeV $\overline{\nu}_e$ energy range and contributes $\sim$1.5% together over the full spectrum range. Since the overall contribution to the MC spectrum is relatively small, the uncertainty was conservatively assumed to be 100%.

7.4.3 Segment-to-segment Uncorrelated Systematics. There are a group of uncertainties that are fully uncorrelated either between segments or baselines. Each of these systematic uncertainties have an associated covariance matrix and were generated first in the Seg vs E bins and then converted to L vs E bins using the mapping detailed in Appendix A.2.

7.4.3.1 Volume Variation. The liquid scintillator was doped with ^{227}Ac and the measured RnPo α event rates in each segment is taken as a proxy for the relative volume of each segment. The uncertainty in the RnPo rates measured in segment was used to generate toys for that respective segment uncorrelated with the other segments.

7.4.3.2 Efficiency Variation. PG4 simulation was used in generation of detector response matrices. A conservative uncertainty of 5% uncorrelated between segments was assumed.

7.4.3.3 Energy Scale. The energy scale could be different between individual segments primarily arising from non-uniform calibration. Comparison of energy scales from calibration sources have shown uniformity within 0.5% as shown in the

Fig. 6.9 [174], [177], [175].

7.4.3.4 Energy Loss. The energy loss because of the gamma leakage and energy deposition in the dead volume may vary between segments. In particular, the gamma leakage is position dependent with more energy leaking closer to the edge of the detector. The difference between ^{22}Na calibration data and corresponding MC that produced the maximum value was conservatively used as the energy loss uncertainty.

7.4.3.5 Energy Resolution. The energy resolution is primarily depended on the number of photoelectrons detected by the PMTs. The number of photoelectrons observed by the PMTs could vary between the segments based on varying LS conditions or the reflectivity of the separators. The uncertainty for this covariance matrix was produced by conservatively assuming the same resolution uncertainty as was used for the full detector.

7.4.3.6 Background Peak Non-uniformity Uncertainty. The prompt event of the main class of IBD mimicking backgrounds are from gammas generated from the neutron capture on Hydrogen (nH) and the neutron inelastic scattering on Carbon (nC). nH produces gammas with a 2.2 MeV peak and nC produces 4.4 MeV peak. Variations in nH peak size to nC peak has been found within the detector primarily based on the variations in the muon veto cut. The variation can be attributed to the fact the neutrons producing nH peak originate primarily from muon spallation on the detector material whereas neutrons producing nC are from single muon events. Toys were generated by assuming gaussian distributions for 2.2 MeV and 4.4 MeV and varying the size of the peak by 5%. The covariance matrix was generated by assuming that the variation was completely uncorrelated between segments as well as between the nH and nC peaks.

Once all the covariance matrices were generated, two reduced systematic co-

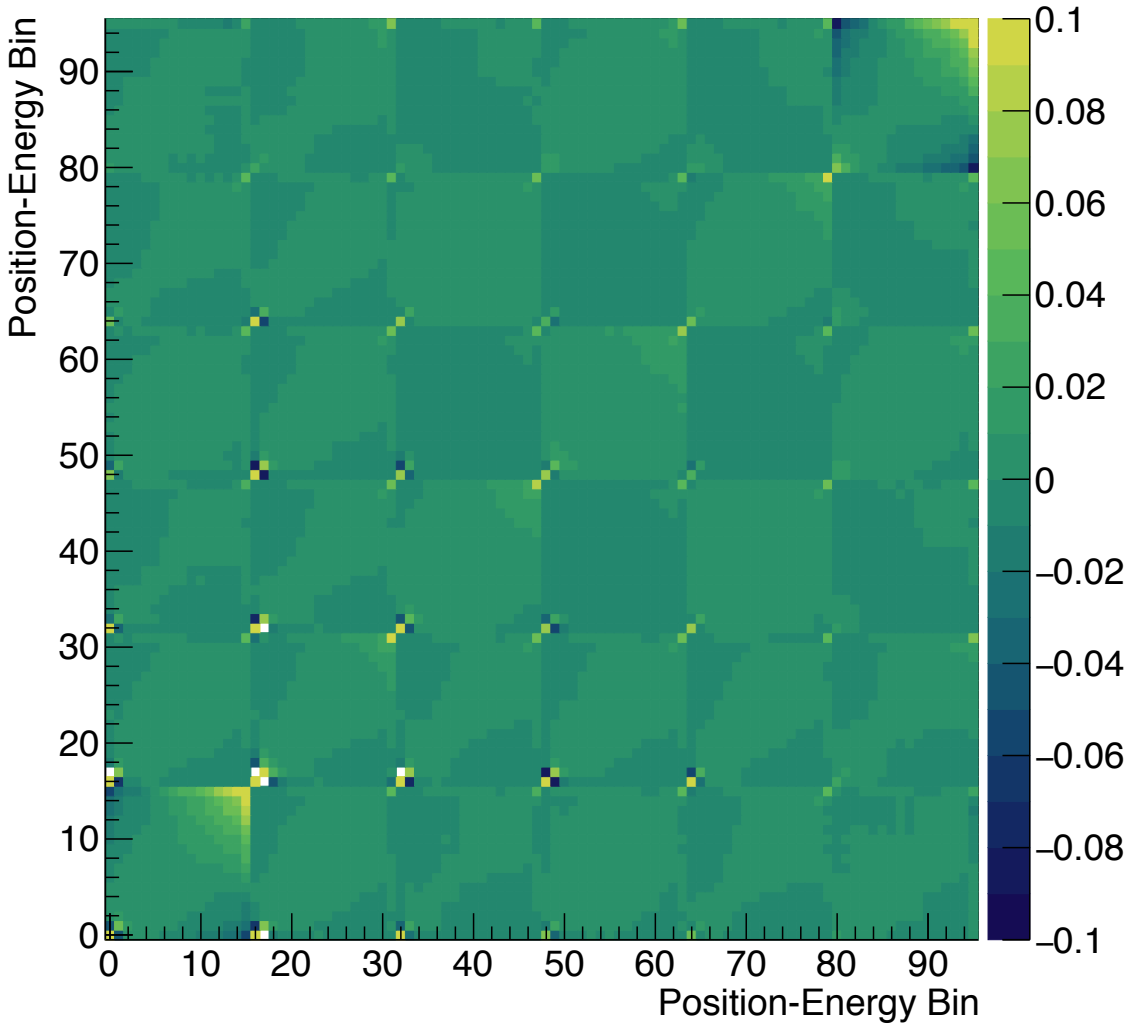

Figure 7.14. Reduced covariance matrix of all the signal related systematics. Each bin in the matrix corresponds to a distinct position-energy bin and each block matrix of 16x16 bins correspond to all energy bins for a specific position bin. Positive values show positive correlations whereas negative values show anti-correlations. Since diagonal terms in the matrix shows the uncertainties in each position-energy bin, they are always positive (positively correlated). On the other hand the non-diagonal terms show the correlations between different bins and could be positive or negative depending on the correlations between bins. Detector-wide systematics acts similarly for the matching energy bins across all the position bins. Most extreme values seen in the matrix are primarily from the bin edge effects.

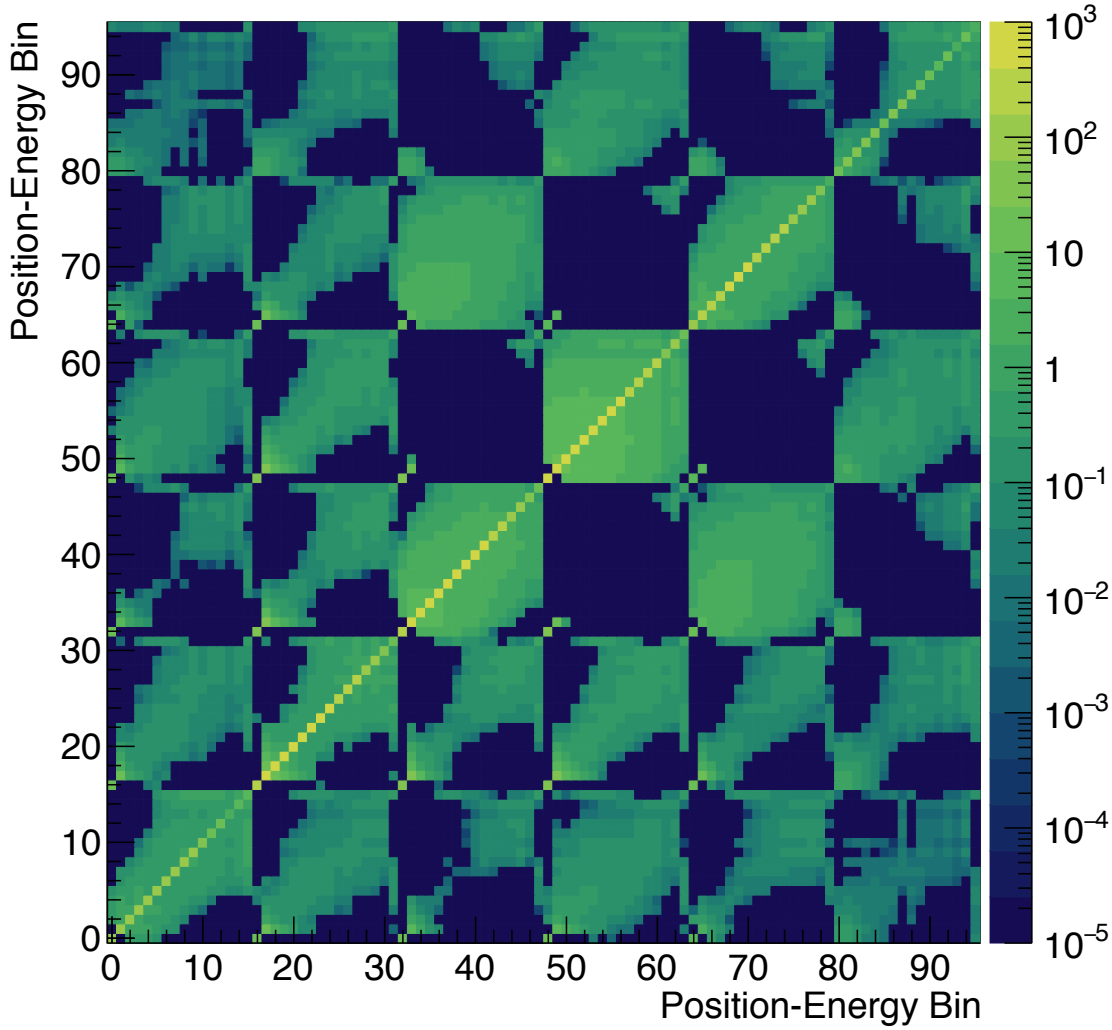

Figure 7.15. Signal covariance matrix including both statistical and systematic uncertainties. Z-axis is shown on log scale to illustrate the correlations between bins across baselines. Statistical uncertainties dominate as can be noticed from the large values of diagonal elements. Similarities between block diagonal matrices across various baselines can be noticed.

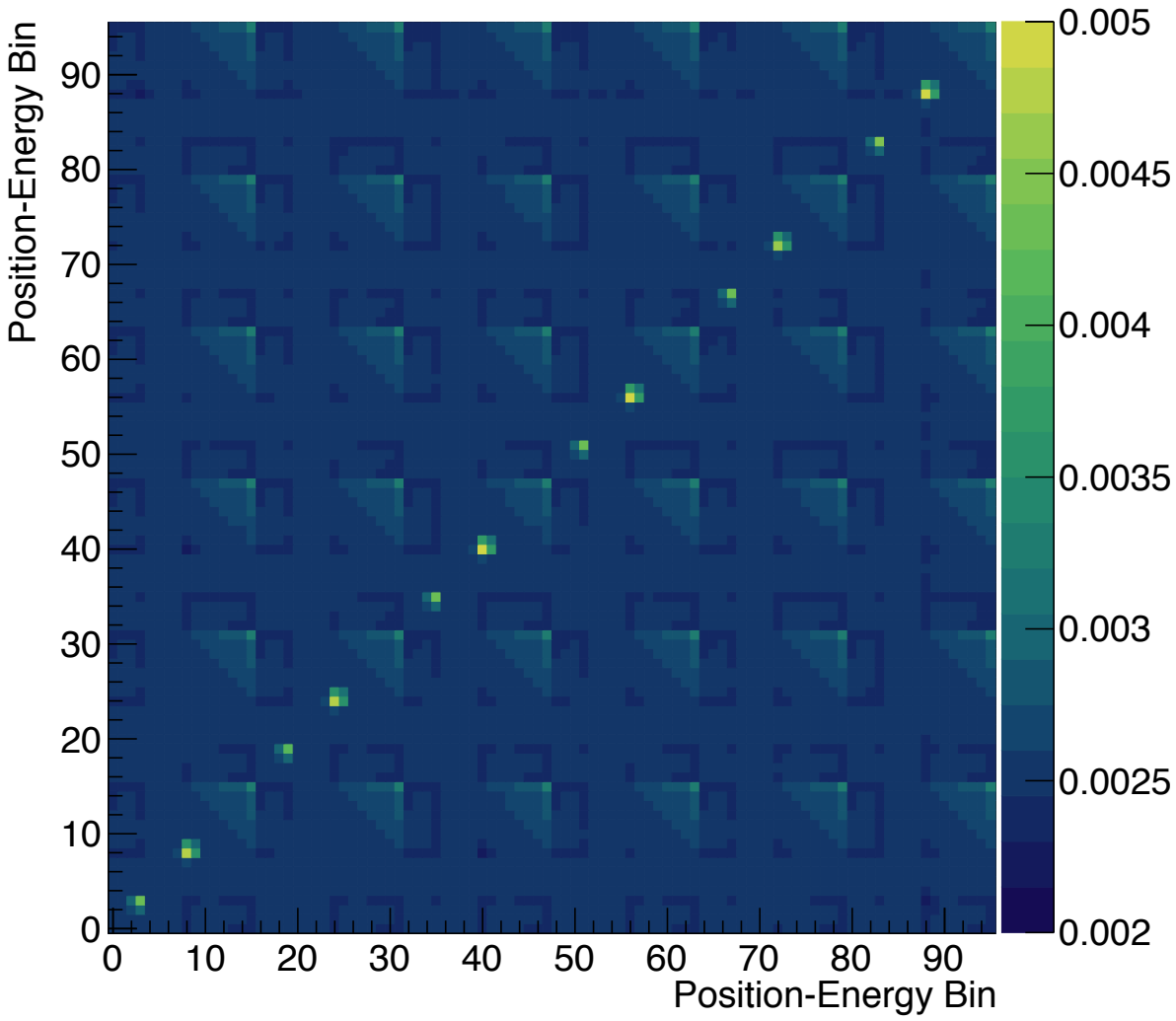

Figure 7.16. Reduced covariance matrix of all the background related systematics. Since the only uncertainties uncorrelated between segments/baselines are the peak uncertainties, all the terms except the block diagonal matrices are identical for the matching energy bins across all position bins. The high values along the diagonal terms are for the nH and nC peaks as expected.

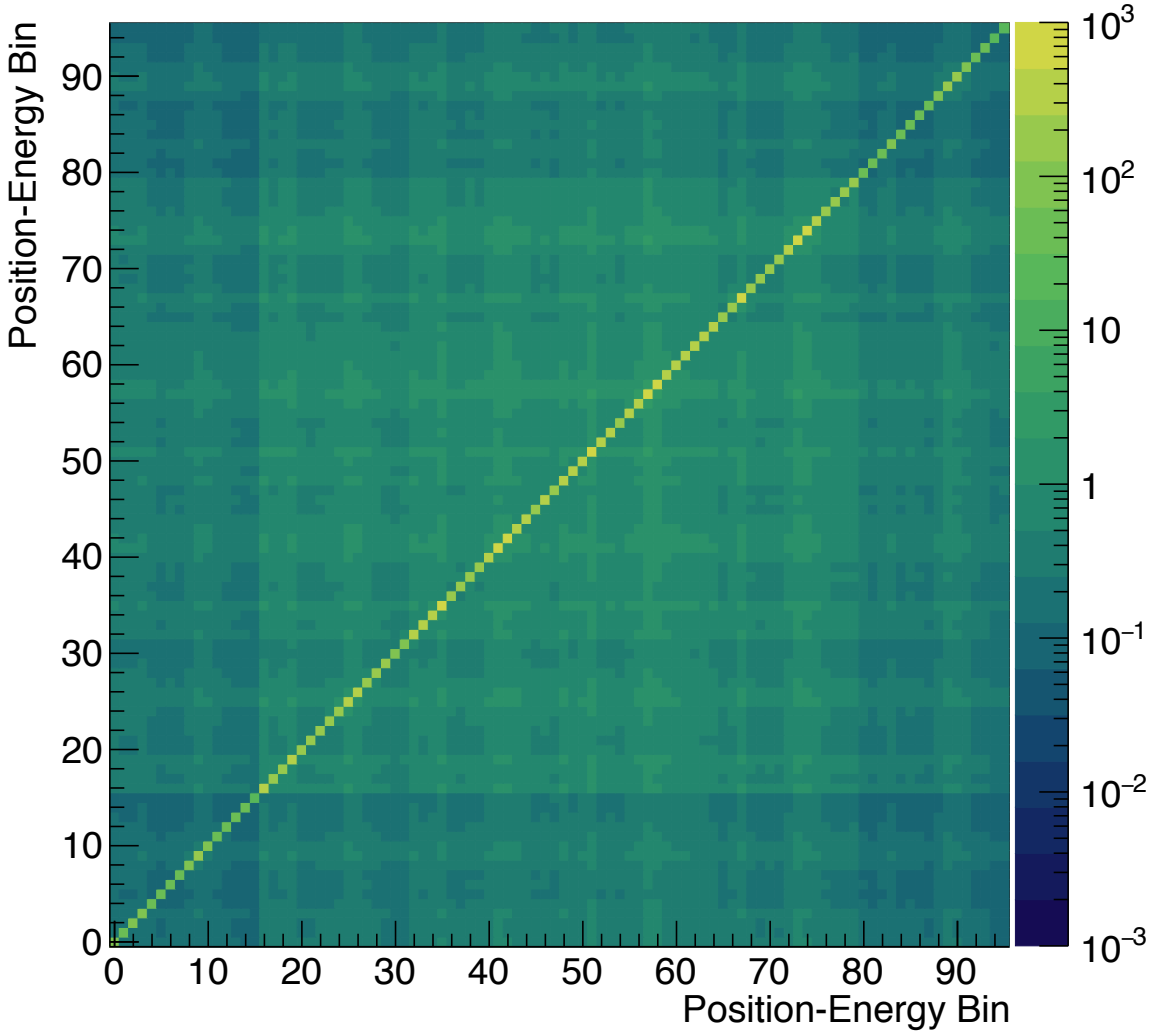

Figure 7.17. Background covariance matrix including both statistical and systematic uncertainties. Z-axis is shown on log scale to illustrate the correlations between bins across baselines. Statistical uncertainties dwarf the systematical uncertainties.

variance matrices were generated one each for the signal and the backgrounds by adding individual covariance matrices bin-by-bin. The total signal (background) systematic covariance matrix was then generated by using

$$\mathbf{V}_{sig,tot} = \mathbf{O}^{\mathrm{T}}\mathbf{V}_{sig,red}\mathbf{O} \tag{7.11}$$

$$\mathbf{V}_{bg,tot} = \mathbf{BG}^{\mathrm{T}}\mathbf{V}_{sig,red}\mathbf{BG} \tag{7.12}$$

Where $\mathbf{V}_{sig,red}$ and $\mathbf{V}_{bg,red}$ are the reduced covariance matrices (96×96) for the signal and background respectively and $\mathbf{O}$ and $\mathbf{BG}$ are the 96 element-long signal and background vectors respectively. The systematic covariance matrices for signal and background are shown in Fig. 7.14 and Fig 7.16 respectively. Similar pattern of behavior could be seen across multiple baseline bins indicating similar uncertainties across baselines. The matrices are then added according to the Eq. 7.8 and are shown in the Figs. 7.15 and 7.17 respectively. It is very evident that in both cases, the matrices are dominated by the statistical uncertainties.

It is worth noting that the statistical covariance matrices were derived from data while the systematic covariance matrices were generated using the predicted spectrum. This is to avoid a common pitfall [178] (pages 101-105) that biases the results when measured values are used to define the systematical uncertainties.

7.5 Confidence Interval Assignment

To properly assign confidence intervals, a full frequentist approach as proposed by Feldman and Cousins [179] was used in this analysis. A unique value ($\Delta\chi^2_C$) for each ($\sin^2 2\theta$,Δm^2_{14}) point was generated for a specific confidence level (CL) employing the following steps:

1. For each point in the ($\sin^2 2\theta$,Δm^2_{14}) grid, 1000 oscillated MC toy datasets were

generated following the strategy described in Appendix A.4.

2. For each of the toy datasets, χ^2_{min} for every point in the grid was generated using Eq. 7.1 where the toy dataset was used instead of data.

3. $\Delta\chi^2 = \chi^2_{\text{min,true}} - \chi^2_{\text{min,best-fit}}$ was then extracted where $\chi^2_{\text{min,true}}$ and $\chi^2_{\text{min,best-fit}}$ are the χ^2_{min} for the true oscillation parameters and the best-fit oscillation parameters respectively for the toy under consideration.

4. Steps 1-3 were then repeated for all the toys and a $\Delta\chi^2$ distribution was generated for each $\sin^2 2\theta$ and Δm^2_{14}. Shown in the Fig. 7.18 are the $\Delta\chi^2$ distributions for no oscillation and RAA oscillation hypotheses.

5. A separate value of $\Delta\chi^2_C(\alpha)$ for each point in the Δm^2_{14}-$\sin^2 2\theta$ grid corresponding to α confidence level was generated such that $\frac{\sum_0^{\Delta\chi^2_C} P(\Delta\chi^2)}{\sum_0^{\infty} P(\Delta\chi^2)} = \alpha$, where $P(\Delta\chi^2)$ is the $\Delta\chi^2$ distribution from step 4.

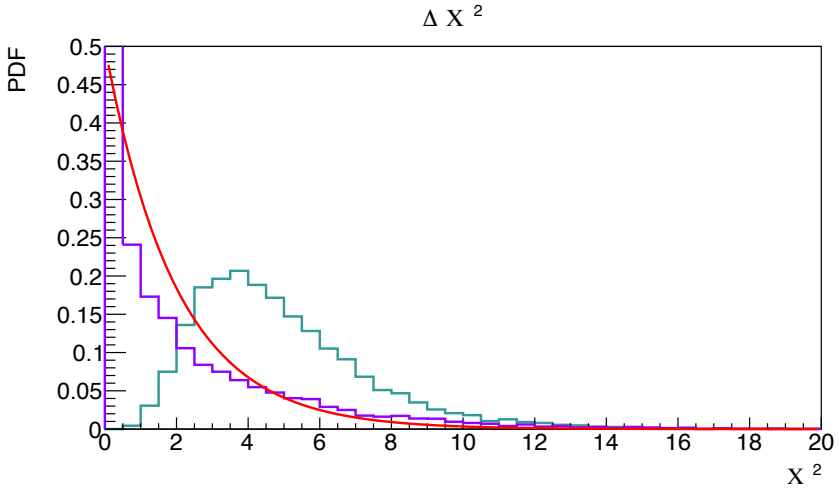

Figure 7.18. Probability distribution function of $\Delta\chi^2$ for RAA oscillation (purple) and null oscillation (teal) hypotheses. Also shown in red is the Wilk's theorem-predicted $\Delta\chi^2$ distribution for two degrees of freedom.

Shown in the Fig. 7.19 are the 90% and 95% CL χ^2_C values for the full parameter space. A point in oscillation parameter grid is said to be excluded by the data at α

confidence level if $\Delta\chi^2_{data} > \Delta\chi^2_C$ where $\Delta\chi^2_{data}$ is obtained from the data following Eq. 7.1 and $\Delta\chi^2_C$ was obtained at the specific oscillation parameters.

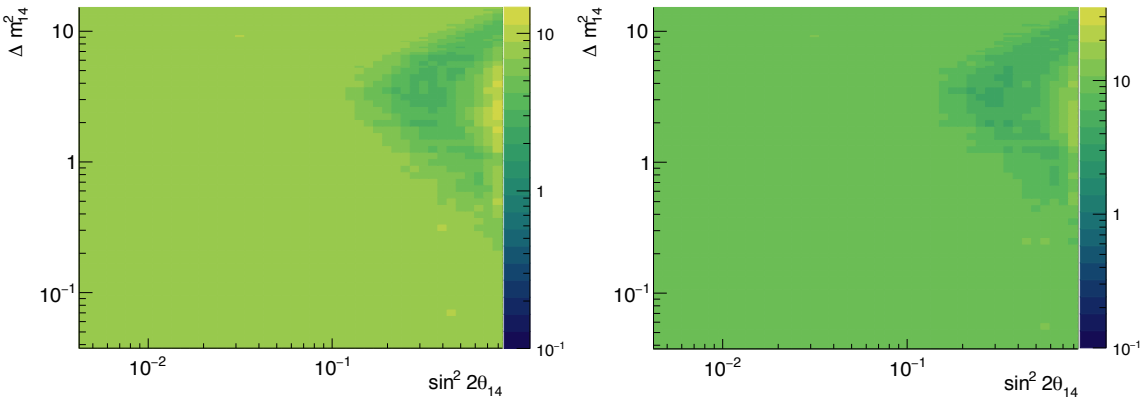

Figure 7.19. Critical $\Delta\chi^2$ values for all the points in the ($\sin^2 2\theta$,Δm^2_{14}) parameter space for 90%(left) and 95%(right) confidence levels.

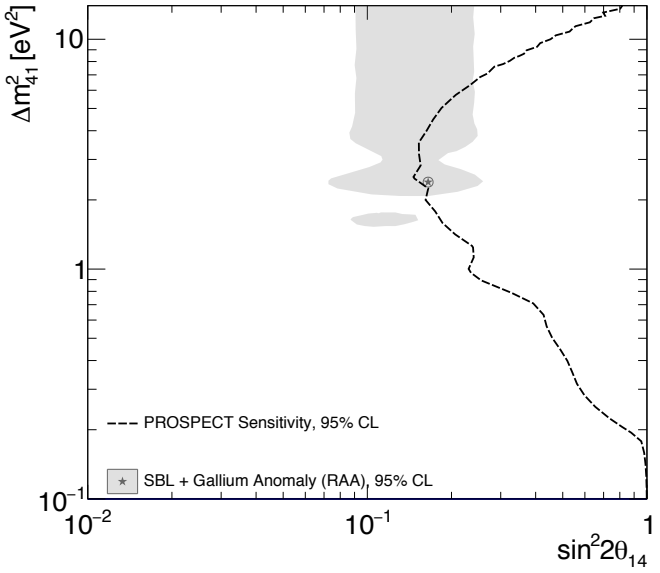

Figure 7.20. Sensitivity of the PROSPECT experiment at 95% CL.

Shown in the Fig. 7.20 is PROSPECT's sensitivity for the dataset size used in this analysis generated using 10000 unoscillated toys. The fluctuations in toys included statistical and systematic uncertainties as defined in the Sec. 7.4. For each toy, a 95% exclusion curve was generated using the procedure described above. The

sensitivity of the experiment was then generated by taking the median of all the exclusion curves.

7.6 Fitter Validation and Performance

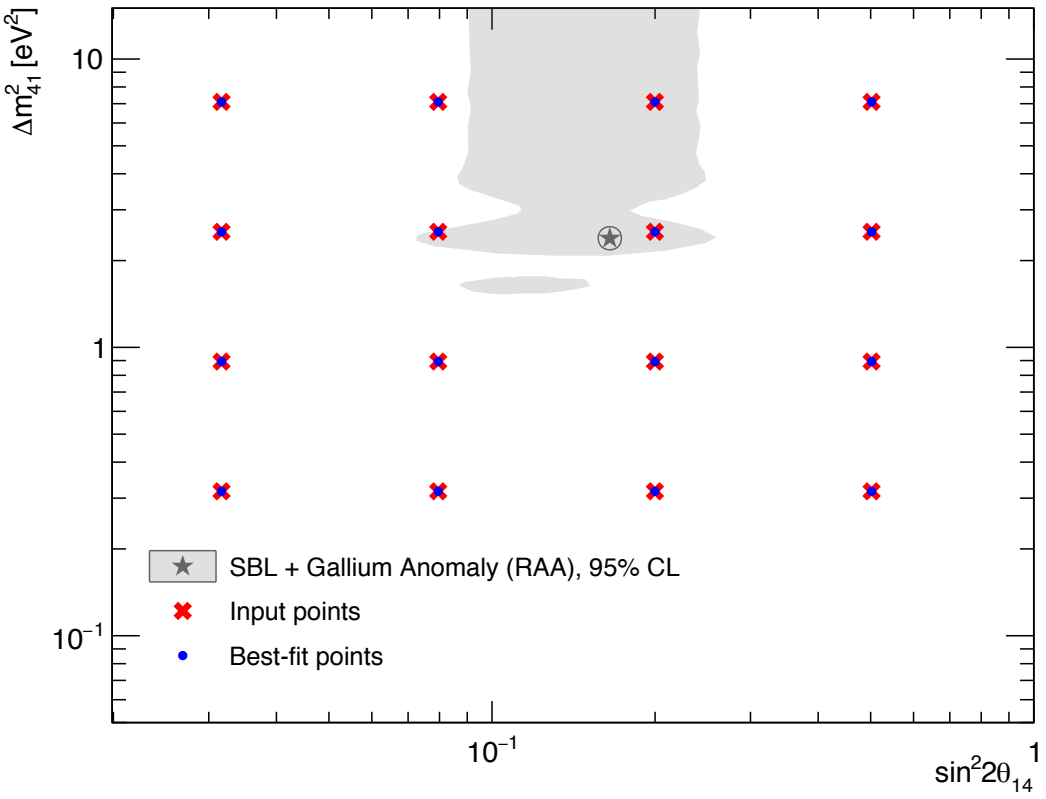

Figure 7.21. Validation of fitter in reproducing input oscillation parameters. Shown in red crosses are the oscillation parameters of the supplied toy datasets and in blue are the best-fit oscillation parameters generated by the fitter.

The effectiveness of the fitter in reproducing inputs oscillation parameters was tested using toys without statistical and systematic fluctuations. Oscillated toy datasets for 16 points equally spaced in log scale in the ($\sin^2 2\theta$,Δm^2_{14}) grid were supplied as inputs to the fitter and the resultant best-fit points were compared to the input values. Results shown in Fig. 7.21 demonstrate the validity of the fitter in reproducing input oscillation parameters. Small deviations in the low ($\sin^2 2\theta$,Δm^2_{14})

regions far from the sensitivity of the experiment were found, but the differences in χ^2 for all the cases were found to be $\mathcal{O}(0.001)$ and are possibly from the rounding errors in inversion of the covariance matrices.

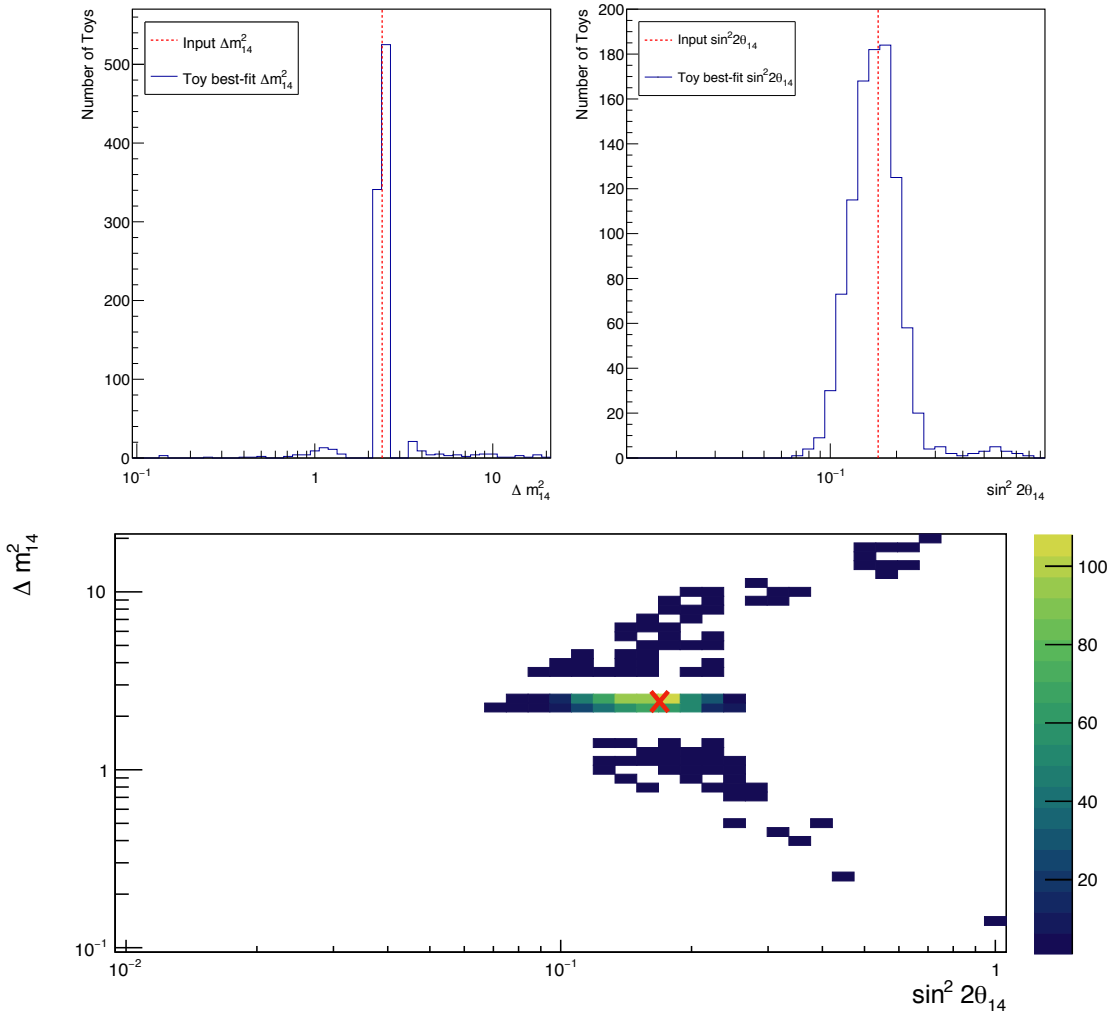

Figure 7.22. Distributions of the best-fit values produced by fitting MC datasets generated using RAA best-fit oscillation parameters ($\sin^2 2\theta$, Δm^2_{14})=(0.165,2.39). The distributions have median values of ($\sin^2 2\theta$, Δm^2_{14})=(0.159, 2.42) and are centered around the true values. The peaks with smaller amplitudes in Δm^2_{14} corresponds to frequencies of oscillation that are offset by 2π. The analysis technique relies on oscillation shape distortion as a function of energy and position but is not dependent on the absolute normalization. This in turn implies that the fitter is more sensitive to fluctuations in Δm^2_{14} and less sensitive to fluctuations in $\sin^2 2\theta$. This can be noticed from the broader distribution of $\sin^2 2\theta$ compared to Δm^2_{14}.

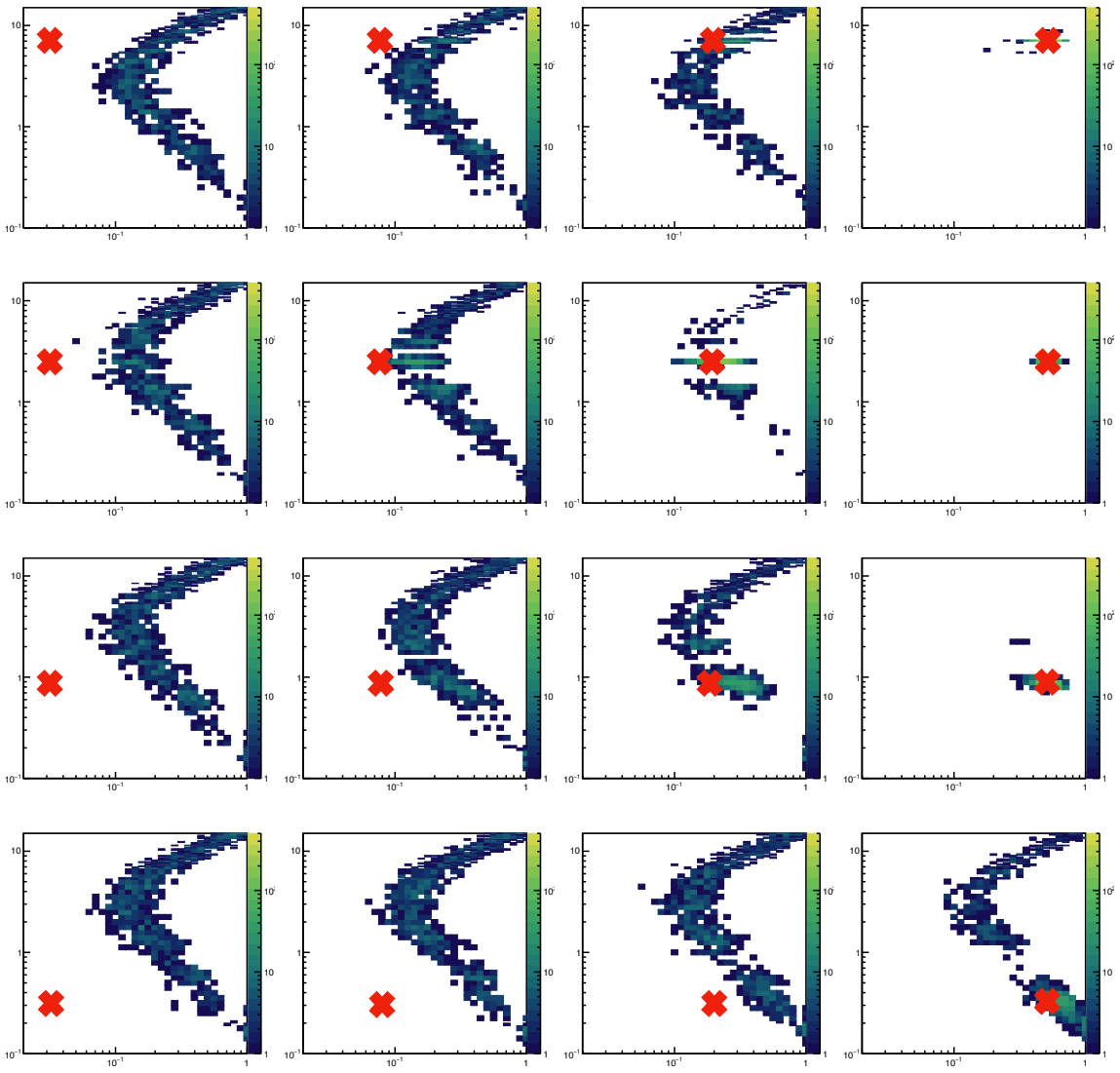

Figure 7.23. Best-fit $\sin^2 2\theta$ and Δm^2_{14} distribution for MC toys generated using 16 different input oscillation parameters. The input and the best-fit oscillation parameters are in agreement for the points in the parameter space sensitive to the detector.

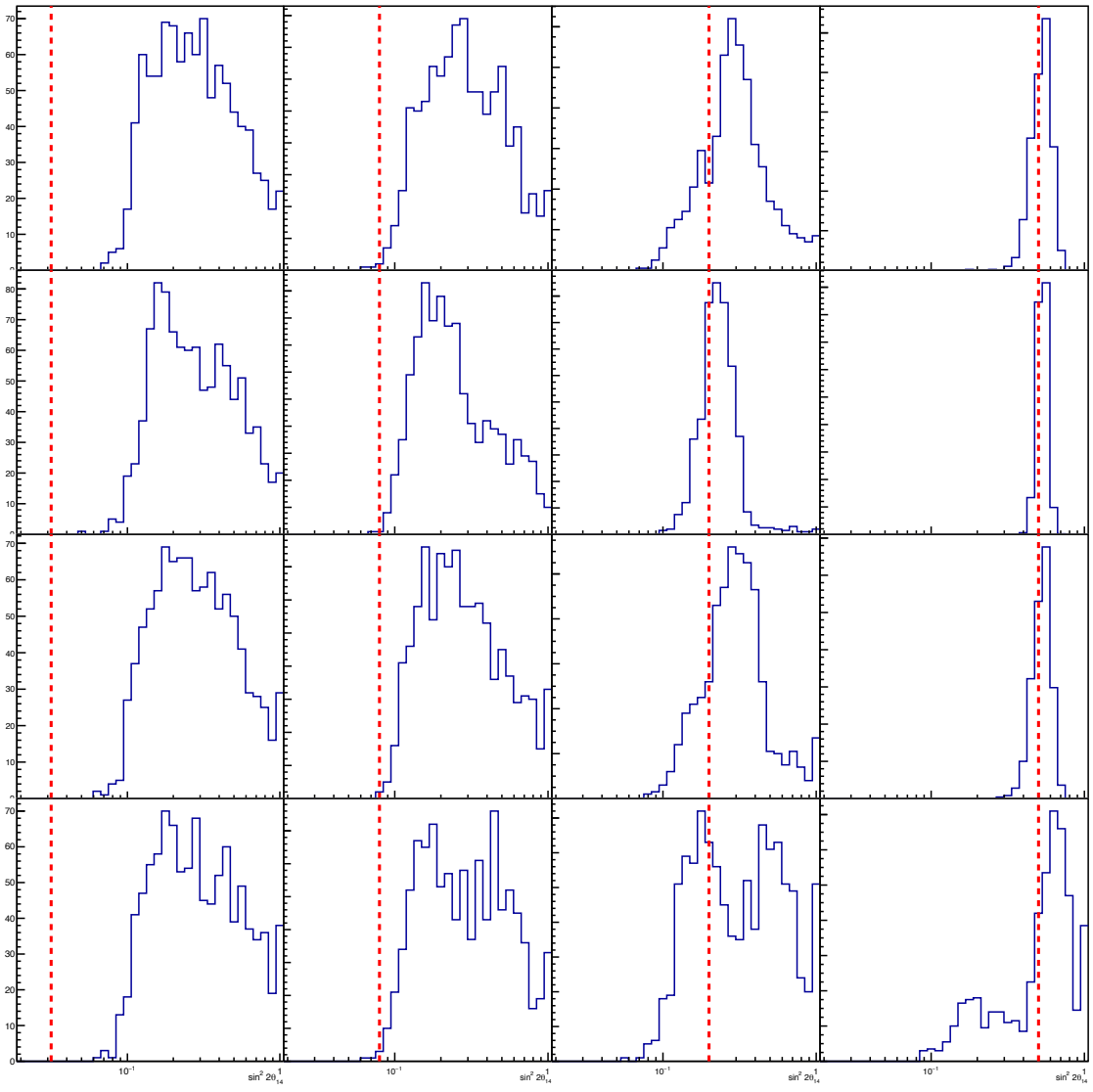

Figure 7.24. Best-fit $\sin^2 2\theta$ distribution for MC toys generated using the same 16 different input oscillation parameters as the ones used in Fig. 7.23. The distributions are centered at higher $\sin^2 2\theta$ because the detector is not sensitive to small oscillation amplitudes and the fluctuations (statistical and systematic) leads the fitter to produce a smaller χ^2 for an oscillation amplitude in a close vicinity of the sensitivity of the detector.

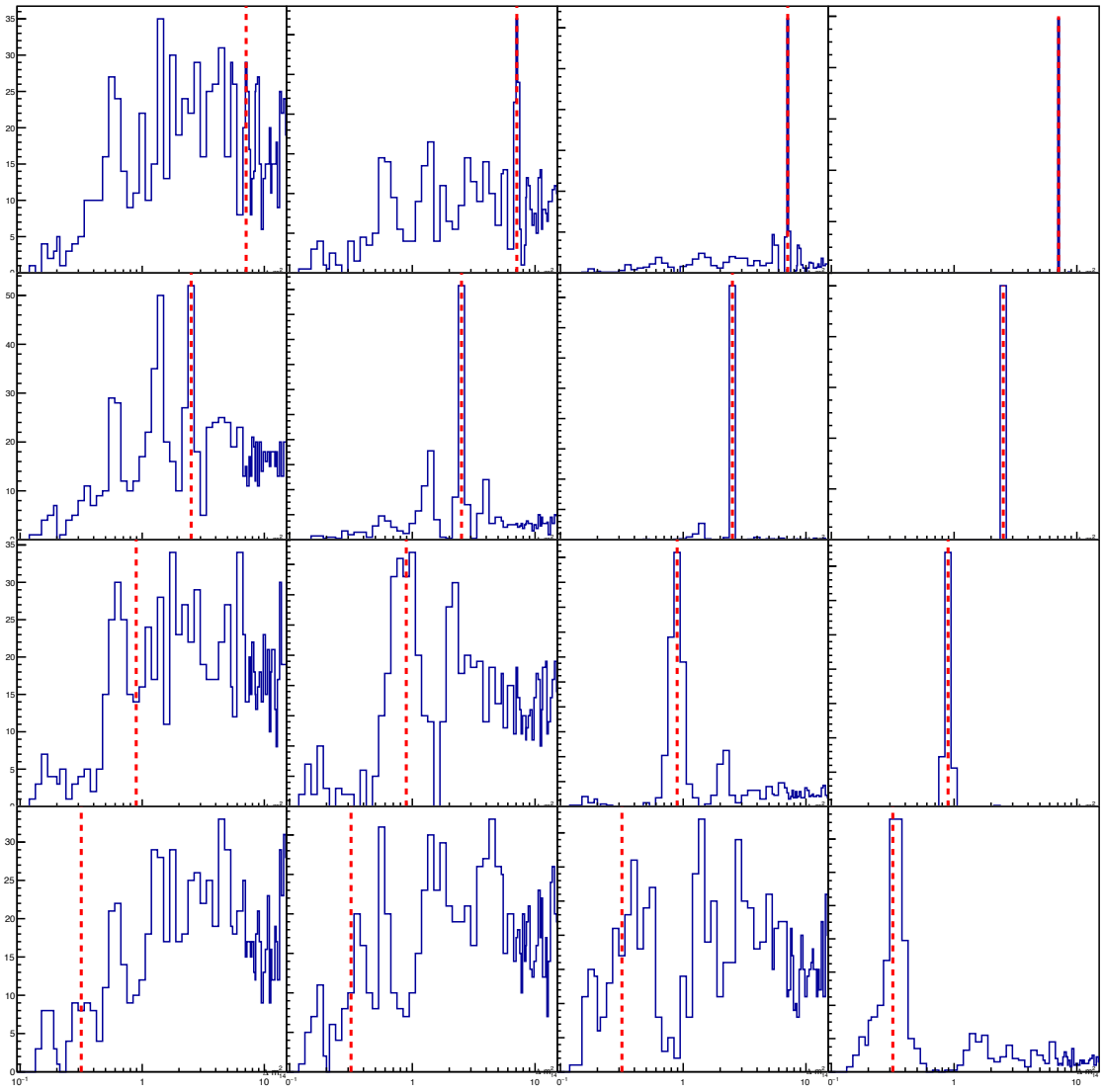

Figure 7.25. Best-fit $\sin^2 2\theta$ distribution for MC toys generated using 16 different input oscillation parameters. The agreement between input and the best-fit oscillation parameters as well as the width of the best-fit distribution is better for the points in the parameter space sensitive to the detector. In particular for the top two points on the right side, the oscillation frequencies and amplitudes are high enough that the ranges of best-fit Δm^2_{14} are smaller than the width of Δm^2_{14} bins.

The ability of the the fitter to reproduce the input oscillation parameters in presence of fluctuations was also tested. Oscillated MC toy datasets following Appendix. A.4 were generated by including fluctuations arising from statistical and systematic uncertainties. Because of the fluctuations, the fitter is not expected to reproduce the input parameters for all the toys but is expected to produce a distribution of best-fits values centered around the true oscillated parameters. Shown in Fig. 7.22 are the best-fit values for 1000 toys for the oscillation parameters corresponding to the RAA best-fit point. The best-fit points generated has median values of $\sin^2 2\theta$=0.159 and Δm^2_{14}=2.42 showing good agreement with the true oscillation parameters $\sin^2 2\theta$=0.165 and Δm^2_{14}=2.39. Shown in the Figs. 7.24, 7.25, 7.23 are the best-fit values for 1000 toys for the same values of oscillation parameters as used in the Fig. 7.21. The best-fit values were found to be in general agreement with the input oscillated parameters in the parameter space sensitive to the dataset. In all cases the toys were generated using the dataset size corresponding to 33 (28) reactor on (off) days. Systematic uncertainties quoted in Tab. 7.1 were used in generating the fluctuations in toys in addition to the fluctuations arising from the statistical uncertainties.

7.7 Results

Using the data and inputs as described in Sec. 7.3, χ^2 values for each ($\sin^2 2\theta$,Δm^2_{14}) grid points and null oscillation hypothesis were calculated as indicated by Eq. 7.1. The best-fit χ^2/NDF of 57.9/78 was found at ($\sin^2 2\theta$,Δm^2_{14}) (0.40, 0.50). In comparison the χ^2/NDF for 3ν oscillation case and RAA best-fit oscillation are found to be 61.9/80 and 68.7/78 respectively. By comparing the $\Delta\chi^2$ values of the data with the corresponding $\Delta\chi^2_C$ distribution, the p values were generated. Accordingly, $\Delta\chi^2_{\text{null}} - \chi^2_{\text{best-fit}} = 4$ is found to have a p value of 0.58 demonstrating that the PROSPECT data agrees well with the 3ν prediction. The $\Delta\chi^2_{\text{RAA}} - \chi^2_{\text{best-fit}} = 10.8$

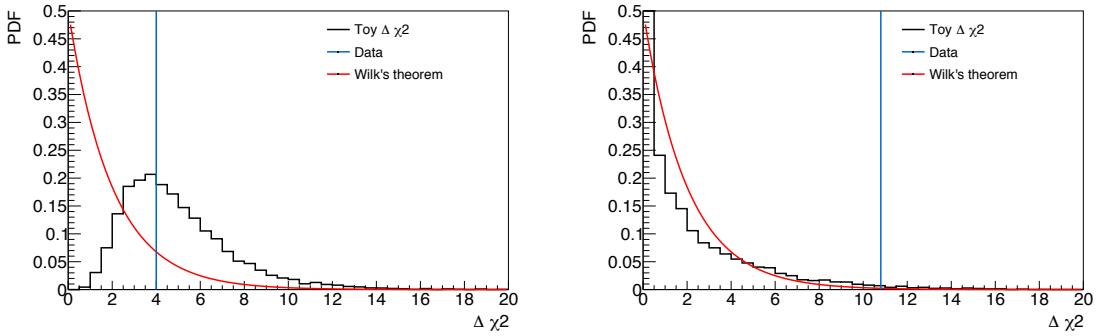

Figure 7.26. Toy χ^2 distribution generated using 10000 toys in null-oscillation (left) and RAA best-fit (right) oscillation cases. Also shown for comparison is the standard χ^2 under Wilk's theorem assumption. It could be seen that the null oscillation hypothesis would be erroneously rejected at better significance if the standard χ^2 distribution is assumed.

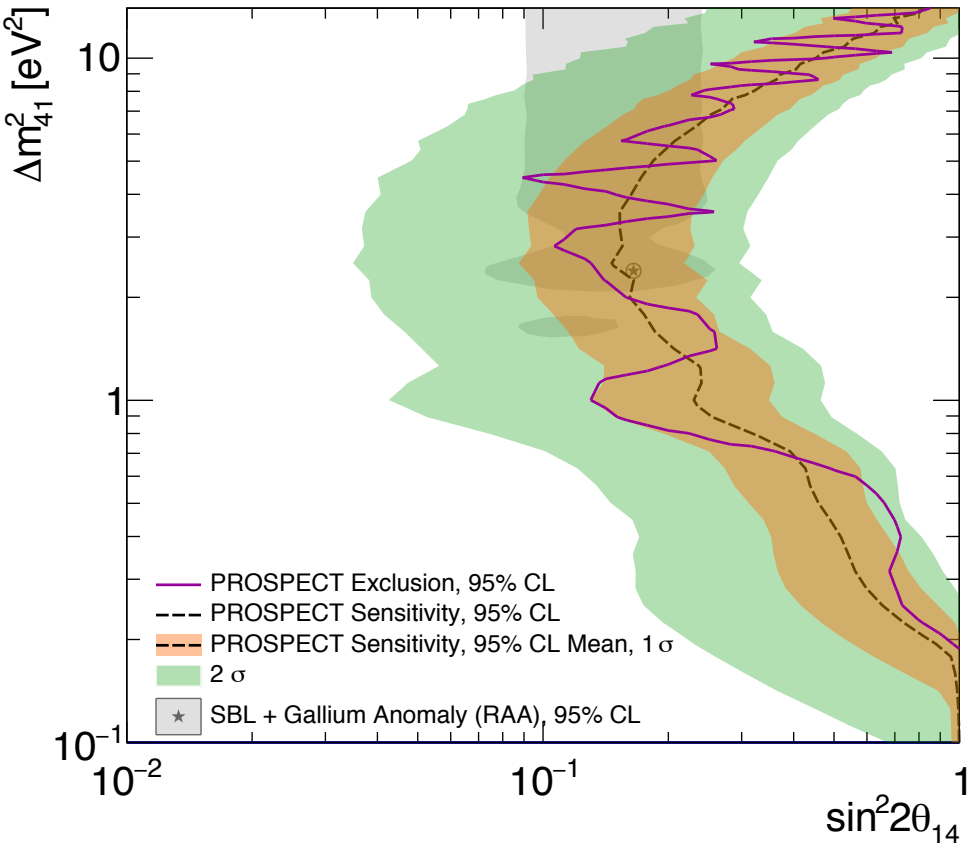

Figure 7.27. The Exclusion and sensitivity curves of the PROSPECT experiment as well as the 1σ and 2σ regions around the sensitivities. Sensitivity curve is the median of 10000 toys generated under no oscillation hypothesis. The 1σ and 2σ regions cover the 68.3% and 95.5% quantiles of toys around the median.

corresponds to a p value of 0.013 thus excluding the RAA best-fit point at 2.2σ. Toy $\Delta\chi^2$ distributions along with the $\Delta\chi^2_{\text{data}}$ values for the 3ν and the RAA best-fit oscillations are shown in the Fig. 7.26. Using the χ^2 values and the procedure defined in the Chapter. 7.5, the 95% CL exclusion curve was generated [2] as shown in the Fig. 7.27.

7.8 Cross-checks

The exclusion curve shown in Fig 7.27 was generated using full frequentist approach as described in Sec. 7.5. To verify the confidence intervals generated using the Feldman Cousins, another statistical approach called Gaussian CLs method [180][17] was used. Gaussian CLs method is a relatively simple and a computationally less intensive alternative to the Feldman Cousins approach. The same test statistic defined in Eq. 7.1 used for the Feldman Cousins approach was used for the Gaussian CLs approach. The exclusion curves generated using both methods agree well as shown in the Fig. 7.28.

One of the important claims of the PROSPECT experiment is the ability to perform search for sterile neutrinos without much dependence on the reactor $\overline{\nu}_e$ model. As mentioned in the Sec. 7.1, the predicted spectra for each baseline is obtained by scaling the measured detector-wide spectra to each baseline appropriately taking position and segment dependent effects into account. The segment and position-dependence was in effect provided by MC spectra as shown in the Eq. 7.1. These MC spectra were generated assuming Huber model for the reactor $\overline{\nu}_e$ spectrum. The reliance of the PROSPECT results on the reactor $\overline{\nu}_e$ models was checked by performing the full chain of analysis on Huber and Vogel models and comparing the results

[17]Gaussian CLs is a statistically appropriate method even when the conditions for the Wilk's theorem are not satisfied. It has the advantage that it is not as computationally intensive as the Feldman Cousins method but it can only be used when a signal is not discovered.

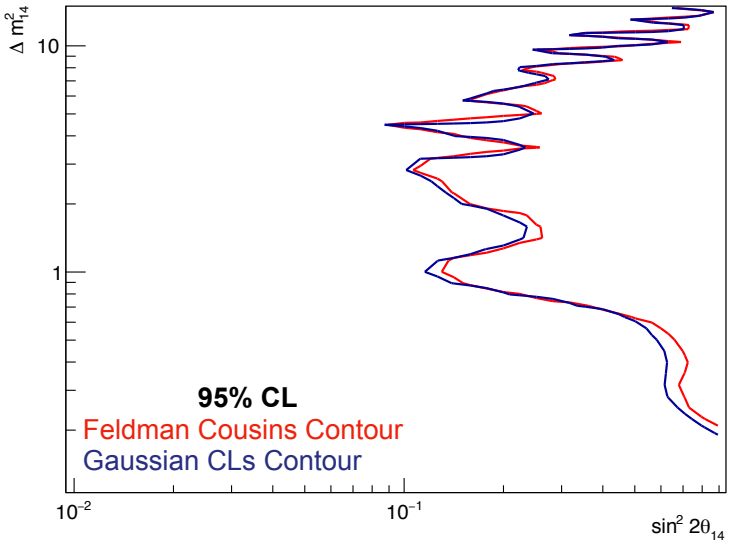

Figure 7.28. A comparison of exclusion curves generated using Feldman Cousins and Gaussian CLs method. The agreement is satisfactory and provides credence to the confidence levels generated using the Feldman Cousins method.

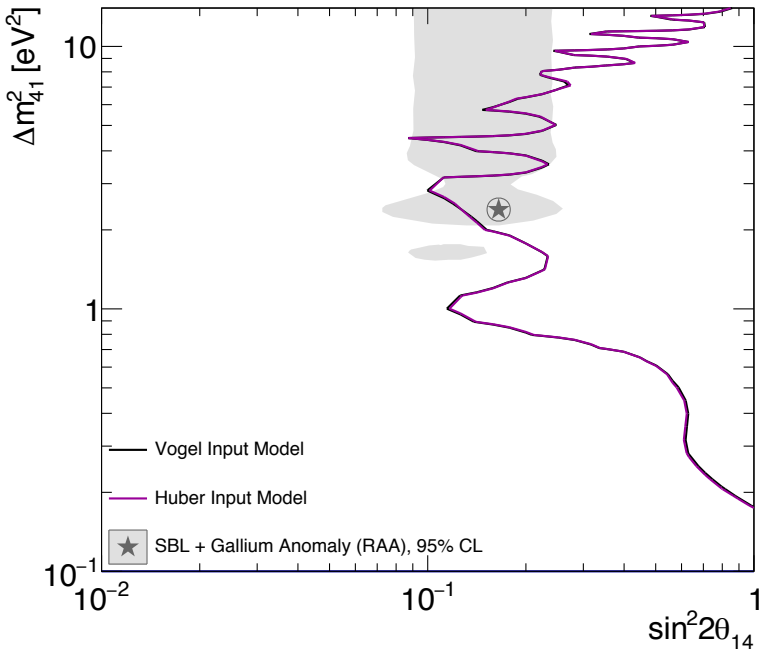

Figure 7.29. Comparison of exclusion curves generated using Vogel and Huber models. This shows the curves generated using Gaussian CLs method, but similar level of agreement was found when FC was used.

as shown in the Fig. 7.28. The impact of the reactor $\overline{\nu}_e$ model was minimum as evident from matching exclusion curves produced by the models. In addition, the best-fit point remained identical and the difference in χ^2_{min} between both cases was $\sim$0.2 showing that the reactor $\overline{\nu}_e$ model only has a small impact on the results.

7.9 Impact of Systematical Uncertainties

The impact of various systematics on the χ^2 values were checked by individually removing each covariance matrix and performing fits. The impact is shown as the difference in χ^2 from the nominal value. As expected, removing an uncertainty increased the χ^2_{min} value in all cases. Tab. 7.2 has a list of all systematic uncertainties and the resulting $\delta\chi^2$s and the best-fit values upon removal of the uncertainties. The biggest impact was found for the uncorrelated background peak non-uniformity, uncorrelated energy resolution, and the baseline shift uncertainties with a modest increase in χ^2 by 1.9, 1.0, and 1.0 respectively. All the other uncertainties contributed to under 1.0.

Table 7.2. Contribution of the systematic uncertainties to the χ^2 value. $\delta\chi^2_{min}$ corresponding to each uncertainty is the difference between the χ^2_{min} when using all the uncertainties and when that particular uncertainty is removed. Major variations were shown in bold for the baseline uncertainty, the background peak non-uniformity uncertainty, and the uncorrelated energy resolution. The best-fit point also remains relatively stable for all the uncertainties except for the uncorrelated energy scale.

Uncertainty Eliminated		$\delta\chi^2_{min}$	BF	
		-	Δm^2_{14}	$\sin^2 2\theta$
All uncertainties		-	***0.50***	***0.40***
No systematics (Only statistical uncertainties)		***6.0***	***0.50***	***0.35***
Correlated	Baseline shift	***1.0***	0.50	0.40
	Non-linearity	0.5	0.50	0.40
	Background normalization	0.3	0.50	0.40
	Correlation	0.2	0.50	0.40
	Background energy scale	0.2	0.50	0.40
	Al28 and Non-eq	0.2	0.50	0.40
	Energy loss	0.1	0.50	0.40
Uncorrelated	Background peak non-uniformity uncertainty	**1.9**	0.50	0.40
	Energy resolution	**1.0**	0.50	0.40
	Energy scale	0.5	**0.45**	0.40
	Efficiency	0.4	0.50	0.40
	Energy loss	0.4	0.50	0.40

CHAPTER 8

CONCLUSION

PROSPECT is a short-baseline reactor antineutrino experiment designed to search for sterile neutrinos and make a precise measurement of ^{235}U reactor antineutrino spectrum from the High Flux Isotope Reactor at Oak Ridge National Laboratory located in Tennessee. PROSPECT designed a detector with novel segmentation system to reach these goals. Several aspects of the detector design are novel or are improvements over the previous detectors with similar design. As part of the segmentation system the custom-built highly reflective optical separators and 3D printed support rods enabled PROSPECT to achieve low dead-volume and high dimensional uniformity. The PROSPECT segmentation system along with the double-ended readout have made 3D event reconstruction possible allowing for a reactor model independent oscillation search. PROSPECT also designed PSD capable ^{6}Li-loaded liquid scintillator with high light yield that enabled high resolution measurement of ^{235}U spectrum with high background reduction.

Using a segmented detector, PROSPECT performed an oscillation search with 33 days of data collected on surface close to a nuclear reactor. Employing a reactor model-independent fitter, the suggested best-fit was excluded at 2.2σ with this data. The close proximity of the detector to the HFIR reactor, the PROSPECT experiment is already able to provide the most competitive limits in the high Δm^2_{14} region. Shown in the Fig 8.1 is the PROSPECT exclusion curve in comparison with the exclusion curves generated by the other sterile neutrino searches using the reactor neutrinos as sources. Current PROSPECT sensitivity is limited by statistics. With additional data and improved statistics, most of the suggested parameter space will be covered by PROSPECT as shown in Fig. 8.1.

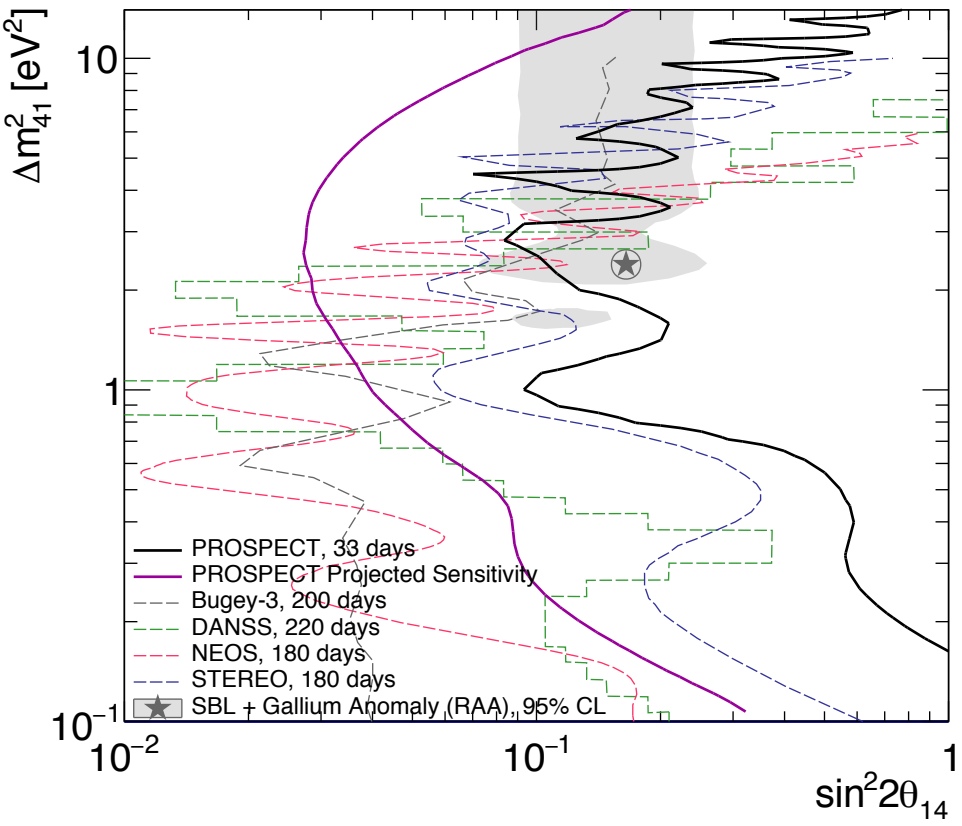

Figure 8.1. The exclusion curve of the PROSPECT experiment in comparison with the other reactor neutrino experiments [181–184] searching for sterile neutrinos. With only 33 days of reactor on data, PROSPECT experiment is already competitive with the other experiments at high oscillation frequencies that ran for much longer durations. Also shown is the PROSPECT sensitivity with 3 calendar years of PROSPECT data. PROSPECT experiment will have the best sensitivity of all the reactor experiments for high frequency oscillations.

PROSPECT is already able to make the most precise ^{235}U spectrum measurement [185] originating from a highly enriched Uranium reactor. The precision of the spectrum measurement will increase with more statistics and improved systematics. Finally, PROSPECT deployed an on-surface detector with almost no overburden and has observed neutrinos with a signal-to-background of 1:1 demonstrating the ability of on-surface detectors to observe neutrinos paving way for the use of neutrino detectors for non-proliferation purposes [186, 187].

APPENDIX A

STATISTICAL TECHNIQUES

In this appendix, statistical methods and the inputs used in performing the oscillation search are described.

A.1 Equivalence of the Pulls based χ^2 and the Covariance Matrix Based χ^2

In hypothesis testing and parameter estimation, typically constraints are set on the parameters of interest by forming confidence intervals. In defining confidence intervals, a function (test statistic) that depends on the parameters of interest and the observed dataset is defined. In the large statistics regime where the data could be approximated to a gaussian distribution, a commonly used test statistic for a collection of N variables is given by

$$\chi^2(\boldsymbol{\theta}) = \sum_{i=1}^{N} \frac{(o_i(\boldsymbol{\theta}) - e_i(\boldsymbol{\theta}) - \sum_{j=1}^{K} \alpha_j s_{ji}(\boldsymbol{\theta}))^2}{\sigma_i^2} + \sum_{j=1}^{K} \alpha_j^2. \tag{A.1}$$

where o_i and e_i are observed and expected counts for the i^{th} variable given parameters $\boldsymbol{\theta}$ with a statistical uncertainty of σ_i. K sources of systematic uncertainties are considered and the systematic uncertainty of j^{th} variable in i^{th} bins is given by s_{ji}. Statistical uncertainty could depend on $\boldsymbol{\theta}$ based on the way a test-statistic is defined [188, 189]. The nuisance parameter α_j could then be adjusted along with $\boldsymbol{\theta}$ to find the minimum value of $\chi^2(\boldsymbol{\theta})_{min}$. The best-fit parameter is thus defined as $\boldsymbol{\theta}_{\min} = \arg\min \chi^2(\boldsymbol{\theta})$.

Eq. A.1 could be represented in matrix form as

$$\begin{aligned} \chi^2 &= (\mathbf{u} - \mathbf{R}^{\mathrm{T}}\boldsymbol{\alpha})^{\mathrm{T}}(\mathbf{u} - \mathbf{R}^{\mathrm{T}}\boldsymbol{\alpha}) + \boldsymbol{\alpha}^{\mathrm{T}}\boldsymbol{\alpha} \\ &= \mathbf{u}^{\mathrm{T}}\mathbf{u} - 2\boldsymbol{\alpha}^{\mathrm{T}}\mathbf{R}\mathbf{u} + \boldsymbol{\alpha}^{\mathrm{T}}\mathbf{R}\mathbf{R}^{\mathrm{T}}\boldsymbol{\alpha} + \boldsymbol{\alpha}^{\mathrm{T}}\boldsymbol{\alpha}, \end{aligned} \tag{A.2}$$

where

$$\begin{aligned} u_i &\equiv \frac{o_i - e_i}{\sigma_i}, \\ R_{ji} &\equiv \frac{s_{ji}}{\sigma_i}, and \\ I_{ij} &\equiv \delta_{ij}. \end{aligned} \tag{A.3}$$

$\mathbf{I}$ is the identity matrix of rank N

The minimum values of the nuisance parameters could be found analytically by taking the derivative with respect to $\boldsymbol{\alpha}$ and setting it equal to zero.

$$\begin{aligned} \frac{\partial \chi^2}{\partial \boldsymbol{\alpha}} &= 0 \\ \therefore \mathbf{R}\mathbf{u} + \mathbf{R}\mathbf{R}^{\mathrm{T}}\boldsymbol{\alpha}_{\min} + \boldsymbol{\alpha}_{\min} &= 0. \end{aligned} \tag{A.4}$$

Multiplying Eq. A.4 on the left side with $\boldsymbol{\alpha}_{\min}$ gives

$$\boldsymbol{\alpha}_{\min}^{\mathrm{T}}\mathbf{R}\mathbf{u} + \boldsymbol{\alpha}_{\min}^{\mathrm{T}}\mathbf{R}\mathbf{R}^{\mathrm{T}}\boldsymbol{\alpha}_{\min} + \boldsymbol{\alpha}_{\min}^{\mathrm{T}}\boldsymbol{\alpha}_{\min} = 0. \tag{A.5}$$

Solving for $\boldsymbol{\alpha}_{\min}$ produces

$$\boldsymbol{\alpha}_{\min} = \mathbf{R}(\mathbf{R}^{\mathrm{T}}\mathbf{R} + \mathbf{I}_N)^{-1}\mathbf{u}. \tag{A.6}$$

Substituting A.4 in Eq. A.2 at $\boldsymbol{\alpha}_{\min}^{\mathrm{T}}$ produces

$$\chi^2_{\min} = \mathbf{u}^{\mathrm{T}}\mathbf{u} - \boldsymbol{\alpha}_{\min}^{\mathrm{T}}\mathbf{R}\mathbf{u}. \tag{A.7}$$

Substituting the value for $\boldsymbol{\alpha}_{\min}$ from Eq. A.6 in Eq. A.7 for $\chi^2_{\min}$ produces

$$\chi^2_{\min} = \mathbf{u}^{\mathrm{T}}(\mathbf{R}^{\mathrm{T}}\mathbf{R} + \mathbf{I}_N)^{-1}\mathbf{u}. \tag{A.8}$$

Separating the matrix $\mathbf{u}$ into two parts:

$$\Delta_i \equiv o_i - e_i \tag{A.9}$$

$$S_{ij} \equiv \sigma_i \delta_{ij}, \tag{A.10}$$

the Eq. A.1 can be written as

$$\chi^2_{\min} = \boldsymbol{\Delta}^{\mathrm{T}}(\mathbf{S}^{\mathrm{T}}(\mathbf{R}^{\mathrm{T}}\mathbf{R} + \mathbf{I}_N)\mathbf{S})^{-1}\boldsymbol{\Delta} \tag{A.11}$$

$$= \boldsymbol{\Delta}^{\mathrm{T}}\mathbf{V}^{-1}\boldsymbol{\Delta}. \tag{A.12}$$

where $\mathbf{V}$ is the covariance matrix defined by:

$$\mathbf{V}_{ij} = \sigma_i^2\delta_{ij} + \sum_l^K s_{li}s_{lj}. \tag{A.13}$$

A more detailed step-by-step derivation could be found in this the Ref. [190]. Using covariance matrix has the advantage that the correlations between all the bins are naturally included in the non-diagonal terms. Since covariance matrix implicitly includes variation over the systematics, fitting was not done explicitly over the nuisance parameters resulting in significant reduction in computation time.

A.2 Mapping Covariance Matrix from Segments to Baselines

The oscillation analysis is performed in energy and baseline bins as describes in the Sec. 7.1. The segment uncorrelated uncertainties have to be generated in segment basis and then transformed into baseline basis. The method to transform a segment based covariance matrix to a baseline based matrix is as follows.

Theorem 1. *Let* $\mathbf{X}$ *be a random vector of* N *elements with a covariance matrix* $\mathbf{V}(\mathbf{X})$*. Let* A *be a matrix that can act on* $\mathbf{X}$*. The covariance matrix of* $A\mathbf{X}$ *is*

$$\mathbf{V}(A\mathbf{X}) = A\ \boldsymbol{V}(\mathbf{X})\ A^T \tag{A.14}$$

The definition of a covariance matrix can be written in terms of the expectation of the set of variables $\mathbf{X}$:

$$\mathbf{V}(\mathbf{X}) = \mathrm{E}[(\mathbf{X} - \mathrm{E}[\mathbf{X}])(\mathbf{X} - \mathrm{E}[\mathbf{X}])^{\mathrm{T}}]. \tag{A.15}$$

The expectation operator is linear, such that, for a variable X and a constant a,

$$\mathrm{E}[aX] = a\mathrm{E}[X]. \tag{A.16}$$

Hence, the covariance matrix of $A\mathbf{X}$ can be derived as follows:

$$\mathbf{V}(A\mathbf{X}) = \mathrm{E}[(A\mathbf{X} - \mathrm{E}[A\mathbf{X}])(A\mathbf{X} - \mathrm{E}[A\mathbf{X}])^{\mathrm{T}}] \tag{A.17}$$

$$= \mathrm{E}[(A\mathbf{X} - A\mathrm{E}[\mathbf{X}])(A\mathbf{X} - A\mathrm{E}[\mathbf{X}])^{\mathrm{T}}] \tag{A.18}$$

$$= \mathrm{E}[A(\mathbf{X} - \mathrm{E}[\mathbf{X}])(A(\mathbf{X} - \mathrm{E}[\mathbf{X}]))^{\mathrm{T}}] \tag{A.19}$$

$$= \mathrm{E}[A(\mathbf{X} - \mathrm{E}[\mathbf{X}])(\mathbf{X} - \mathrm{E}[\mathbf{X}])^{\mathrm{T}} A^{\mathrm{T}}] \tag{A.20}$$

$$= A\ \mathrm{E}[(\mathbf{X} - \mathrm{E}[\mathbf{X}])(\mathbf{X} - \mathrm{E}[\mathbf{X}])^{\mathrm{T}}]\ A^{\mathrm{T}} \tag{A.21}$$

$$= A\ \mathbf{V}(\mathbf{X})\ A^{\mathrm{T}}. \tag{A.22}$$

For a given set of segments and baselines, the matrix A defines the mapping between the segments and baselines.

A.3 Statistical Covariance Matrices

Oscillation search was performed by comparing the scaled detector-wide spectrum to spectra for all the baselines. As discussed in Sec. 7.4.1, in addition to the observed spectra $O_{l,e}$, the predicted spectra $P_{l,e}$ also includes statistical fluctuations. Additionally, since $P_{l,e} = O_e \frac{M_{l,e}}{M_e} = (\sum_l O_{l,e}) \frac{M_{l,e}}{M_e}$, the terms $P_{l,e}$ and $O_{l,e}$ have correlations. The statistical covariance matrix has to include uncertainties and correlations that arise from defining $P_{l,e}$ using $O_{l,e}$.

For simplicity in deriving the covariance matrix terms, few terms are redefined as follows:

$$\begin{aligned} k = k_{l,e} &= \frac{M_{l,e}}{M_e} \\ X &= O_{l,e} \\ Y &= O_e \\ Z &= Y - X = O_e - O_{l,e}. \end{aligned} \tag{A.23}$$

$P_{l,e}$ can then be defined as

$$P_{l,e} = k \cdot Y \tag{A.24}$$

The first and the second moments for $X, Y,$ and Z are defined as $\mu_X, \mu_Y,$ and μ_Z and $\sigma_X^2, \sigma_Y^2,$ and σ_Z^2 respectively. From A.23, it can be seen that $\mu_Y = \mu_X + \mu_Z$.

Using the terms defined in Eq. A.23, A.24, the variance of the term $O_{l,e} - P_{l,e}$ is given by

$$\sigma^2(O_{l,e} - P_{l,e}) = \sigma^2(X - k \cdot Y) \tag{A.25}$$

Since the terms X and Y are correlated, Eq. A.25 can be defined as

$$\sigma^2(X - k_{l,e} \cdot Y) = \sigma^2(X) + k^2 \cdot \sigma^2(Y) - 2k \cdot \sigma(XY), \tag{A.26}$$

where $\sigma(XY)$ is the covariance between terms X and Y.

$$\begin{aligned} \sigma(XY) &= \mathrm{E}[XY] - \mathrm{E}[X]\mathrm{E}[Y] \\ &= \mathrm{E}[X(X+Z)] - \mu_X \cdot \mu_Y \\ &= \mathrm{E}[X^2 - X \cdot Z)] - \mu_X \cdot \mu_Y. \end{aligned} \tag{A.27}$$

Since X and Z are not correlated Eq.A.27 can be written as

$$\begin{aligned} \sigma(XY) &= \mathrm{E}[X^2] - \mathrm{E}[X] \cdot \mathrm{E}[Z] - \mu_X \cdot \mu_Y \\ &= \sigma^2 X + \mu_X^2 - \mu_X \cdot \mathrm{E}[Y - X] \cdot \mu_Y \\ &= \sigma^2 X + \mu_X^2 - \mu_X \cdot (\mu_Y - \mu_X) \cdot \mu_Y \\ &= \sigma^2 X + \mu_X^2 - \mu_X \cdot \mu_Y - \mu_X^2 \cdot \mu_Y \\ &= \sigma^2 X. \end{aligned} \tag{A.28}$$

Substituting $\sigma(XY)$ from Eq. A.28 in Eq. A.26 yields

$$\begin{aligned} \sigma^2(X - k_{l,e} \cdot Y) &= \sigma^2(X) + k^2 \cdot \sigma^2(Y) - 2k \cdot \sigma^2 X \\ &= \sigma^2(X) \cdot (1 - 2k) + k^2 \cdot \sigma^2(Y). \end{aligned} \tag{A.29}$$

Finally replacing the terms X, Y and with their original definitions yields the variance for l, e bin

$$\mathbf{V}_{\mathrm{l,e}} = \sigma^2(O_{l,e} - P_{l,e}) = \sigma^2(O_{l,e}) \cdot (1 - 2k) + k^2 \cdot \sigma^2(O_e). \tag{A.30}$$

This covariance matrix was only used during the fitting and omitted during toy generation.

A.4 Covariance Matrices and Toy Datasets

Covariance matrices for all the systematic matrices were generated using

$$\mathbf{V} = \mathrm{E}[(\mathbf{X} - \boldsymbol{\mu})(\mathbf{X} - \boldsymbol{\mu})^T] \tag{A.31}$$

where $\mathbf{X}$ is a toy vector generated using for a nominal distribution $\boldsymbol{\mu}$ and variations defined by the type of systematic under consideration.

Feldman Cousins method was used to generate the exclusion regions after performing fits. This method relies on generation of several MC toys for each oscillation parameter set. These MC toys should include fluctuations arising from the statistic and systematic uncertainties including correlations between bins. The fluctuations are generated using Cholesky decomposed covariance matrices. A MC toy with N bins is generated using

$$\mathbf{Y} = \boldsymbol{\mu} + \mathbf{L}\mathbf{z} \tag{A.32}$$

where $\boldsymbol{\mu}$ is an N element long vector containing the central values in each bin, $\mathbf{L}$ is a triangular matrix generated by Cholesky decomposing covariance matrix, $\mathbf{z}$ is an N element vector containing uncorrelated random values generated using a Gaussian distribtion $\mathcal{N}(0,1)$. $\mathbf{Y}$ is the generated MC toy that includes fluctuations originating from the covariance matrix $\mathbf{V}_{tot}$. The covariance matrix includes all statistical and systematic uncertainties discussed in Sec. 7.4 apart from the correlations arising from using the detector-wise spectrum to generate the predicted spectrum.

The generation of toys from covariance matrix is the reverse process of generating covariance matrix from toys [191, 192]. A positive definite symmetric matrix $\mathbf{V}$

can be Cholesky decomposed to produce a unique matrix $\mathbf{L}$.

$$\begin{aligned} \mathbf{V} &= \mathbf{L}\mathbf{L}^{\mathrm{T}} \\ &= \mathbf{L}\mathrm{E}[\mathbf{z}\mathbf{z}^{T}]\mathbf{L}^{\mathrm{T}}, \end{aligned} \tag{A.33}$$

where in the last equation since terms in $\mathbf{Z}$ are uncorrelated random variables, $\mathrm{E}[\mathbf{z}\mathbf{z}^{\mathrm{T}} = \mathbf{I}$. Since expectation is a linear operator

$$\begin{aligned} \mathbf{V} &= \mathrm{E}[\mathbf{L}\mathbf{z}\mathbf{z}^{\mathrm{T}}\mathbf{L}^{\mathrm{T}}] \\ &= \mathrm{E}[(\mathbf{L}\mathbf{z})(\mathbf{z}\mathbf{L})^{\mathrm{T}}]. \end{aligned} \tag{A.34}$$

This proves that the expectation value of $\mathbf{L}\mathbf{z}(\mathbf{z}\mathbf{L})^{\mathrm{T}}$ is the input covariance matrix. Recalling the definition of covariance matrix from Eq. A.31 that the Cholesky decomposition of a matrix produces unique result, Eq. A.34 proves that $\mathbf{L}\mathbf{z} = \mathbf{X} - \boldsymbol{\mu}$ proving that $\mathbf{Y}$ from Eq.A.32 is a toy containing all the fluctuations arising from the covariance matrix $\mathbf{V}$.

$$\mathbf{X} = \mathbf{Y} = \boldsymbol{\mu} + \mathbf{L}\mathbf{z}. \tag{A.35}$$

APPENDIX B

RATIONALE BEHIND USING FELDMAN COUSINS APPROACH

The standard (Wilks' theorem [193,194]) way of generating confidence region is by comparing the χ^2 generated using data with the standard χ^2 function. This is only valid under a specific set of conditions as described in detail in the articles [179, 180]. In case of search for sterile neutrino oscillations, the Wilks' theorem fails in several cases.

1. One condition needed for the Wilks' theorem is to have an open neighborhood around the true value of oscillations. This condition is not satisfied for the null oscillation and low oscillation amplitude cases since $\sin^2 2\theta < 0$ is invalid. This condition is well illustrated in the Ref. [180] in Figs.1 and 5.

2. Neutrino oscillations are sinusoidal in nature but Wilks' theorem assumes a gaussian probability distribution. For high frequency oscillations, the fits will have tendency to prefer local minima and hence Wilks' theorem breaks down. This can be seen in the Fig. 7.22 where some of the best-fits are concentrated around the points that produces local minima.

3. Additionally, for a binned analysis, Wilks' theorem breaks down in case of searches for sterile neutrinos at high Δm^2_{14} where the oscillation frequencies compete with the energy resolution of the detector.

Using the standard method would produce regions of overcoverage–assigning higher confidence than is true–or undercoverage–assigns lower confidence than is true–in several regions of the parameter space. To illustrate the point, the experiment's coverage was generated using the critical χ^2 maps 7.6 and is shown in Fig. B.1. It can be seen that most of the parameter space would be overcovered but a small region of parameter space would also be undercovered. The exclusion curve generated using both methods is shown in Fig. B.2. Since most of the exclusion curve is in the over-coverage region, the standard approach incorrectly provides better apparent coverage

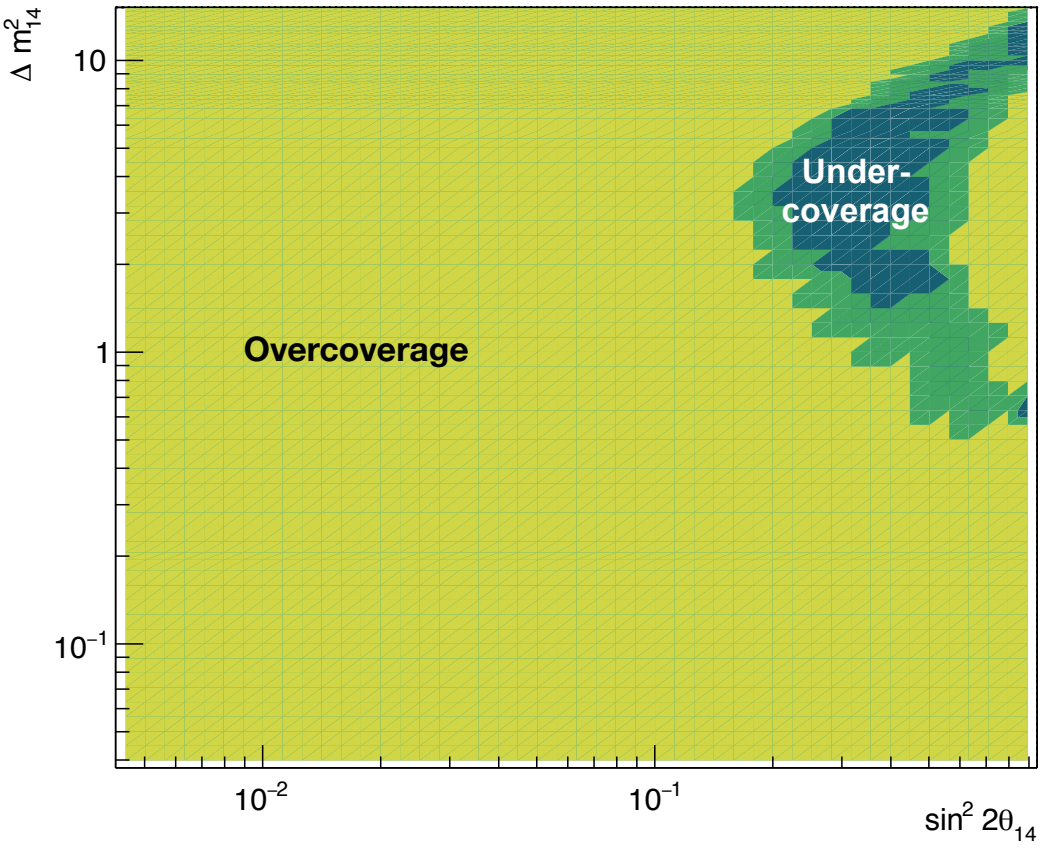

Figure B.1. Regions of significant overcoverage and undercoverage using the standard approach for the data set size and the uncertainties used in this analysis. The parameter space is dominated by overcoverage regions except for small regions in the high Δm^2_{14} and $\sin^2 2\theta$ values.

than the Feldman Cousins method. This shows the importance of assigning coverage based on using a statistically powerful technique like Feldman Cousins approach as opposed to the standard approach.

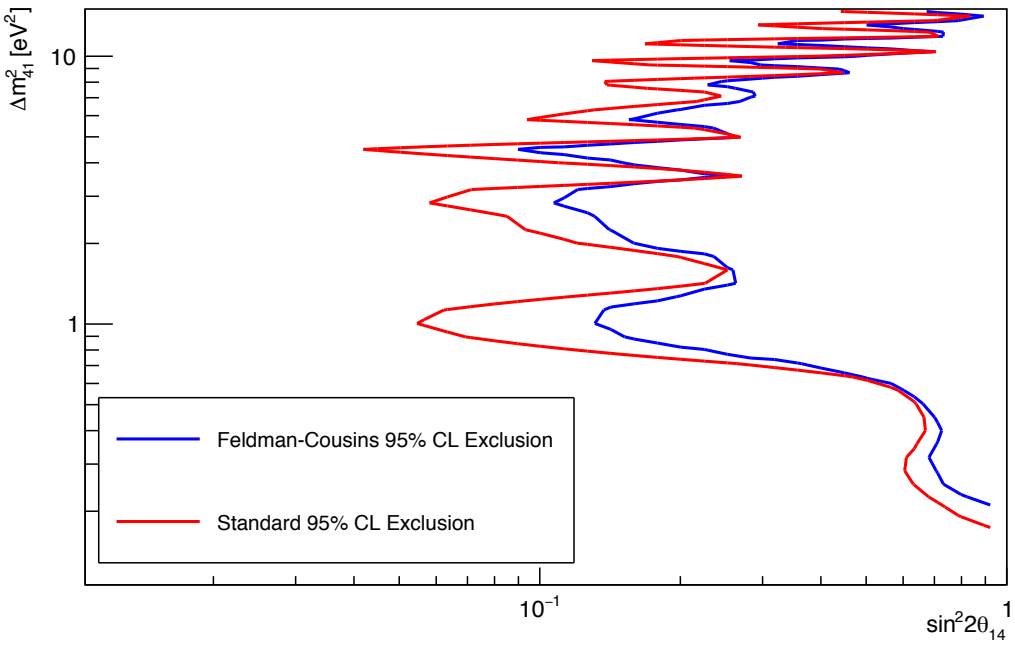

Figure B.2. A comparison between the exclusion curves generated using Feldman cousins approach and the standard approach. It can be seen that most of the parameter space will be overcovered if the standard method was used.

BIBLIOGRAPHY

[1] J. Ashenfelter *et al.*, *A Low Mass Optical Grid for the PROSPECT Reactor Antineutrino Detector* (2019)

[2] J. Ashenfelter *et al.*, *First search for short-baseline neutrino oscillations at HFIR with PROSPECT*, Phys. Rev. Lett. **121** (2018) (25), p. 251802

[3] J. Chadwick, *The intensity distribution in the magnetic spectrum of beta particles from radium (B+ C)*, Verh. Phys. Gesell. **16** (1914), pp. 383–391

[4] C. D. Ellis and W. A. Wooster, *The Average Energy of Disintegration of Radium E*, Proceedings of the Royal Society of London Series A **117** (1927), pp. 109–123

[5] L. Meitner and W. Orthmann, *Über eine absolute Bestimmung der Energie der primären β-Strahlen von Radium E*, Zeitschrift für Physik **60** (1930) (3-4), pp. 143–155

[6] F. Rasetti, *Alternating intensities in the spectrum of nitrogen*, Nature **124** (1929), pp. 792–793

[7] W. Pauli, *Letter to the physicists gathering at Tubingen. December 4, 1930, reprinted in Wolfgang Pauli, Collected scientific papers, edited by R*, Kronig and V. Weisskopf **2** (1930), p. 1313

[8] E. Fermi, *An attempt of a theory of beta radiation. 1.*, Z.Phys. **88** (1934), pp. 161–177

[9] F. Reines and C. Cowan, *The Reines-Cowan experiments: Detecting the Poltergeist*, Los Alamos Sci. **25** (1997), pp. 4–27

[10] F. Reines and C. L. Cowan, *The neutrino*, Nature **178** (1956) (4531), pp. 446–449

[11] R. Davis Jr, *Attempt to Detect the Antineutrinos from a Nuclear Reactor by the Cl 37 (ν^-, e-) A 37 Reaction*, Physical Review **97** (1955) (3), p. 766

[12] T. D. Lee and C. N. Yang, *Question of Parity Conservation in Weak Interactions*, Phys. Rev. **104** (1956), pp. 254–258,
URL: `https://link.aps.org/doi/10.1103/PhysRev.104.254`

[13] C. S. Wu, E. Ambler, R. W. Hayward, D. D. Hoppes and R. P. Hudson, *Experimental Test of Parity Conservation in Beta Decay*, Physical Review **105** (1957), pp. 1413–1415

[14] E. C. G. Sudarshan and R. E. Marshak, *Chirality Invariance and the Universal Fermi Interaction*, Phys. Rev. **109** (1958), pp. 1860–1862,
URL: `https://link.aps.org/doi/10.1103/PhysRev.109.1860.2`

[15] R. P. Feynman and M. Gell-Mann, *Theory of the Fermi Interaction*, Phys. Rev. **109** (1958), pp. 193–198,
URL: `https://link.aps.org/doi/10.1103/PhysRev.109.193`

[16] M. Goldhaber, L. Grodzins and A. W. Sunyar, *Helicity of Neutrinos*, Phys. Rev. **109** (1958), pp. 1015–1017,
URL: `https://link.aps.org/doi/10.1103/PhysRev.109.1015`

[17] G. Danby, J. Gaillard, K. Goulianos, L. Lederman, N. Mistry, M. Schwartz and J. Steinberger, *Observation of high-energy neutrino reactions and the existence of two kinds of neutrinos*, Physical Review Letters **9** (1962) (1), pp. 36–44

[18] J. N. Bahcall, *Solar neutrinos. i. theoretical*, Physical Review Letters **12** (1964) (11), pp. 300–302

[19] R. Davis Jr, D. S. Harmer and K. C. Hoffman, *Search for neutrinos from the sun*, Physical Review Letters **20** (1968) (21), p. 1205

[20] V. Gribov and B. Pontecorvo, *Neutrino astronomy and lepton charge*, Physics Letters B **28** (1969) (7), pp. 493–496

[21] Z. Maki, M. Nakagawa and S. Sakata, *Remarks on the unified model of elementary particles*, Progress of Theoretical Physics **28** (1962) (5), pp. 870–880

[22] F. Reines, H. Sobel and E. Pasierb, *Evidence for neutrino instability*, Physical Review Letters **45** (1980) (16), p. 1307

[23] J. Abdurashitov, E. Faizov, V. Gavrin, A. Gusev, A. Kalikhov, T. Knodel, I. Knyshenko, V. Kornoukhov, I. Mirmov, A. Pshukov *et al.*, *Results from SAGE (the Russian-American gallium solar neutrino experiment)*, Physics Letters B **328** (1994) (1), pp. 234–248

[24] W. Hampel, J. Handt, G. Heusser, J. Kiko, T. Kirsten, M. Laubenstein, E. Pernicka, W. Rau, M. Wojcik, Y. Zakharov *et al.*, *GALLEX solar neutrino observations: Results for GALLEX IV*, Physics Letters B **447** (1999) (1), pp. 127–133

[25] E. Bellotti, *First results from GNO*, Nuclear Physics B-Proceedings Supplements **91** (2001) (1), pp. 44–49

[26] M. Koshiba, *Kamioka Nucleon Decay Experiment: Kamiokande Collaboration*, in *Conf. Proc.* (1985), vol. 850418, pp. 65–88

[27] S. Hatakeyama *et al.*, *Measurement of the Flux and Zenith-Angle Distribution of Upward Through-Going Muons in Kamiokande I I+ I I I*, Physical Review Letters **81** (1998) (10), p. 2016

[28] Fukuda, Y and others, *Tau Neutrinos Favored over Sterile Neutrinos in Atmospheric Muon Neutrino Oscillations*, Physical Review Letters **85** (2000), pp. 3999–4003

[29] Q. Ahmad, R. Allen, T. Andersen, J. Anglin, J. Barton, E. Beier, M. Bercovitch, J. Bigu, S. Biller, R. Black *et al.*, *Direct evidence for neutrino flavor transformation from neutral-current interactions in the Sudbury Neutrino Observatory*, Physical Review Letters **89** (2002) (1), p. 011301

[30] K. Kodama *et al.*, *Observation of tau neutrino interactions*, Physics Letters B **504** (2001) (3), pp. 218–224

[31] J. B. Albert *et al.*, *Sensitivity and Discovery Potential of nEXO to Neutrinoless Double Beta Decay*, Phys. Rev. **C97** (2018) (6), p. 065503

[32] F. Monrabal *et al.*, *The Next White (NEW) Detector*, JINST **13** (2018) (12), p. P12010

[33] N. Abgrall *et al.*, *The Large Enriched Germanium Experiment for Neutrinoless Double Beta Decay (LEGEND)*, AIP Conf. Proc. **1894** (2017) (1), p. 020027

[34] A. Gando *et al.*, *Search for Majorana Neutrinos near the Inverted Mass Hierarchy Region with KamLAND-Zen*, Phys. Rev. Lett. **117** (2016) (8), p. 082503, [Addendum: Phys. Rev. Lett.117,no.10,109903(2016)]

[35] M. Agostini *et al.*, *Improved Limit on Neutrinoless Double-β Decay of ^{76}Ge from GERDA Phase II*, Phys. Rev. Lett. **120** (2018) (13), p. 132503

[36] C. Alduino *et al.*, *First Results from CUORE: A Search for Lepton Number Violation via $0\nu\beta\beta$ Decay of ^{130}Te*, Phys. Rev. Lett. **120** (2018) (13), p. 132501

[37] R. Acciarri *et al.*, *Long-baseline neutrino facility (LBNF) and deep underground neutrino experiment (DUNE) conceptual design report, volume 4 the DUNE detectors at LBNF*, arXiv preprint arXiv:1601.02984 (2016)

[38] K. Abe *et al.*, *Hyper-Kamiokande design report*, arXiv preprint arXiv:1805.04163 (2018)

[39] F. An *et al.*, *Neutrino physics with JUNO*, Journal of Physics G: Nuclear and Particle Physics **43** (2016) (3), p. 030401

[40] T. I.-P. Collaboration, *Letter of intent: the precision IceCube next generation upgrade (PINGU)*, arXiv preprint arXiv:1401.2046 (2014)

[41] S.-B. Kim, *New results from RENO and prospects with RENO-50*, Nuclear and Particle Physics Proceedings **265** (2015), pp. 93–98

[42] K. Abe *et al.*, *Measurement of Muon Antineutrino Oscillations with an Accelerator-Produced Off-Axis Beam*, Phys. Rev. Lett. **116** (2016), p. 181801, URL: `https://link.aps.org/doi/10.1103/PhysRevLett.116.181801`

[43] M. A. Acero *et al.*, *New constraints on oscillation parameters from ν_e appearance and ν_μ disappearance in the NOvA experiment*, Phys. Rev. **D98** (2018), p. 032012

[44] A. A. Esfahani *et al.*, *Determining the neutrino mass with cyclotron radiation emission spectroscopy—Project 8*, Journal of Physics G: Nuclear and Particle Physics **44** (2017) (5), p. 054004

[45] J. Wolf, K. Collaboration *et al.*, *The KATRIN neutrino mass experiment*, Nuclear Instruments and Methods in Physics Research Section A: Accelerators, Spectrometers, Detectors and Associated Equipment **623** (2010) (1), pp. 442–444

[46] M. Tanabashi *et al.*, *Review of Particle Physics*, Phys. Rev. D **98** (2018), p. 030001,
URL: `https://link.aps.org/doi/10.1103/PhysRevD.98.030001`

[47] C. Giunti and C. W. Kim, *Fundamentals of neutrino physics and astrophysics* (Oxford university press, 2007)

[48] R. Foot, H. Lew, X.-G. He and G. C. Joshi, *See-saw neutrino masses induced by a triplet of leptons*, Zeitschrift für Physik C Particles and Fields **44** (1989) (3), pp. 441–444

[49] K. N. Abazajian *et al.*, *Light sterile neutrinos: a white paper*, arXiv preprint arXiv:1204.5379 (2012)

[50] S. Gariazzo, C. Giunti, M. Laveder, Y. Li and E. Zavanin, *Light sterile neutrinos*, Journal of Physics G: Nuclear and Particle Physics **43** (2016) (3), p. 033001

[51] F. Reines, *The Early Days of Experimental Neutrino Physics*, Science **203** (1979) (4375), pp. 11–16,
URL: http://science.sciencemag.org/content/203/4375/11

[52] R. E. Carter, F. Reines, J. J. Wagner and M. E. Wyman, *Free Antineutrino Absorption Cross Section. II. Expected Cross Section from Measurements of Fission Fragment Electron Spectrum*, Phys. Rev. **113** (1959), pp. 280–286,
URL: https://link.aps.org/doi/10.1103/PhysRev.113.280

[53] F. Reines, H. S. Gurr and H. W. Sobel, *Detection of $\overline{\nu}_e - e$ Scattering*, Phys. Rev. Lett. **37** (1976), pp. 315–318,
URL: https://link.aps.org/doi/10.1103/PhysRevLett.37.315

[54] A. Vershinksii, A. Meluzov, L. Mikaelyan, S. Nikolaev, M. Skorokhvatov and A. Etenko, *Observation of the interaction of reactor antineutrinos with deuterons in neutral and charged current channels at the Rovno nuclear power station*, JETP LETTERS **51** (1990) (2), pp. 94–98

[55] A. Afonin, S. Ketov, V. Kopeikin, L. Mikaelyan, M. Skorokhvatov and S. Tolokonnikov, *A study of the reaction v e+ P→ e++ n on a nuclear reactor*, Soviet Physics-JETP (English Translation) **67** (1988) (2), pp. 213–221

[56] A. Afonin, A. Borovoi, Y. L. Dobrynin, S. Ketov, V. Kopeikin, L. Mikaélyan, M. Skorokhvatov, S. Tolokonnikov and A. Kheruvtsmov, *Neutrino experiment in the reactor of the Rovno atomic power plant: cross section for inverse ß decay*, measurements **15** (1984), p. 14X103

[57] G. Vidyakin, V. Vyrodov, Y. V. Kozlov, A. Martem'yanov, V. Martem'yanov, A. Odinokov, S. Śukhotin, V. Tarasenkov, E. Turbin, S. Tyurenkov *et al.*, *Limitations on the characteristics of neutrino oscillations*, JETP Letters **59** (1994) (6), pp. 390–393

[58] F. Reines, *Do neutrinos oscillate?*, Nuclear Physics A **396** (1983), pp. 469 – 478

[59] H. Kwon, F. Boehm, A. A. Hahn, H. E. Henrikson, J. L. Vuilleumier, J. F. Cavaignac, D. H. Koang, B. Vignon, F. v. Feilitzsch and R. L. Mössbauer, *Search for neutrino oscillations at a fission reactor*, Phys. Rev. D **24** (1981), pp. 1097–1111,
URL: http://link.aps.org/doi/10.1103/PhysRevD.24.1097

[60] F. von Feilitzsch, A. Hahn and K. Schreckenbach, *Experimental beta-spectra from 239Pu and 235U thermal neutron fission products and their correlated antineutrino spectra*, Physics Letters B **118** (1982) (1), pp. 162 – 166,
URL: http://www.sciencedirect.com/science/article/pii/0370269382906220

[61] A. Hahn, K. Schreckenbach, W. Gelletly, F. von Feilitzsch, G. Colvin and B. Krusche, *Antineutrino spectra from 241Pu and 239Pu thermal neutron fission products*, Physics Letters B **218** (1989) (3), pp. 365 – 368, URL: http://www.sciencedirect.com/science/article/pii/0370269389915980

[62] K. Schreckenbach, G. Colvin, W. Gelletly and F. V. Feilitzsch, *Determination of the antineutrino spectrum from 235U thermal neutron fission products up to 9.5 MeV*, Physics Letters B **160** (1985) (4), pp. 325 – 330, URL: http://www.sciencedirect.com/science/article/pii/0370269385913371

[63] J. Cavaignac, A. Hoummada, D. Koang, B. Vignon, Y. Declais, H. De Kerret, H. Pessard and J. Thenard, *Indication for neutrino oscillation from a high statistics experiment at the bugey reactor*, Physics Letters B **148** (1984) (4-5), pp. 387–394

[64] Y. Declais *et al.*, *Study of reactor anti-neutrino interaction with proton at Bugey nuclear power plant*, Phys. Lett. **B338** (1994), pp. 383–389

[65] B. Achkar *et al.*, *Search for neutrino oscillations at 15, 40 and 95 meters from a nuclear power reactor at Bugey*, Nuclear Physics B **434** (1995) (3), pp. 503–532

[66] B. Achkar, R. Aleksan, M. Avenier, G. Bagieu, J. Bouchez, R. Brissot, J. Cavaignac, J. Collot, M. Cousinou, J.-P. Cussonneau *et al.*, *Comparison of anti-neutrino reactor spectrum models with the Bugey 3 measurements*, Physics Letters B **374** (1996) (1-3), pp. 243–248

[67] A. Afonin *et al.*, *Search for neutrino oscillations in an experiment in the reactor of the Rovno nuclear power plant*, Jetp Lett **42** (1985) (5), p. 285

[68] G. Vidyakin, V. Vyrodov, I. Gurevich, Y. V. Kozlov, V. Martemyanov, S. Sukhotin, V. Tarasenkov and S. K. Khakimov, *Detection of anti-neutrinos in the flux from two reactors*, Sov. Phys. JETP **66** (1987), p. 243

[69] M. Apollonio *et al.*, *Limits on neutrino oscillations from the CHOOZ experiment*, Physics Letters B **466** (1999) (2), pp. 415–430

[70] F. Boehm *et al.*, *The Palo Verde reactor neutrino oscillation experiment*, Nuclear Physics B-Proceedings Supplements **77** (1999) (1), pp. 166–170

[71] T. Araki *et al.*, *Measurement of neutrino oscillation with KamLAND: Evidence of spectral distortion*, Physical Review Letters **94** (2005) (8), p. 081801

[72] K. Abe *et al.*, *Indication of electron neutrino appearance from an accelerator-produced off-axis muon neutrino beam*, Physical Review Letters **107** (2011) (4), p. 041801

[73] P. Adamson *et al.*, *Improved Search for Muon-Neutrino to Electron-Neutrino Oscillations in MINOS*, Phys. Rev. Lett. **107** (2011), p. 181802, URL: http://link.aps.org/doi/10.1103/PhysRevLett.107.181802

[74] Y. Abe *et al.*, *Indication of Reactor $\overline{\nu}_e$ Disappearance in the Double Chooz Experiment*, Phys. Rev. Lett. **108** (2012), p. 131801, URL: http://link.aps.org/doi/10.1103/PhysRevLett.108.131801

[75] D. Adey *et al.*, *Improved Measurement of the Reactor Antineutrino Flux at Daya Bay* (2018)

[76] U. of Texas Austin, *Nuclear fission of ^{235}U*, University of Texas Austin, URL: https://ph.utexas.edu

[77] A. Strumia and F. Vissani, *Precise quasielastic neutrino/nucleon cross-section*, Physics Letters B **564** (2003) (1), pp. 42 – 54, URL: http://www.sciencedirect.com/science/article/pii/S0370269303006166

[78] A. C. Hayes and P. Vogel, *Reactor neutrino spectra*, Annual Review of Nuclear and Particle Science **66** (2016), pp. 219–244

[79] V. Kopeikin, L. Mikaelyan and V. Sinev, *Reactor as a source of antineutrinos: Thermal fission energy*, Physics of Atomic Nuclei **67** (2004) (10), pp. 1892–1899

[80] A. Hayes, J. Friar, G. Garvey, G. Jungman and G. Jonkmans, *Systematic Uncertainties in the Analysis of the Reactor Neutrino Anomaly*, Phys.Rev.Lett. **112** (2014), p. 202501

[81] M. Kellett, O. Bersillon and R. Mills, *The JEFF-3.1/-3.1. 1 radioactive decay data and fission yields sub-libraies Tech*, Rep. JEFF Report **20** (2009)

[82] M. Chadwick *et al.*, *ENDF/B-VII.1 Nuclear Data for Science and Technology: Cross Sections, Covariances, Fission Product Yields and Decay Data*, Nuclear Data Sheets **112** (2011) (12), pp. 2887 – 2996, URL: http://www.sciencedirect.com/science/article/pii/S009037521100113X, special Issue on ENDF/B-VII.1 Library

[83] A. A. Sonzogni, T. D. Johnson and E. A. McCutchan, *Nuclear structure insights into reactor antineutrino spectra*, Phys. Rev. C **91** (2015), p. 011301, URL: https://link.aps.org/doi/10.1103/PhysRevC.91.011301

[84] A. Dwyer, D. and J. Langford, T. *Spectral Structure of Electron Antineutrinos from Nuclear Reactors*, Phys. Rev. Lett. **114** (2015), p. 012502, URL: http://link.aps.org/doi/10.1103/PhysRevLett.114.012502

[85] A. A. Sonzogni, E. A. McCutchan, T. D. Johnson and P. Dimitriou, *Effects of Fission Yield Data in the Calculation of Antineutrino Spectra for* $^{235}\mathrm{U}(n, \mathit{fission})$ *at Thermal and Fast Neutron Energies*, Phys. Rev. Lett. **116** (2016), p. 132502, URL: https://link.aps.org/doi/10.1103/PhysRevLett.116.132502

[86] A. A. Sonzogni, M. Nino and E. A. McCutchan, *Revealing Fine Structure in the Antineutrino Spectra From a Nuclear Reactor*, Phys. Rev. **C98** (2018) (1), p. 014323

[87] K. Schreckenbach, H. R. Faust, F. von Feilitzsch, A. A. Hahn, K. Hawerkamp and J. L. Vuilleumier, *Absolute measurement of the beta spectrum from 235 U fission as a basis for reactor antineutrino experiments*, Phys. Lett. **99B** (1981), pp. 251–256

[88] P. Huber, *Determination of antineutrino spectra from nuclear reactors*, Phys. Rev. C **84** (2011), p. 024617, URL: http://link.aps.org/doi/10.1103/PhysRevC.84.024617

[89] P. Vogel and J. F. Beacom, *Angular distribution of neutron inverse beta decay, $\overline{\nu}_e + p \rightarrow e^+ + n$*, Physical Review D **60** (1999) (5), p. 053003

[90] G. R. Jocher, D. A. Bondy, B. M. Dobbs, S. T. Dye, J. A. G. III, J. G. Learned, C. L. Mulliss and S. Usman, *Theoretical antineutrino detection, direction and ranging at long distances*, Physics Reports **527** (2013) (3), pp. 131 – 204, URL: http://www.sciencedirect.com/science/article/pii/S0370157313000240, theoretical Antineutrino Detection, Direction and Ranging at Long Distances

[91] C. O. Muehlhause and S. Oleksa, *Antineutrino Flux from a Reactor*, Phys. Rev. **105** (1957), pp. 1332–1334, URL: https://link.aps.org/doi/10.1103/PhysRev.105.1332

[92] R. W. King and J. F. Perkins, *Inverse Beta Decay and the Two-Component Neutrino*, Phys. Rev. **112** (1958), pp. 963–966, URL: https://link.aps.org/doi/10.1103/PhysRev.112.963

[93] F. T. Avignone, *$V-A$ Elastic Scattering of Electrons by Fission Antineutrinos*, Phys. Rev. D **2** (1970), pp. 2609–2612, URL: https://link.aps.org/doi/10.1103/PhysRevD.2.2609

[94] B. R. Davis, P. Vogel, F. M. Mann and R. E. Schenter, *Reactor antineutrino spectra and their application to antineutrino-induced reactions*, Phys. Rev. C **19** (1979), pp. 2259–2266, URL: https://link.aps.org/doi/10.1103/PhysRevC.19.2259

[95] H. Klapdor and J. Metzinger, *Calculation of the antineutrino spectrum from thermal fission of 235U*, Physics Letters B **112** (1982) (1), pp. 22–26

[96] F. Avignone III and Z. Greenwood, *Calculated spectra of antineutrinos from the fission products of U 235, U 238, and Pu 239, and antineutrino-induced reactions*, Physical Review C **22** (1980) (2), p. 594

[97] N. Haag, W. Gelletly, F. von Feilitzsch, L. Oberauer, W. Potzel, K. Schreckenbach and A. A. Sonzogni, *Re-publication of the data from the BILL magnetic spectrometer: The cumulative β spectra of the fission products of ^{235}U, ^{239}Pu, and ^{241}Pu*, arXiv e-prints (2014)

[98] N. Haag, A. Gütlein, M. Hofmann, L. Oberauer, W. Potzel, K. Schreckenbach and F. M. Wagner, *Experimental Determination of the Antineutrino Spectrum of the Fission Products of ^{238}U*, Phys. Rev. Lett. **112** (2014), p. 122501, URL: https://link.aps.org/doi/10.1103/PhysRevLett.112.122501

[99] T. A. Mueller *et al.*, *Improved Predictions of Reactor Antineutrino Spectra*, Phys. Rev. **C83** (2011), p. 054615

[100] G. Mention, M. Fechner, T. Lasserre, T. A. Mueller, D. Lhuillier, M. Cribier and A. Letourneau, *Reactor antineutrino anomaly*, Physical Review D **83** (2011) (7), p. 073006

[101] F. P. An *et al.*, *Measurement of the Reactor Antineutrino Flux and Spectrum at Daya Bay*, Phys. Rev. Lett. **116** (2016) (6), p. 061801, [Erratum: Phys. Rev. Lett.118,no.9,099902(2017)]

[102] Y. Abe *et al.*, *Measurement of θ_{13} in Double Chooz using neutron captures on hydrogen with novel background rejection techniques*, JHEP **01** (2016), p. 163

[103] G. Bak *et al.*, *Fuel-composition dependent reactor antineutrino yield and spectrum at RENO* (2018)

[104] F. P. An *et al.*, *Improved Measurement of the Reactor Antineutrino Flux and Spectrum at Daya Bay*, Chin. Phys. **C41** (2017) (1), p. 013002

[105] A. C. Hayes, E. A. McCutchan and A. A. Sonzogni, Phys. Rev. Lett. **119** (2017), p. 112501

[106] A. C. Hayes, J. L. Friar, G. T. Garvey, D. Ibeling, G. Jungman, T. Kawano and R. W. Mills, *Possible origins and implications of the shoulder in reactor neutrino spectra*, Phys. Rev. D **92** (2015), p. 033015,
URL: https://link.aps.org/doi/10.1103/PhysRevD.92.033015

[107] X. Wang, J. Friar and A. Hayes, Phys. Rev. C (2016), p. 034314

[108] Y. Gebre, B. R. Littlejohn and P. T. Surukuchi, *Prospects for improved understanding of isotopic reactor antineutrino fluxes*, Phys. Rev. D **97** (2018), p. 013003,
URL: https://link.aps.org/doi/10.1103/PhysRevD.97.013003

[109] A. Onillon, *Updated Flux and Spectral Predictions relevant to the RAA*, Applied Antineutrino Physics Workshop (AAP) 2018 (2018),
URL: https://neutrinos.llnl.gov/content/assets/docs/workshops/2018/AAP2018-ILL-spectra-normalization-Onillon.pdf

[110] C. Giunti, Y. F. Li, B. R. Littlejohn and P. T. Surukuchi, *Diagnosing the reactor antineutrino anomaly with global antineutrino flux data*, Phys. Rev. D **99** (2019), p. 073005,
URL: https://link.aps.org/doi/10.1103/PhysRevD.99.073005

[111] C. Giunti, *Precise determination of the ^{235}U reactor antineutrino cross section per fission*, Phys. Lett. B **764** (2017), pp. 145–149

[112] G. Mention, M. Fechner, T. Lasserre, T. A. Mueller, D. Lhuillier, M. Cribier and A. Letourneau, *The Reactor Antineutrino Anomaly*, Phys. Rev. **D83** (2011), p. 073006

[113] K. N. Abazajian *et al.*, *Light Sterile Neutrinos: A White Paper* (2012)

[114] F. P. An *et al.*, Phys. Rev. Lett. **118** (2017), p. 251801

[115] F. P. An *et al.*, *Improved measurement of the reactor antineutrino flux and spectrum at Daya Bay*, Chinese Physics C **41** (2017) (1), p. 013002,
URL: https://doi.org/10.1088%2F1674-1137%2F41%2F1%2F013002

[116] T. Abrahão, T. Bezerra, A. Onillon and S. W. and, *Reactor spectral rate and shape measurement in Double Chooz detectors*, Journal of Physics: Conference Series **888** (2017), p. 012134,
URL: https://doi.org/10.1088%2F1742-6596%2F888%2F1%2F012134

[117] J. Choi, W. Choi, Y. Choi, H. Jang, J. Jang, E. Jeon, K. Joo, B. Kim, H. Kim, J. Kim *et al.*, *Observation of energy and baseline dependent reactor antineutrino disappearance in the RENO experiment*, Physical review letters **116** (2016) (21), p. 211801

[118] V. Zacek, G. Zacek, P. Vogel and J.-L. Vuilleumier, *Evidence for a 5 MeV Spectral Deviation in the Goesgen Reactor Neutrino Oscillation Experiment*, arXiv preprint arXiv:1807.01810 (2018)

[119] C. Buck, A. P. Collin, J. Haser and M. Lindner, *Investigating the spectral anomaly with different reactor antineutrino experiments*, Physics Letters B **765** (2017), pp. 159–162

[120] A. Aguilar, L. Auerbach, R. Burman, D. Caldwell, E. Church, A. Cochran, J. Donahue, A. Fazely, G. Garvey, R. Gunasingha *et al.*, *Evidence for neutrino oscillations from the observation of ν^- e appearance in a ν^- μ beam*, Physical Review D **64** (2001) (11), p. 112007

[121] A. Aguilar-Arevalo *et al.*, *Search for Electron Neutrino Appearance at the Δ m 2 1 eV 2 Scale*, Physical review letters **98** (2007) (23), p. 231801

[122] G. Ilas *et al.*, *Modeling and Simulations for the High Flux Isotope Reactor Cycle 400* (2015),
URL: `https://info.ornl.gov/sites/publications/Files/Pub54181.pdf`

[123] A. Conant, *Reactor Modeling Uncertainties for Antineutrino Detection at HFIR using the PROSPECT Experiment.*, MARC XI (2018),
URL: `https://prospect.yale.edu/sites/default/files/files/Conant_MARCXI_Poster_v5.pdf`

[124] High Flux Isotope Reactor, `https://neutrons.ornl.gov/hfir/parameters`

[125] J. Ashenfelter *et al.*, *Background Radiation Measurements at High Power Research Reactors*, Nucl. Instrum. Meth. **A806** (2016), pp. 401–419

[126] K. Heeger, M. Tobin, B. Littlejohn and H. Mumm, *Experimental parameters for a reactor antineutrino experiment at very short baselines*, Physical Review D **87** (2013) (7), p. 073008

[127] Eljen Technologies, `https://eljentechnology.com/products/liquid-scintillators/ej-301-ej-309`, accessed: 2018-09-11

[128] J. Ashenfelter *et al.*, *The PROSPECT Reactor Antineutrino Experiment*, arXiv (2018)

[129] CAEN V1725 Waveform Digitizer, `https://www.caen.it/products/v1725`, accessed: 2019-01-09

[130] Wiener MPOD high voltage crate and controller, `http://www.wiener-d.com/sc/powered-crates/vme/9u-vme-6023.html`, accessed: 2019-01-09

[131] J. Ashenfelter *et al.*, *Lithium-loaded liquid scintillator production for the PROSPECT experiment*, Journal of Instrumentation **14** (2019) (03), pp. P03026–P03026,
URL: `https://doi.org/10.1088%2F1748-0221%2F14%2F03%2Fp03026`

[132] D. Norcini, *Development of PROSPECT detectors for precision antineutrino studies*, in *Proceedings, Meeting of the APS Division of Particles and Fields (DPF 2015): Ann Arbor, Michigan, USA, 4-8 Aug 2015* (2015)

[133] J. Ashenfelter *et al.*, *The PROSPECT physics program*, Journal of Physics G: Nuclear and Particle Physics **43** (2016) (11), p. 113001, URL: http://stacks.iop.org/0954-3899/43/i=11/a=113001

[134] J. Ashenfelter *et al.*, *Light collection and pulse-shape discrimination in elongated scintillator cells for the PROSPECT reactor antineutrino experiment*, Journal of Instrumentation **10** (2015) (11), p. P11004, URL: http://stacks.iop.org/1748-0221/10/i=11/a=P11004

[135] J. Ashenfelter *et al.*, *Performance of a segmented 6 Li-loaded liquid scintillator detector for the PROSPECT experiment*, Journal of Instrumentation **13** (2018) (06), p. P06023, URL: http://stacks.iop.org/1748-0221/13/i=06/a=P06023

[136] P. T. Surukuchi, *Design of the PROSPECT Experiment*, PoS **ICHEP2016** (2016), p. 938

[137] 3M DF2000MA, https://multimedia.3m.com/mws/media/982449O/3mtm-specular-film-df2000ma-technical-data-sheet.pdf

[138] ACP Composites, https://www.acpsales.com/home.html, accessed: 2018-09-11

[139] Enhanced Specular Reflector, https://www.3m.com/3M/en_US/company-us/all-3m-products/~/3M-Enhanced-Specular-Reflector-3M-ESR-/?N=5002385+3293061534&rt=rud

[140] J. Cao and K.-B. Luk, *An overview of the Daya Bay reactor neutrino experiment*, Nuclear Physics B **908** (2016), pp. 62 – 73, URL: http://www.sciencedirect.com/science/article/pii/S0550321316300724, neutrino Oscillations: Celebrating the Nobel Prize in Physics 2015

[141] F. Cavanna, M. Kordosky, J. Raaf and B. Rebel, *LArIAT: Liquid Argon In A Testbeam* (2014)

[142] H. Du, Y. Yang and S. Cherry, *Comparison of four depth-encoding PET detector modules with wavelength shifting (WLS) and optical fiber read-out*, Physics in Medicine and Biology **53** (2008) (7), pp. 1829–1842, URL: https://www.scopus.com/inward/record.uri?eid=2-s2.0-42449159363&doi=10.1088%2f0031-9155%2f53%2f7%2f002&partnerID=40&md5=8d83187da8390adff40d59009490edd4, cited By 15

[143] E. Lorincz, G. Erdei, I. Peczeli, C. Steinbach, F. Ujhelyi and T. Bukki, *Modeling and Optimization of Scintillator Arrays for PET Detectors*, IEEE Transactions on Nuclear Science **57** (2010) (1), pp. 48–54

[144] General Formulations Concept 106, http://www.generalformulations.com/Products/Digital-Media/Mounting-Adhesives-(1)/Concept-106

[145] Autotiv Mfg, https://autotiv.com

[146] Ingeniven LLC, https://ingeniven.com

[147] Dylos DC1100, http://www.dylosproducts.com/dcairqumowip.html

[148] Drytac JetMounter Cold Roll Laminator, https://www.drytac.com/product/jm18-jm26-jm34-electric-jetmounter-table-top-laminators/

[149] *ASTM F88 / F88M-15 Standard Test Method for Seal Strength of Flexible Barrier Materials*

[150] Hatchbox 3D, https://hatchbox3d.com

[151] P. Analysis, *Data analysis framework for PROSPECT detectors.*, PROSPECT Github.

[152] R. Brun and F. Rademakers, *ROOT—an object oriented data analysis framework*, Nuclear Instruments and Methods in Physics Research Section A: Accelerators, Spectrometers, Detectors and Associated Equipment **389** (1997) (1-2), pp. 81–86

[153] S. Agostinelli *et al.*, *GEANT4—a simulation toolkit*, Nuclear instruments and methods in physics research section A: Accelerators, Spectrometers, Detectors and Associated Equipment **506** (2003) (3), pp. 250–303

[154] PROSPECT-G4, *Geant4 particle tracking simulation for PROSPECT experiment.*, PROSPECT Github.

[155] J. B. Birks, *Scintillations from Organic Crystals: Specific Fluorescence and Relative Response to Different Radiations*, Proceedings of the Physical Society. Section A **64** (1951) (10), p. 874,
URL: http://stacks.iop.org/0370-1298/64/i=10/a=303

[156] C. Patrignani, P. D. Group *et al.*, *Passage of particles through matter*, Chin. Phys. C **40** (2016), p. 100001

[157] M. Mendenhall, *Deadtime Technote*, PROSPECT DocDB-2350v2, July 2018

[158] A. Conant, *HFIR Core Modeling and Analysis for the PROSPECT Reactor Antineutrino Experiment.*, PROSPECT DocDB-1213v1, June 2016

[159] O. Kyzylova, *Cylindrical uniform power model vs real power distribution Comparison.*, PROSPECT DocDB-2290v1, May 2018.

[160] A. Conant, *HFIR Fission Distribution and Baseline Evolution.*, PROSPECT DocDB-2297v1, May 2018.

[161] H. Band, *Detector baseline estimate, DocDB-2229* (2018), PROSPECT DocDB-1213v1, June 2016

[162] P. T. Surukuchi, *Detector reactor baselines and angles, DocDB-2248* (2018), PROSPECT DocDB-1213v1, June 2016

[163] H. Band, *AD Geometry.*, PROSPECT DocDB-1006, Mar 2017

[164] P. Huber, *On the determination of anti-neutrino spectra from nuclear reactors*, Phys. Rev. **C84** (2011), p. 024617, [Erratum: Phys. Rev.C85,029901(2012)]

[165] P. T. Surukuchi, *Detector reactor baselines and angles, DocDB-2338* (2018), PROSPECT DocDB-2338v2, May 2018

[166] P. T. Surukuchi, *Al-28 and He-6 Contribution, DocDB-2709* (2018), PROSPECT DocDB-2709v2, March 2019

[167] C. J. Werner, J. S. Bull, C. J. Solomon, F. B. Brown, G. W. McKinney, M. E. Rising, D. A. Dixon, R. L. Martz, H. G. Hughes, L. J. Cox *et al.*, *MCNP Version 6.2 Release Notes*, Tech. rep., Los Alamos National Lab.(LANL), Los Alamos, NM (United States) (2018)

[168] P. T. Surukuchi, *Non-fission Contribution to Neutrinos, DocDB-2346* (2018), PROSPECT DocDB-2346v2, May 2018

[169] M. Mendenhall, *Improved quenching model for PROSPECT-G4.*, PROSPECT DocDB-1006v2, Mar 2016

[170] X. Zhang, *Energy Scale Update and Quoting Key Parameters.*, PROSPECT DocDB-2363v2, May 2018

[171] P. T. Surukuchi *et al.*, *Freezing Segment List*, PROSPECT DocDB-1213v1, June 2016

[172] D. Berish, *AD PMT and Cell ID Diagram*, PROSPECT DocDB-2004v1, Nov 2017

[173] D. Norcini, *Na22 peak shifts.*, PROSPECT DocDB-002349v2, May 2018

[174] D. Jones, *BiPo Analysis and Plots.*, PROSPECT DocDB-2377v2, June 2018

[175] D. Berish, *RnPo Coincidences in AD*, PROSPECT DocDB-2424v1, July 2018

[176] O. Kyzylova, *Cosmogenic Background vs Pressure and Time Tech Note.*, PROSPECT DocDB-2298v1, May 2018.

[177] J. Gaison, *Segment-to-Segment Relative Energy Uncertainty.*, PROSPECT DocDB-2296v1, June 2018

[178] L. Lyons, R. P. Mount and R. Reitmeyer (eds.), *Statistical problems in particle physics, astrophysics and cosmology. Proceedings, Conference, PHYSTAT 2003, Stanford, USA, September 8-11, 2003* (2003),
URL: `http://www-public.slac.stanford.edu/sciDoc/docMeta.aspx?slacPubNumber=slac-r-703`

[179] G. J. Feldman and R. D. Cousins, *Unified approach to the classical statistical analysis of small signals*, Phys. Rev. D **57** (1998), pp. 3873–3889,
URL: `https://link.aps.org/doi/10.1103/PhysRevD.57.3873`

[180] X. Qian, A. Tan, J. Ling, Y. Nakajima and C. Zhang, *The Gaussian CL s method for searches of new physics*, Nuclear Instruments and Methods in Physics Research Section A: Accelerators, Spectrometers, Detectors and Associated Equipment **827** (2016), pp. 63–78

[181] Y. Ko *et al.*, *Sterile neutrino search at the NEOS experiment*, Physical review letters **118** (2017) (12), p. 121802

[182] I. Alekseev *et al.*, *Search for sterile neutrinos at the DANSS experiment*, Physics Letters B **787** (2018), pp. 56 – 63,
URL: `http://www.sciencedirect.com/science/article/pii/S0370269318308098`

[183] Y. Declais *et al.*, *Search for neutrino oscillations at 15-meters, 40-meters, and 95-meters from a nuclear power reactor at Bugey*, Nucl. Phys. **B434** (1995), pp. 503–534

[184] L. Bernard, *New Results from STEREO: A Search for a Sterile Neutrino 1eV at Short Baselines* (2019),
URL: `http://moriond.in2p3.fr/2019/EW/Program.html`, rencontres de Moriond

[185] J. Ashenfelter *et al.*, *Measurement of the Antineutrino Spectrum from ^{235}U Fission at HFIR with PROSPECT* (2018)

[186] R. Carr *et al.*, *Neutrino-based tools for nuclear verification and diplomacy in North Korea*, arXiv preprint arXiv:1811.04737 (2018)

[187] R. Carr *et al.*, *Neutrino physics for Korean diplomacy.*, Science (New York, NY) **362** (2018) (6415), p. 649

[188] J. Neyman, *On the two different aspects of the representative method: the method of stratified sampling and the method of purposive selection*, Journal of the Royal Statistical Society **97** (1934) (4), pp. 558–625

[189] J. Neyman, E. S. Pearson, S. Kotz and N. L. Johnson, *On the Problem of the Most Efficient Tests of Statistical Hypotheses* (Springer New York, New York, NY, 1992), pp. 73–108,
URL: `https://doi.org/10.1007/978-1-4612-0919-5_6`

[190] L. Demortier, *Equivalence of the best-fit and covariance matrix methods for comparing binned data with a model in the presence of correlated systematic uncertainties*, Tech. rep., CDF Note 8661 (1999)

[191] USER17762, *Generating correlated random numbers: Why does Cholesky decomposition work?*, Mathematics Stack Exchange,
URL: `https://math.stackexchange.com/q/163472`

[192] K. Gilje, *Covariance Matrices.*, PROSPECT DocDB-1345v1, Sep 2016.

[193] S. S. Wilks, *The large-sample distribution of the likelihood ratio for testing composite hypotheses*, The Annals of Mathematical Statistics **9** (1938) (1), pp. 60–62

[194] A. Wald, *Tests of statistical hypotheses concerning several parameters when the number of observations is large*, Transactions of the American Mathematical society **54** (1943) (3), pp. 426–482